Astronomy & Astrophysics

High-*J* CO survey of low-mass protostars observed with *Herschel*-HIFI[*,**]

U. A. Yıldız[1], L. E. Kristensen[1,2], E. F. van Dishoeck[1,3], I. San José-García[1], A. Karska[3], D. Harsono[1], M. Tafalla[4], A. Fuente[5], R. Visser[6], J. K. Jørgensen[7,8], and M. R. Hogerheijde[1]

[1] Leiden Observatory, Leiden University, PO Box 9513, 2300 RA Leiden, The Netherlands
    e-mail: yildiz@strw.leidenuniv.nl
[2] Harvard-Smithsonian Center for Astrophysics, 60 Garden Street, Cambridge, MA 02138, USA
[3] Max Planck Institut für Extraterrestrische Physik, Giessenbachstrasse 1, 85748 Garching, Germany
[4] Observatorio Astronómico Nacional (IGN), Calle Alfonso XII, 3, 28014 Madrid, Spain
[5] Observatorio Astronómico Nacional, Apartado 112, 28803 Alcalá de Henares, Spain
[6] Department of Astronomy, University of Michigan, 500 Church Street, Ann Arbor, MI 48109-1042, USA
[7] Niels Bohr Institute, University of Copenhagen, Juliane Maries Vej 30, 2100 Copenhagen Ø., Denmark
[8] Centre for Star and Planet Formation, Natural History Museum of Denmark, University of Copenhagen, Øster Voldgade 5–7, 1350 Copenhagen K., Denmark

ABSTRACT

Context. In the deeply embedded stage of star formation, protostars start to heat and disperse their surrounding cloud cores. The evolution of these sources has traditionally been traced through dust continuum spectral energy distributions (SEDs), but the use of CO excitation as an evolutionary probe has not yet been explored due to the lack of high-*J* CO observations.
Aims. The aim is to constrain the physical characteristics (excitation, kinematics, column density) of the warm gas in low-mass protostellar envelopes using spectrally resolved *Herschel* data of CO and compare those with the colder gas traced by lower excitation lines.
Methods. *Herschel*-HIFI observations of high-*J* lines of ^{12}CO, ^{13}CO, and C^{18}O (up to $J_{\rm u} = 10$, $E_{\rm u}$ up to 300 K) are presented toward 26 deeply embedded low-mass Class 0 and Class I young stellar objects, obtained as part of the Water In Star-forming regions with *Herschel* (WISH) key program. This is the first large spectrally resolved high-*J* CO survey conducted for these types of sources. Complementary lower *J* CO maps were observed using ground-based telescopes, such as the JCMT and APEX and convolved to matching beam sizes.
Results. The ^{12}CO 10–9 line is detected for all objects and can generally be decomposed into a narrow and a broad component owing to the quiescent envelope and entrained outflow material, respectively. The ^{12}CO excitation temperature increases with velocity from ~60 K up to ~130 K. The median excitation temperatures for ^{12}CO, ^{13}CO, and C^{18}O derived from single-temperature fits to the $J_{\rm u} = 2$–10 integrated intensities are ~70 K, 48 K and 37 K, respectively, with no significant difference between Class 0 and Class I sources and no trend with $M_{\rm env}$ or $L_{\rm bol}$. Thus, in contrast to the continuum SEDs, the spectral line energy distributions (SLEDs) do not show any evolution during the embedded stage. In contrast, the integrated line intensities of all CO isotopologs show a clear decrease with evolutionary stage as the envelope is dispersed. Models of the collapse and evolution of protostellar envelopes reproduce the C^{18}O results well, but underproduce the ^{13}CO and ^{12}CO excitation temperatures, due to lack of UV heating and outflow components in those models. The H$_2$O $1_{10} - 1_{01}$/CO 10–9 intensity ratio does not change significantly with velocity, in contrast to the H$_2$O/CO 3–2 ratio, indicating that CO 10–9 is the lowest transition for which the line wings probe the same warm shocked gas as H$_2$O. Modeling of the full suite of C^{18}O lines indicates an abundance profile for Class 0 sources that is consistent with a freeze-out zone below 25 K and evaporation at higher temperatures, but with some fraction of the CO transformed into other species in the cold phase. In contrast, the observations for two Class I sources in Ophiuchus are consistent with a constant high CO abundance profile.
Conclusions. The velocity resolved line profiles trace the evolution from the Class 0 to the Class I phase through decreasing line intensities, less prominent outflow wings, and increasing average CO abundances. However, the CO excitation temperature stays nearly constant. The multiple components found here indicate that the analysis of spectrally unresolved data, such as provided by SPIRE and PACS, must be done with caution.

Key words. astrochemistry – stars: formation – stars: protostars – ISM: molecules – techniques: spectroscopic

1. Introduction

Low-mass stars like our Sun form deep inside collapsing molecular clouds by accreting material onto a central dense source. As the source evolves, gas and dust move from the envelope to the disk and onto the star, resulting in a decrease in the envelope mass and a shift in the peak of the continuum spectral energy distribution to shorter wavelengths (e.g., Lada 1999; André et al. 2000; Young & Evans 2005). At the same time, jets and winds from the protostar entrain material and disperse the envelope. Spectral lines at submillimeter wavelengths trace this dense molecular gas and reveal both the kinematic signature of collapse (Gregersen et al. 1997; Myers et al. 2000; Kristensen et al. 2012) as well as the high velocity gas in the outflows (Arce et al. 2007).

The most commonly used probe is CO because it is the second most abundant molecule after H_2, has a simple energy level structure, and all main isotopolog lines are readily detectable (^{12}CO, ^{13}CO, $C^{18}O$, $C^{17}O$). Because of its small dipole moment, its rotational lines are easily excited and therefore provide an excellent estimate of the gas column density and the kinetic temperature. Although low excitation lines of CO have been observed in protostars for decades (e.g., Hayashi et al. 1994; Blake et al. 1995; Bontemps et al. 1996; Jørgensen et al. 2002; Fuller & Ladd 2002; Tachihara et al. 2002; Hatchell et al. 2005), no systematic studies have been undertaken so far of the higher excitation lines that probe the warm gas ($T > 100$ K) during protostellar evolution. Ground-based observations of other molecules exist as well and in some (but not all) show low-mass sources a variety of complex organic species commonly ascribed to "hot cores" where ices evaporate molecules back into the gas phase (e.g., van Dishoeck & Blake 1998; Ceccarelli et al. 2007). Quantifying these hot core abundances has been complicated by the lack of a good reference of the H_2 column density in this warm ≥100 K gas.

With the launch of the *Herschel* Space Observatory (Pilbratt et al. 2010) equipped with new efficient detectors, observations of low-mass protostars in higher-J transitions of CO have become possible. In this paper, high-J refers to the lines $J_u \geq 6$ ($E_u > 100$ K) and low-J refers to $J_u \leq 5$ ($E_u < 100$ K). The Heterodyne Instrument for Far-Infrared (HIFI; de Graauw et al. 2010) on *Herschel* offers a unique opportunity to observe spectrally resolved high-J CO lines of various isotopologs with unprecedented sensitivity (see Yıldız et al. 2010; Plume et al. 2012, for early results). Even higher transitions of CO up to $J_u = 50$ are now routinely observed with the Photoconducting Array and Spectrometer (PACS; Poglitsch et al. 2010) and the Spectral and Photometric Imaging Receiver (SPIRE; Griffin et al. 2010) instruments on *Herschel*, but those data are spectrally unresolved, detect mostly ^{12}CO, and probe primarily a hot shocked gas component associated with the source (e.g., van Kempen et al. 2010; Herczeg et al. 2012; Goicoechea et al. 2012; Karska et al. 2013; Manoj et al. 2013; Green et al. 2013). To study the bulk of the protostellar system and disentangle the various physical components, velocity resolved lines of isotopologs including optically thin $C^{18}O$ are needed.

In this paper, we use *Herschel*-HIFI single pointing observations of high-J CO and its isotopologs up to the 10–9 ($E_u/k = 300$ K) transition from low-mass protostars obtained in the "Water in Star-forming regions with *Herschel*" (WISH) key program (van Dishoeck et al. 2011). The CO lines have been obtained as complement to the large set of lines from H_2O, OH and other related molecules in a sample of ~80 low to high-mass protostars at different evolutionary stages. This study focuses on low-mass protostellar sources ($L_{bol} < 100$ $L_\odot$) ranging from the most deeply embedded Class 0 phase to the more evolved Class I stage. The *Herschel* CO data are complemented by ground-based lower-J transitions.

The warm gas probed by these high-J CO lines is much more diagnostic of the energetic processes that shape deeply embedded sources than the low-J lines observed so far. Continuum data from submillimeter to infrared wavelengths show that the temperature characterizing the peak wavelength of the SED (the so-called bolometric temperature T_{bol}; Myers & Ladd 1993) increases from about 25 K for the earliest Class 0 sources to about 200–300 K for the more evolved Class I sources, illustrating the increased dust temperatures as the source evolves. At the same time, the envelope gradually decreases with evolution from ~1 $M_\odot$ to <0.05 $M_\odot$ (Shirley et al. 2000; Young & Evans 2005).

Our CO data probe gas over the entire range of temperature and masses found in these protostellar envelopes. Hence we pose the following questions regarding the evolution of the envelope and interaction with both the outflow and immediate environment: (*i*) Does the CO line intensity decrease with evolutionary stage from Class 0 to Class I in parallel with the dust? (*ii*) Does the CO excitation change with evolutionary stage, as does the dust temperature? (*iii*) How do the CO molecular line profiles (i.e., kinematics) evolve through 2–1 up to 10–9? For example, what fraction of emission is contained in the envelope and outflow components? (*iv*) What is the relative importance of the different energetic processes in the YSO environment, e.g., passive heating of the envelope, outflows, photon heating, and how is this quantitatively reflected in the lines of the three CO isotopologs? (*v*) Can our data directly probe the elusive "hot core" and provide a column density of quiescent warm ($T > 100$ K) gas as reference for chemical studies? How do those column densities evolve from Class 0 to Class I?

To address these questions, the full suite of lines and isotopologs is needed. The ^{12}CO line wings probe primarily the entrained outflow gas. The ^{13}CO lines trace the quiescent envelope but show excess emission that has been interpreted as caused by UV-heated gas along outflow cavity walls (Spaans et al. 1995; van Kempen et al. 2009b). The $C^{18}O$ lines probe the bulk of the collapsing envelope heated by the protostellar luminosity and can be used to constrain the CO abundance structure. These different diagnostic properties of the CO and isotopolog lines have been demonstrated through early *Herschel*-HIFI results of high-J CO and isotopologs up to 10–9 by Yıldız et al. (2010, 2012) for three low-mass protostars and by Fuente et al. (2012) for one intermediate protostar. Here we investigate whether the conclusions on column densities, temperatures of the warm gas and CO abundance structure derived for just a few sources hold more commonly in a large number of sources covering different physical characteristics and evolutionary stages.

This paper presents *Herschel*-HIFI CO and isotopolog spectra for a sample of 26 low-mass protostars. The *Herschel* data are complemented by ground-based spectra to cover as many lines as possible from $J = 2$–1 up to $J = 10$–9, providing the most complete survey of velocity resolved CO line profiles of these sources to date. We demonstrate that the combination of low- and high-J lines for the various CO isotopologs is needed to get the complete picture. The *Herschel* data presented here are also included in the complementary paper by San José-García et al. (2013) comparing high-J CO from low- to high-mass YSOs. That paper investigates trends across the entire mass spectrum, whereas this paper focuses on a detailed analysis of the possible excitation mechanisms required to explain the CO emission.

The outline of the paper is as follows. In Sect. 2, the observations and the telescopes used to obtain the data are described. In Sect. 3, the *Herschel* and complementary lines are presented and a decomposition of the line profiles is made. In Sect. 4, the data for each of the CO isotopologs are analyzed, probing the different physical components. Rotational excitation diagrams are constructed, column densities and abundances are determined and kinetic temperatures in the entrained outflow gas are constrained. The evolution of these properties from the Class 0 to the Class I sources is studied and compared with evolutionary models. Section 7 summarizes the conclusions from this work.

2. Observations and complementary data

An overview of observed spectral lines with their upper level energies, Einstein A coefficients, and rest frequencies are presented

Table 1. Overview of the observed transitions.

Molecule	Trans. J_u–J_l	E_u [K]	A_{ul} [s^{-1}]	Freq. [GHz]
CO	2–1	16.6	6.910×10^{-7}	230.538000
	3–2	33.19	2.497×10^{-6}	345.795989
	4–3	55.3	6.126×10^{-6}	461.040768
	6–5	116.2	2.137×10^{-5}	691.473076
	7–6	154.9	3.422×10^{-5}	806.651806
	10–9	304.2	1.006×10^{-4}	1151.985452
^{13}CO	2–1	15.9	6.038×10^{-7}	220.398684
	3–2	31.7	2.181×10^{-6}	330.587965
	4–3	52.9	5.353×10^{-6}	440.765174
	6–5	111.1	1.868×10^{-5}	661.067277
	8–7	190.4	4.487×10^{-5}	881.272808
	10–9	290.8	8.797×10^{-5}	1101.349597
C^{18}O	2–1	15.8	6.011×10^{-7}	219.560354
	3–2	31.6	2.172×10^{-6}	329.330553
	5–4	79.0	1.062×10^{-5}	548.831010
	6–5	110.6	1.860×10^{-5}	658.553278
	9–8	237.0	6.380×10^{-5}	987.560382
	10–9	289.7	8.762×10^{-5}	1097.162875

Notes. The level energies, Einstein A coefficients, and line frequencies are from the LAMDA, JPL and CDMS databases (Schöier et al. 2005; Pickett et al. 2010; Müller et al. 2005).

in Table 1. The selection of the sources and their characteristics are described in van Dishoeck et al. (2011) and Kristensen et al. (2012) together with the targeted coordinates. In total, 26 low-mass young stellar objects were observed in CO of which 15 are Class 0 and 11 Class I sources, with the boundary taken to be at T_{bol} = 70 K (Myers & Ladd 1993; Chen et al. 1995). In terms of envelope mass, the boundary between the two classes is roughly at 0.5 $M_\odot$ (Jørgensen et al. 2002). All Class I sources have been vetted to be truly embedded "Stage I" sources cf. Robitaille et al. (2006) and not Class II edge-on disks or reddened background stars (van Kempen et al. 2009c,d). Throughout the paper, Class 0 sources are marked as red, and Class I sources are marked as blue in the figures. In addition to *Herschel*-HIFI spectra, data come from the 12-m sub-mm Atacama Pathfinder Experiment Telescope, APEX[1] at Llano de Chajnantor in Chile, and the 15-m *James Clerk Maxwell* Telescope (JCMT)[2] at Mauna Kea, Hawaii. The overview of all the observations can be found in Table B.1.

All data were acquired on the T_A^* antenna temperature scale, and were converted to main-beam brightness temperatures $T_{MB} = T_A^*/\eta_{MB}$ (Kutner & Ulich 1981) by using the beam efficiencies (η_{MB}) stated in each of the source Tables C.1–C.26.

Herschel: spectral line observations of ^{12}CO 10–9, ^{13}CO 10–9, C^{18}O 5–4, 9–8 and 10–9 were obtained with HIFI as part of the WISH guaranteed time key program on *Herschel*. Single pointing observations at the source positions were carried out between March 2010 and October 2011. An overview of the HIFI observations for each source is provided in Table D.1 with their corresponding *Herschel* Science Archive

(HSA) obsids. The lines were observed in dual-beam switch (DBS) mode using a switch of 3′. The CO transitions were observed in combination with the water lines: ^{12}CO 10–9 with H$_2$O 3_{12}–2_{21} (10 min); ^{13}CO 10–9 with H$_2$O 1_{11}–0_{00} (40 min); C^{18}O 5–4 with H$_2^{18}$O 1_{10}–1_{01} (60 min); C^{18}O 9–8 with H$_2$O 2_{02}–1_{11} (20 min); and C^{18}O 10–9 with H$_2$O 3_{12}–3_{03} (30 min or 5 h). Only a subset of the H$_2$O lines were observed toward all Class I sources and therefore C^{18}O 5–4 and part of the isotopolog CO 10–9 data are missing for these sources. For C^{18}O 9–8, IRAS 2A, IRAS 4A, IRAS 4B, Elias 29, and GSS30 IRS1 were observed in very deep integrations for 5 h in the open-time program OT2_rvisser_2 (PI: R. Visser). Also, the C^{18}O 5–4 lines have very high signal-to-noise ratio (S/N) because of the long integration on the H$_2^{18}$O line. Thus, the noise level varies per source and per line.

The *Herschel* data were taken using the wide-band spectrometer (WBS) and high-resolution spectrometer (HRS) backends. Owing to the higher noise ranging from a factor of 1.7 up to 4.7 of the HRS compared with the WBS, mainly WBS data are presented here except for the narrow C^{18}O 5–4 lines where only the HRS data are used. The HIFI beam sizes are ∼20″ (∼4000 AU for a source at ∼200 pc) at 1152 GHz and 42″ (∼8400 AU) at 549 GHz. The typical spectral resolution ranges from 0.68 km s^{-1} (band 1) to 0.3 km s^{-1} (band 5) in WBS, and 0.11 km s^{-1} (band 1) in HRS. Typical rms values range from 0.1 K for ^{12}CO 10–9 line to 9 mK for C^{18}O 10–9 in the longest integration times.

Data processing started from the standard HIFI pipeline in the *Herschel* interactive processing environment (HIPE[3]) ver. 8.2.1 (Ott 2010), where the V_{lsr} precision is of the order of a few m s^{-1}. Further reduction and analysis were performed using the GILDAS-CLASS[4] software. The spectra from the H- and V-polarizations were averaged to obtain better *S/N*. In some cases a discrepancy of 30% or more was found between the two polarizations, in which case only the H band spectra were used for analysis. These sources are indicated in Tables C.1–C.26. Significant emission contamination from one of the reference position was found at the ^{12}CO 10–9 observation of IRAS 2A and IRAS 4A. In that case, only one reference position, which was clean, was used in order to reduce the data. On the other hand, even though the pointing accuracy is ∼2″, the H- and V-polarizations have slightly shifted pointing directions (Band 1: −6.″2, +2.″2; Band 4: −1.″3, −3.″3; Band 5: 0.″0, +2.″8), which may give rise to different line profiles in strong extended sources (Roelfsema et al. 2012). No corrections were made for these offsets. The HIFI beam efficiencies are 0.76, 0.74, and 0.64 for bands 1, 4, and 5, respectively (Roelfsema et al. 2012).

APEX: maps of the ^{12}CO 6–5, 7–6 and ^{13}CO 6–5 lines over a few arcmin region were observed with the CHAMP$^+$ instrument (Kasemann et al. 2006; Güsten et al. 2008) at the APEX telescope for all sources visible from Chajnantor, whereas ^{13}CO 8–7 and C^{18}O 6–5 lines were obtained for selected objects in staring mode. The CHAMP$^+$ instrument consists of two heterodyne receiver arrays, each with seven pixel detector elements for simultaneous operations in the 620–720 GHz and 780–950 GHz frequency ranges. The APEX beam sizes correspond to 8″ (∼1600 AU for a source at 200 pc) at 809 GHz and 9″ (∼1800 AU) at 691 GHz. A detailed description of the instrument and observations of several sources in the current

sample have been presented in van Kempen et al. (2009a,b,c); Yıldız et al. (2012) and the remaining maps will be given in Yıldız et al. (in prep.). Here only the data for the central source positions are considered. In addition, lower-J transitions were observed for southern sources using various receivers at APEX (van Kempen et al. 2006, 2009a,b,c).

JCMT: all sources visible from the JCMT were mapped by the HARP (Buckle et al. 2009) instrument over an area of $2' \times 2'$ in ^{12}CO, ^{13}CO and C^{18}O 3–2 transitions. HARP consists of 16 SIS detectors with 4×4 pixel elements of 15″ each at 30″ separation. Other 2–1 lines were observed with the single pixel RxA instrument at a beam size of ∼23″ by Jørgensen et al. (2002). Part of those observations were fetched from the JCMT public archive[5].

Since the observations involve a number of different telescopes and frequencies, the beam sizes differ for each case. The maps obtained with the JCMT and APEX were resampled to a common resolution of 20″ so as to be directly comparable to the beam size of the HIFI CO 10–9 and 9–8 observations (20″ and 23″, respectively) as well as the JCMT CO 2–1 observations (22″). The exception are a few CO 4–3 lines that are only available for a single pointing in an 11″ beam size which are indicated in the tables at the Appendix C. The 20″ beam corresponds to a diameter of 2500 AU for a source at 125 pc (closest distance), and 9000 AU for a source in 450 pc (furthest distance), so the observing beam encloses both the bulk of the dense envelope as well as outflow material. The data reduction and analysis for each source were finalized using the GILDAS-CLASS software. Calibration errors are estimated as ∼20% for the ground-based telescopes (Buckle et al. 2009, for JCMT), and ∼10% for the HIFI lines (Roelfsema et al. 2012).

The full APEX and JCMT maps will be presented in Yıldız et al. (in prep) where the outflows are studied in more detail. The full set of lines for NGC 1333 IRAS 2A, IRAS 4A and IRAS 4B have also been presented in Yıldız et al. (2010, 2012) (except for the deeper C^{18}O 10–9 data), but for completeness and comparison with the rest of the WISH sample, the data are included in this paper.

3. Results

3.1. CO line gallery

The ^{12}CO, ^{13}CO and C^{18}O spectra from $J = 2$–1 up to $J = 10$–9 for each source are provided in Appendix C. This appendix contains figures of all the observed spectra and tables with the extracted information. Summary spectra are presented in Fig. 1 for the CO 3–2, 10–9, ^{13}CO 10–9, C^{18}O 5–4, 9–8, and 10–9 lines, respectively. Emission is detected in almost all transitions with our observing setup except some higher-J isotopolog lines discussed below. The high-J CO lines observed with *Herschel* are the first observations for these types of sources. Decomposition of line profiles is discussed in detail in San José-García et al. (2013) and is only briefly summarized below.

3.2. ^{12}CO lines

^{12}CO 10–9 emission is detected in all sources. Integrated and peak intensities are typically higher in the Class 0 sources compared with the Class I sources. Typical integrated intensities at

Table 2. Relative fractions of integrated intensities calculated for broad and narrow components in ^{12}CO 10–9 lines.

Source	$\int T_{MB}dV$ (K km s^{-1})		%^{a}	
	NC	BC	NC	BC
L1448MM	12.7	33.9	27	73
NGC 1333-IRAS 2A	6.4	3.1	67	33
NGC 1333-IRAS 4A	...	49.4	...	100
NGC 1333-IRAS 4B	5.6	23.6	19	81
L1527	4.2	...	100	...
Ced110IRS4	1.8	3.7	33	67
BHR71	7.8	8.2	49	51
IRAS15398	9.9	6.8	59	41
L483MM	4.7	6.3	44	56
Ser SMM1	26.2	53.1	33	67
Ser SMM4	31.7	35.0	47	53
Ser SMM3	9.3	15.7	37	63
L723MM	3.5	3.4	51	49
B335	2.6	9.2	22	78
L1157	1.4	6.8	17	83
L1489	2.5	3.4	42	58
L1551IRS5	8.5	6.0	59	41
TMR1	1.3	7.6	15	85
HH46	3.1	5.4	37	63
DK Cha	8.2	1.8	82	18
GSS30IRS1	31.2	11.8	73	27
Elias29	10.6	36.5	22	78
TMC1A	(1.4^b)	...	...	...
TMC1	(2.9^b)	...	...	...
Oph IRS63	(1.1^b)	...	...	...
RNO91	(5.2^b)	...	...	...

Notes. NC: narrow component, BC: broad component; $^{(a)}$ Relative percentages of the integrated intensities given in the 2nd and 3rd columns. $^{(b)}$ Due to low S/N in their spectra, profiles could not be decomposed, however, total integrated intensities are given.

the source positions range from 1 K km s^{-1} (in Oph IRS63) up to 82 K km s^{-1} (in Ser-SMM1), whereas peak intensities range from 0.6 K (in Oph IRS63) up to 9.3 K (in GSS30 IRS1). One striking result is that none of the ^{12}CO 10–9 observations show self-absorption except for Ser-SMM1 and GSS30 IRS1, whereas all of the CO 3–2 observations have strong self-absorption, which suggests optically thick line centers[6]. The absorption components are located at the source velocities as indicated by the peak of the low-J C^{18}O emission and are thus due to self-absorption from the outer envelope. Examining other available ^{12}CO transitions (lower than $J = 10$–9) shows that the self-absorption diminishes with increasing J and disappears for all sources (again except Ser-SMM1 and GSS30 IRS1) at around $J = 10$–9 (see Figs. C.1–C.26).

For the ^{12}CO lines, more than two thirds of the sample can readily be decomposed into two Gaussian components with line widths of ≤7.5 km s^{-1} (narrow) and 11–25 km s^{-1} (broad; see Fig. 2; San José-García et al. 2013, for details). The narrow component is due to the quiescent envelope whereas the broad component represents the swept-up outflow gas[7]. Figure 3 summarizes the relative fraction of each of the components in terms of integrated intensities (also tabulated in Table 2). For four sources in the sample, i.e., TMC1A, TMC1, Oph IRS63, and RNO91, the

[6] The only exception is IRAS 15398 where the targeted position is off source, see Kristensen et al. (2012).

[7] The broad CO component is not necessarily the same physical component as seen in the broad H$_2$O profiles; this point will be further discussed in Sect. 5.3.
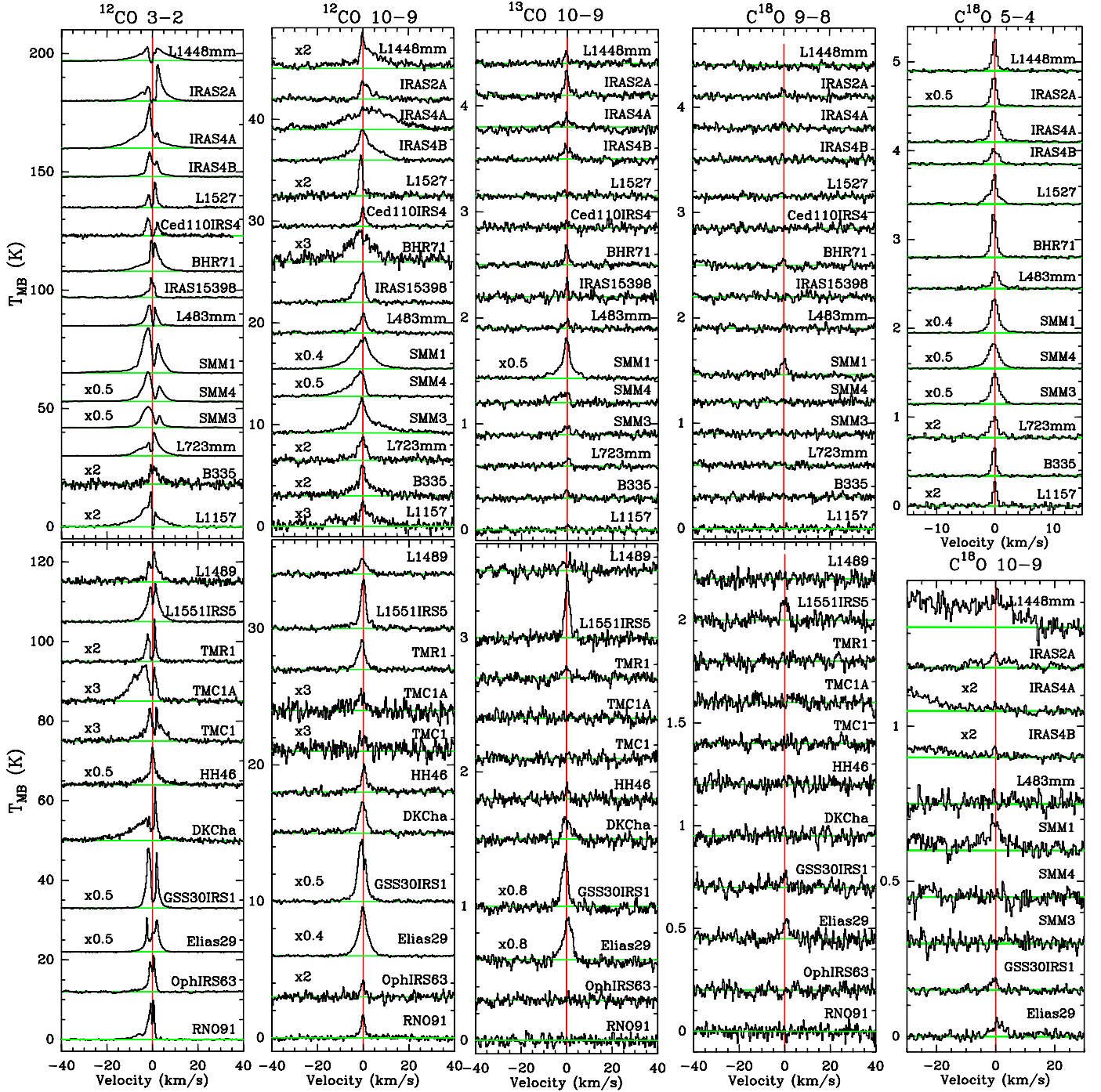
Fig. 1. On source CO spectra convolved to a ~20″ beam. From left to right: ^{12}CO 3–2, 10–9, ^{13}CO 10–9, C^{18}O 9–8, 5–4 and 10–9, respectively. Only the CO 3–2 lines are observed with the JCMT, the rest of the data are from *Herschel*-HIFI. The spectra are plotted by shifting the source velocity (V_{lsr}) to 0 km s^{-1} (actual source velocities are given in Table 4). The lines are shifted vertically. Intensity scale of some sources is multiplied by a constant value for easy viewing and marked if different from 1. The *top half of the figure* shows the Class 0 sources whereas the *bottom part* displays the Class I sources. The *right-most column* displays the C^{18}O 5–4 and C^{18}O 10–9 lines for the Class 0 sources only. The latter lines are very close to the H$_2$O 3$_{12}$–3$_{03}$ line resulting in an intensity rise on the blue side of the spectrum in some sources.

profiles could not be decomposed due to low *S/N* in their spectra. The fraction of emission contained in the narrow component ranges from close to 0% (IRAS 4A) to nearly 100% (L1527), with a median fraction of 42%. Particularly, for IRAS 4A, the narrow component is most likely hidden under the strong broad component, whereas for L1527, outflows are in the plane of the sky therefore the broad component is not evident. This decomposition demonstrates that the contributions from these two components are generally comparable so care must be taken

in interpreting spectrally unresolved data from *Herschel*-SPIRE and PACS, and, to some extent, near-IR transitions of the same molecules.

Figure 4 presents the averaged ^{12}CO 3–2, 10–9, and H$_2$O 1$_{10}$−1$_{01}$ lines for the Class 0 and Class I sources in order to obtain a generic spectral structure for one type of source. To compare with the H$_2$O spectra, a similar averaging procedure was followed as in Kristensen et al. (2012), where ground state ortho-water composite spectra observed with *Herschel*-HIFI
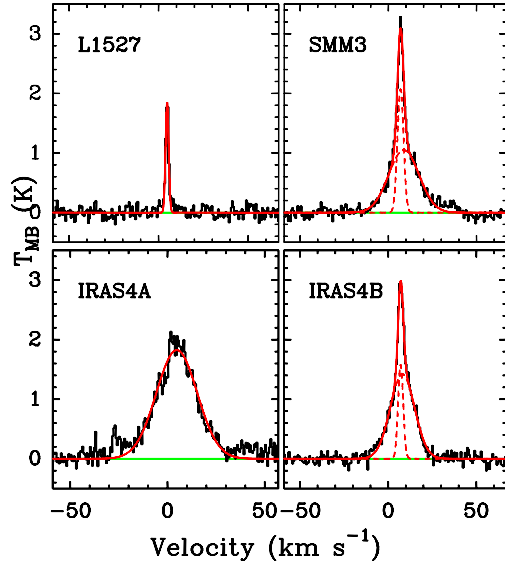
Fig. 2. Gaussian decomposition of the ^{12}CO 10–9 profile toward four sources. The profile toward two sources, L1527 and IRAS 4A, can be decomposed into a single Gaussian, whereas SMM3, IRAS 4B and all the remaining sources in the sample require two components (decomposition shown with the dashed red fit).
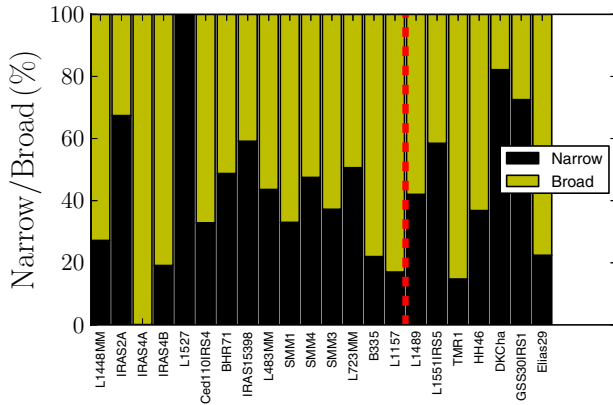

Fig. 3. Relative fraction of the integrated intensity of the narrow and broad components for each source. The ^{12}CO 10–9 profile decomposition is given in San José-García et al. (2013). Yellow regions indicate the broad component fraction and black the narrow component fractions. The red dashed line divides the Class 0 (*left*) and Class I (*right*) sources.

Fig. 4. Composite H$_2$O 1_{10}–1_{01}, CO 10–9 and CO 3–2 spectra of Class 0 and Class I sources averaged in order to compare the line profiles of two types of sources. All spectra are rescaled to a common distance of 200 pc, shifted to the central 0 km s^{-1} velocity, rebinned to a 0.3 km s^{-1} velocity resolution. The CO spectra refer to a 20$''$ beam, the H$_2$O spectra to a 40$''$ beam. The red spectra overlaid on top of the ^{12}CO 10–9 are obtained by normalizing all the spectra to a common peak temperature first and then averaging them.

at 557 GHz were presented in a beam of 40$''$. In this comparison, the IRAS 15398 (Class 0), TMC1 and GSS30 IRS1 (Class I) spectra have been excluded from the averaging procedure. The CO 10–9 line of IRAS 15398 is taken at a position 15$''$ offset from the source position, the TMC1 spectrum was too noisy and the excitation of GSS30 IRS1 may not be representative of Class I sources (Kristensen et al. 2012). Therefore, 14 Class 0 and 9 Class I spectra are scaled to a common distance of 200 pc and averaged.

It is seen that the broad CO outflow component is much more prominent in the Class 0 than in the Class I sources (Fig. 4). For the Class 0 sources, the 10–9 line is broader than the 3–2 lines. However, neither is as broad as the line wings seen in H$_2$O 557 GHz lines, for which the average H$_2$O spectra are taken from Kristensen et al. (2012). The comparison between CO and H$_2$O will be discussed further in Sect. 5.3.
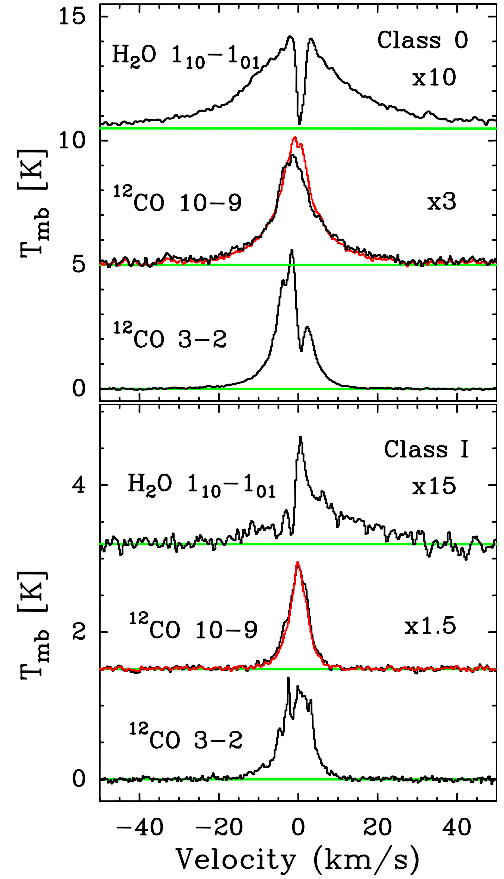
For a few sources, high velocity molecular emission features associated with shock material moving at velocities up to hundred km s^{-1} have been observed (Bachiller et al. 1990; Tafalla et al. 2010). For species like SiO, their abundance is increased due to shock-induced chemistry (Bachiller & Perez Gutierrez 1997; Bourke et al. 1997). These Extremely High Velocity (EHV) components (or "bullet" emission) are also visible in the higher-J CO transitions, as well as in lower-J transitions, but the contrast in emission between bullet and broad outflow emission is greatly enhanced at higher frequencies. Bullets are visible specifically in CO 6–5 and 10–9 data toward L1448 mm and BHR71 at ~±60 km s^{-1} (see Fig. 5 for the bullets and Table 3 for the fit parameters). These bullets are also seen in H$_2$O observations of the same sources, as well as other objects (Kristensen et al. 2011, 2012).

3.3. ^{13}CO lines

^{13}CO emission is detected in all sources except for the 10–9 transition toward Oph IRS63, RNO91, TMC1A, and TMR1. The 10–9 integrated and peak intensities are higher in Class 0 sources compared with the Class I sources. Typical integrated intensities range from 0.1 K (L1527) up to 3.4 K km s^{-1} (Ser-SMM1). Peak intensities range from 0.1 K (L1448 MM, L1527) up to

Table 3. Fit parameters obtained from the bullet sources.

| Source | EHV-B | | | Broad | | | Narrow | | | EHV-R | | |
	$\int T_{\rm MB}{\rm d}V$ [K km s^{-1}]	$T_{\rm peak}$ [K]	*FWHM* [km s^{-1}]	$\int T_{\rm MB}{\rm d}V$ [K km s^{-1}]	$T_{\rm peak}$ [K]	*FWHM* [km s^{-1}]	$\int T_{\rm MB}{\rm d}V$ [K km s^{-1}]	$T_{\rm peak}$ [K]	*FWHM* [km s^{-1}]	$\int T_{\rm MB}{\rm d}V$ [K km s^{-1}]	$T_{\rm peak}$ [K]	*FWHM* [km s^{-1}]
L1448MM	6.9	0.26	24.6	17.5	0.30	54.3	6.5	1.10	7.5	8.1	0.43	17.8
BHR71	4.2	0.16	25.2	10.8	0.18	55.6	4.2	0.71	10.0	3.9	0.14	27.1

Table 4. Source parameters.

Source	d [pc]	$v_{\rm LSR}{}^a$ [km s^{-1}]	$L_{\rm bol}{}^b$ [$L_\odot$]	$T_{\rm bol}{}^b$ [K]	$M_{\rm env\,(10\,K)}{}^c$ [$M_\odot$]	$n_{1000\,{\rm AU}}{}^{c,d}$ [10^5 cm^{-3}]	$n_{20''}{}^{c,e}$ [10^5 cm^{-3}]
L1448-MM	235	+5.2	9.0	46	3.9	39	11
NGC 1333-IRAS 2A	235	+7.7	35.7	50	5.1	17	4.0
NGC 1333-IRAS 4A	235	+7.0	9.1	33	5.6	67	15
NGC 1333-IRAS 4B	235	+7.1	4.4	28	3.0	57	17
L1527	140	+5.9	1.9	44	0.9	8.1	6.0
Ced110-IRS4	125	+4.2	0.8	56	0.2	3.9	2.8
BHR71	200	−4.4	14.8	44	2.7	18	5.4
IRAS 15398	130	+5.1	1.6	52	0.5	16	11
L483 mm	200	+5.2	10.2	49	4.4	5.1	2.8
Ser-SMM1	230	+8.5	30.4	39	16.1	41	14
Ser-SMM4	230	+8.0	1.9	26	2.1	54	23
Ser-SMM3	230	+7.6	5.1	38	3.2	11	5.5
L723	300	+11.2	3.6	39	1.3	8.0	2.2
B335	250	+8.4	3.3	36	1.2	15	4.3
L1157	325	+2.6	4.7	46	1.5	20	2.9
L1489	140	+7.2	3.8	200	0.2	1.9	1.2
L1551-IRS5	140	+6.2	22.1	94	2.3	12	6.4
TMR1	140	+6.3	3.8	133	0.2	2.1	1.2
TMC1A	140	+6.6	2.7	118	0.2	2.2	1.3
TMC1	140	+5.2	0.9	101	0.2	1.8	1.2
HH46-IRS	450	+5.2	27.9	104	4.4	12	1.1
DK Cha	178	+3.1	35.4	569	0.8	9.2	3.7
GSS30-IRS1	125	+3.5	13.9	142	0.6	1.7	1.1
Elias 29	125	+4.3	14.1	299	0.3	0.8	0.6
Oph-IRS63	125	+2.8	1.0	327	0.3	6.9	5.0
RNO91	125	+0.5	2.6	340	0.5	3.3	2.4

Notes. Sources above the horizontal line are Class 0, sources below are Class I. [a] Obtained from ground-based C^{18}O or C^{17}O observations. [b] Measured using *Herschel*-PACS data from the WISH and DIGIT key programmes (Karska et al. 2013; Green et al. 2013). [c] Determined from DUSTY modeling of the sources; see Kristensen et al. (2012). [d] Density at 1000 AU. [e] Density at a region of 20″ diameter.

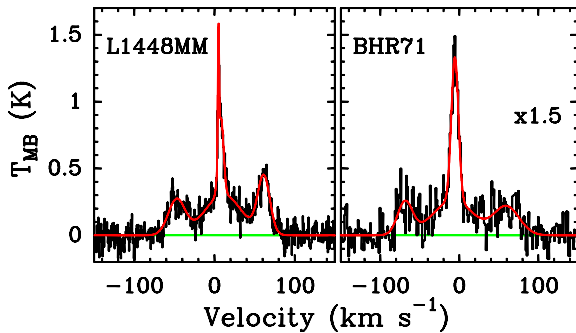**Fig. 5.** ^{12}CO 10–9 spectra of L1448 mm and BHR71, where bullet structures are shown. The green lines indicates the baseline and the red lines represent the Gaussian fits of the line profiles. Fit parameters are given in Table 3.

0.4 K (Ser-SMM1). All ^{13}CO 10–9 lines can be fitted by a single Gaussian (narrow component) except for Ser-SMM1 and IRAS 4A where two Gaussians (narrow and broader component) are needed.

3.4. C^{18}O lines

C^{18}O emission is detected in all sources up to J = 5–4. The 9–8 line is seen in several sources, mostly Class 0 objects (BHR71, IRAS 2A, IRAS 4A, IRAS 4B, Ser-SMM1, L1551 IRS5). The C^{18}O 10–9 line is detected after 5-hour integrations in IRAS 2A, IRAS 4A, IRAS 4B, Elias 29, GSS30 IRS1, and Ser-SMM1, with integrated intensities ranging from 0.05 (in IRAS 4A) up to 0.6 K km s^{-1} (Ser-SMM1). Peak intensities range from 0.02 K up to 0.07 K for the same sources. The rest of the high-J C^{18}O lines do not show a detection but have stringent upper limits. The high S/N and high spectral resolution C^{18}O 5–4 data reveal a weak, broad underlying component even in this minor isotopolog for several sources (see Fig. 1 in Yıldız et al. 2010).

The availability of transitions from 2–1 to 10–9 for many sources in optically thin C^{18}O lines also gives an opportunity to revisit source velocities, $V_{\rm lsr}$ that were previously obtained from the literature. Table 4 presents the results with nine sources showing a change in $V_{\rm lsr}$, compared with values listed in

Table 5. Extracted rotational temperatures and column densities.

Source	Rotational temperature [K]			H$_2$ column density^a [10^{21} cm^{-2}]		Kinetic temperature^b [K]		X_{constant}^{c}
	^{12}CO	^{13}CO	C^{18}O	from ^{13}CO	from C^{18}O	Blue wing	Red wing	$\times 10^{-8}$
L1448-MM	81 ± 10	46 ± 7	39 ± 6	5.0 ± 0.7	4.4 ± 0.6	60–75	100–200	2.1
NGC 1333-IRAS 2A	57 ± 7	46 ± 6	39 ± 6	6.8 ± 0.9	9.2 ± 1.3	. . .	. . .	6.0
NGC 1333-IRAS 4A	77 ± 9	43 ± 5	39 ± 5	10.6 ± 1.3	6.5 ± 0.8	70–80	80–110	1.4
NGC 1333-IRAS 4B	83 ± 11	48 ± 7	34 ± 5	2.4 ± 0.4	9.0 ± 1.4	110–170	110–280	1.5
L1527	62 ± 8	38 ± 5	31 ± 5	6.0 ± 0.8	5.5 ± 0.8	80–130	80–110	14.0
Ced110-IRS4	66 ± 9	42 ± 16	<33	3.0 ± 1.1	<7.8	. . .	. . .	17.0
BHR71	72 ± 13	62 ± 21	36 ± 7	1.7 ± 0.6	5.0 ± 1.0	75–105	70–140	8.5
IRAS15398	104 ± 16	60 ± 12	35 ± 5	0.9 ± 0.2	3.8 ± 0.7	. . .	. . .	3.5
L483	77 ± 10	43 ± 6	39 ± 6	4.5 ± 0.6	4.0 ± 0.6	105–300	100–240	6.0
Ser SMM1	97 ± 12	60 ± 8	50 ± 5	12.7 ± 1.7	10.1± 1.1	90–120	100–230	2.2
Ser SMM4	71 ± 10	43 ± 7	36 ± 7	9.2 ± 1.6	8.8 ± 1.6	75–120	50–120	6.0
Ser SMM3	74 ± 9	37 ± 5	32 ± 4	19.8 ± 2.8	12.7± 1.8	75–175	80–260	10.0
L723	71 ± 13	43 ± 5	34 ± 5	4.6 ± 0.6	2.8 ± 0.4	. . .	. . .	4.4
B335	71 ± 9	46 ± 6	34 ± 5	3.0 ± 1.7	3.6 ± 0.5	. . .	. . .	9.0
L1157	62 ± 8	50 ± 8	35 ± 6	3.4 ± 0.5	2.1 ± 0.3	75–130	85–120	2.4
L1489	75 ± 9	49 ± 10	<37	3.5 ± 0.7	<3.7	. . .	. . .	17.0
L1551-IRS5	68 ± 10	53 ± 8	39 ± 6	10.7 ± 1.5	11.3 ± 1.8	70–130	70–130	8.0
TMR1	94 ± 12	56 ± 11	<35	3.1 ± 0.6	< 4.9	. . .	. . .	38.0
TMC1A	49 ± 6	52 ± 11	<37	1.4 ± 0.3	<3.4	. . .	. . .	17.0
TMC1	68 ± 9	53 ± 11	<33	1.1 ± 0.2	<6.0	. . .	. . .	50.0
HH46-IRS	61 ± 7	41 ± 7	<33	7.1 ± 1.1	<8.0	100–130	105–300	9.0
DK Cha	68 ± 10	62 ± 10	<38	3.2 ± 0.5	<3.6	. . .	. . .	7.0
GSS30-IRS1	77 ± 11	45 ± 6	35 ± 5	37.0 ± 5.1	24.0 ± 3.7	160–300	130–240	45.0
Elias 29	103 ± 14	49 ± 7	39 ± 6	19.1 ± 2.7	31.1 ± 4.4	340–400	340–400	50.0
Oph-IRS63	50 ± 7	42 ± 8	<40	4.6 ± 0.9	<2.4	. . .	. . .	40.0
RNO91	65 ± 9	35 ± 5	<39	5.2 ± 0.8	<2.9	. . .	. . .	12.0

Notes. Rotational temperatures and column densities calculated from ^{12}CO, ^{13}CO and C^{18}O observations. Kinetic temperatures calculated from blue and red line wings. $^{(a)}$ In H$_2$ column densities. Derived using a constant abundance ratio of CO/H$_2$ = 10^{-4}. $^{(b)}$ Obtained from CO 10–9/3–2 line intensity ratios as explained in Sect. 4.5. $^{(c)}$ Constant abundance fits as explained in Sect. 6.1.

van Dishoeck et al. (2011) ranging from 0.2 km s^{-1} (IRAS 4A) up to 1.0 km s^{-1} (L1551-IRS5).

4. Rotational diagrams

To understand the origin of the CO emission, rotational diagrams provide a useful starting point to constrain the temperature of the gas. In our sample, we have CO and isotopolog emission lines of all sources from J = 2–1 up to 10–9 with upper level energies from E_{up} = 5 K to ~300 K. Rotational diagrams are constructed assuming that the lines can be characterized by a single excitation temperature T_{ex}, also called rotational temperature T_{rot}. Typically, the isotopolog ^{13}CO and C^{18}O lines are optically thin, as well as the ^{12}CO line wings (see van Kempen et al. 2009b; Yıldız et al. 2012), so no curvature should be induced in their excitation diagrams due to optical depth effects. However, the low-J ^{12}CO line profiles have strong self-absorption and their cores are optically thick, leading to the column density of these levels being underestimated. The C^{18}O 5–4 line has a beam size of 42″ and may thus contain unrelated cloud material, so its uncertainty is artificially enhanced from 10% to 20% in order to reduce its weight in the fit calculations.

Using the level energies, Einstein A coefficients and line frequencies from Table 1 and the cited databases, rotational diagrams are constructed where the column density for each level is plotted against its level energy (Goldsmith & Langer 1999). This temperature T_{rot} is basically defined from the Boltzmann equation

$$\frac{N_{\text{u}}}{N_{\text{l}}} = \frac{g_{\text{u}}}{g_{\text{l}}} e^{(-\Delta E/kT_{\text{rot}})}, \tag{1}$$

where N_{u} and N_{l} are the column densities in the upper and lower states, and g_{u} and g_{l} their statistical weights equal to $2J_{\text{u}}$ + 1 and $2J_{\text{l}}$ + 1, respectively. The CO column densities in individual levels are obtained from

$$\frac{N_{\text{u}}}{g_{\text{u}}} = \beta \frac{(\nu[\text{GHz}])^2 \, W[\text{K km s}^{-1}]}{A_{\text{ul}}[\text{s}^{-1}] \, g_{\text{u}}}, \tag{2}$$

where β = 1937 cm^{-2} and $W = \int T_{\text{mb}} dV$ is the integrated intensity of the emission line.

The slope of the linear fit to the observations, $-(1/T_{\text{rot}})$, gives the rotational temperature, whereas the y-intercept gives the total column density ln $(N_{\text{total}}/Q(T_{\text{rot}}))$ where $Q(T_{\text{rot}})$ is the partition function referenced from CDMS for the temperature given by the fit.

The total integrated intensity W for each line is measured over the entire velocity range out to where line wings become equal to the 1σ noise. In L1448 mm and BHR71, the bullet emission is not included in the intensity calculation. In IRAS 2A, the emission in the 10–9 line is corrected for emission at one of the reference positions, which results in a higher T_{rot} compared with Yıldız et al. (2012).

4.1. Rotational diagram results

In Figs. 6–8, rotational diagrams are depicted for the ^{12}CO, ^{13}CO and C^{18}O lines, respectively. Extracted excitation temperatures and column densities are presented in Table 5; ^{12}CO column densities are not provided because they are affected by optical depth effects. In all sources the data can be fitted to a single temperature component from J = 2–1 up to 10–9 with a
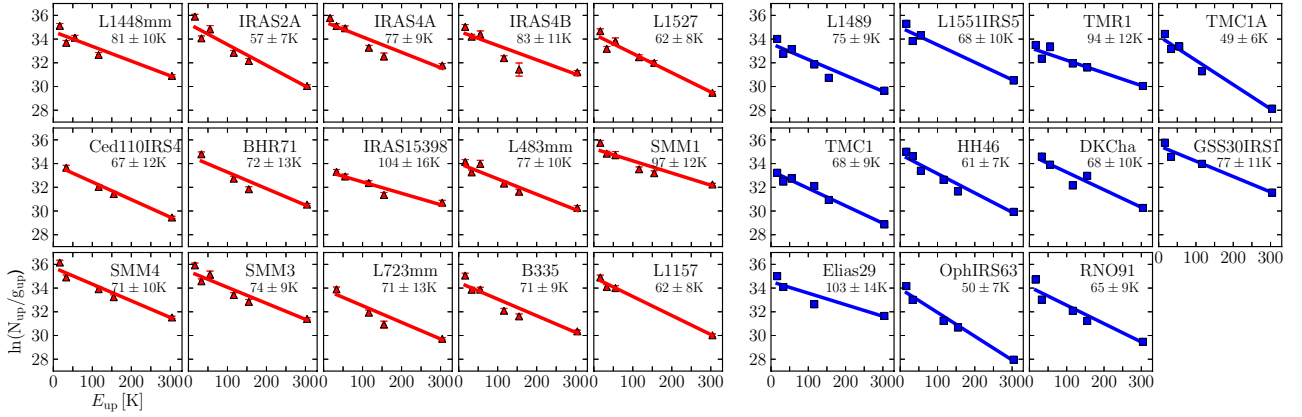
Fig. 6. Rotational diagrams for ^{12}CO lines using the integrated intensities. All data are convolved to a 20″ beam and each plot shows the best single temperature fit to the observed transitions (see also Table 5). *Left panel* (red): Class 0 sources; *right panel* (blue): Class I sources.
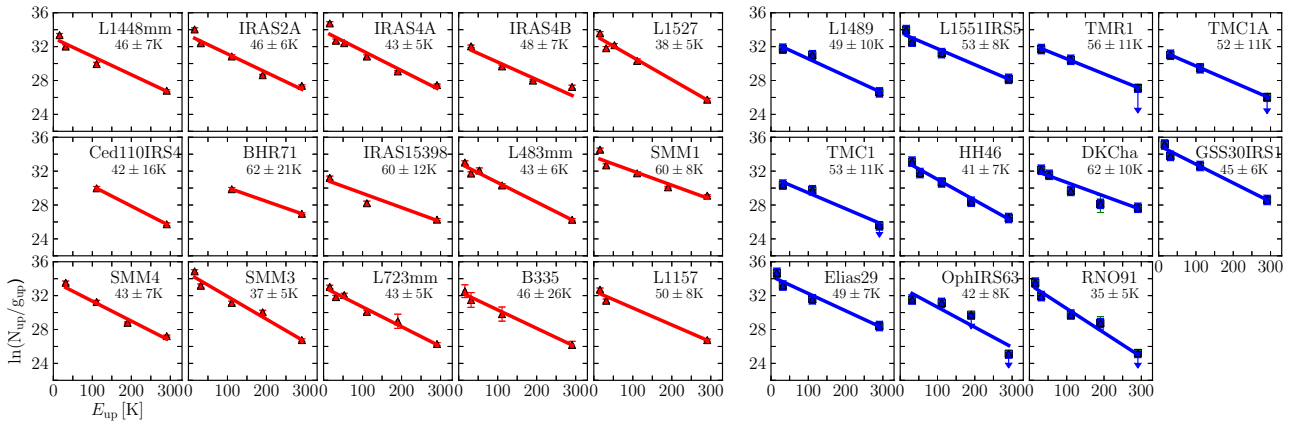

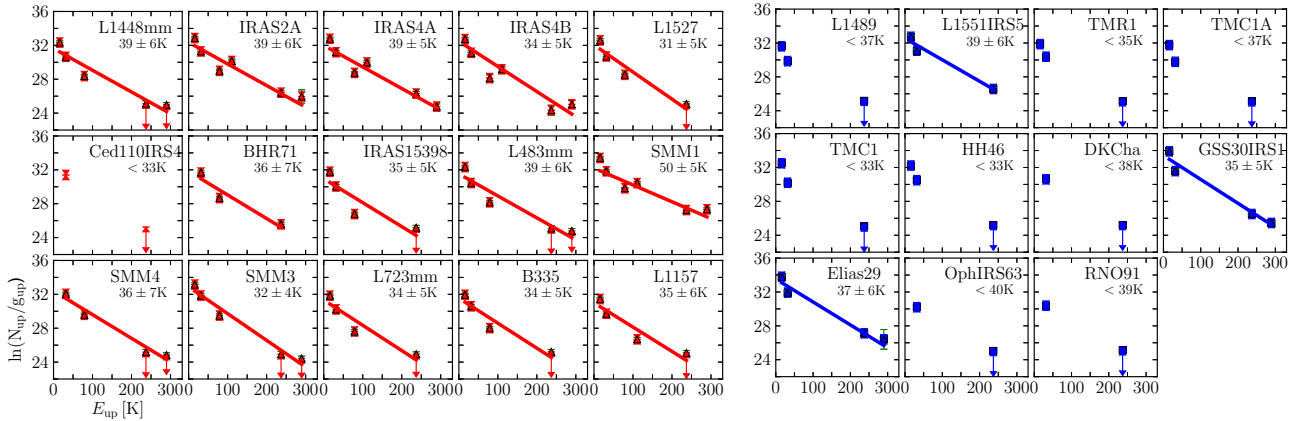**Fig. 7.** Same as Fig. 6 but for ^{13}CO lines.

Fig. 8. Same as Fig. 6 but for C^{18}O lines.

range of uncertainty from 12% to 21% except ^{13}CO temperatures in Ced110-IRS4 and BHR71 where only two observations are present. Curvature is present for a number of sources which will be discussed in Sect. 4.3. The derived ^{12}CO rotational temperatures range from ∼50 K to ∼100 K. The median temperatures for both Class 0 and Class I sources are similar, $T_{rot} = 71$ K and 68 K, respectively.

For ^{13}CO, the temperatures range from T_{rot} ∼35 K to ∼60 K, with a median $T_{rot} = 46$ K and 49 K for Class 0 and Class I sources, respectively. For C^{18}O, the median temperature for Class 0 sources is $T_{rot} = 36$ K. For Class I sources, either

lack of observational data or non-detections make it harder to obtain an accurate temperature. Nevertheless, upper limits are still given. The median T_{rot} for the sources with ≥3 data points is 37 K. A summary of the median rotational temperatures is given in Table 6. Figure 9 presents the ^{12}CO and ^{13}CO temperatures in histogram mode for the Class 0 and Class I sources, with no statistically significant differences between them. Note that this analysis assumes that all lines have a similar filling factor in the ∼20″ beam; if the higher-J lines would have a smaller filling factor than the lower-J lines the inferred rotational temperatures would be lower limits.

Table 6. Median rotational temperatures and colum densities of Class 0 and Class I sources calculated from ^{12}CO, ^{13}CO and $C^{18}O$.

| | Rotational temperature [K] | | | Column density^a [10^{21} cm^{-2}] | |
	^{12}CO	^{13}CO	$C^{18}O$	^{13}CO	$C^{18}O$
Class 0	71 ± 13	46 ± 6	36 ± 7	4.6 ± 0.6	5.2 ± 0.9
Class I	68 ± 9	49 ± 10	…	4.6 ± 0.9	…

Notes. Median's error is taken as global error value. $^{(a)}$ Derived using a constant abundance ratio of $CO/H_2 = 10^{-4}$.
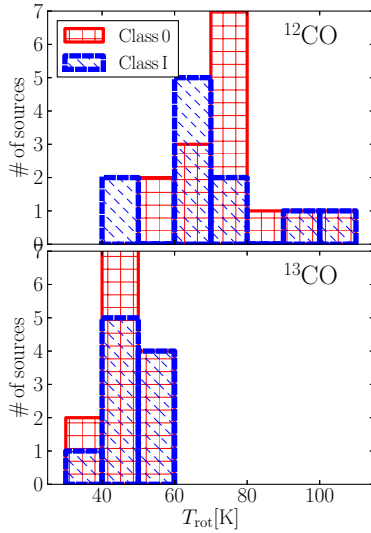
Fig. 9. Distribution of rotation temperatures (T_{rot}) calculated from ^{12}CO and ^{13}CO line observations. The median temperatures are listed in Table 6.

For the case of Serpens-SMM1, our inferred rotational temperatures of 97 ± 12 and 60 ± 8 K compare well with those of 103 ± 15 and 76 ± 6 K found by Goicoechea et al. (2012) from *Herschel*-SPIRE data for ^{12}CO and ^{13}CO, respectively. The SPIRE values were obtained from a fit to the $J_u = 4–14$ levels, with the beam changing by a factor of ~3 from ~47″ to ~13″ across the ladder.

The ^{12}CO and ^{13}CO 2–1 lines included in Figs. 6 and 7 are observed in a similar ~20″ beam as the higher transitions, but they most likely include cold cloud emission as well. Removing those lines from the rotational diagrams increases the temperatures around 10–15 %. Similarly, the $C^{18}O$ 5–4 line is observed in a 42″ beam and removing this line from the fit increases the temperatures around 5–10%, which is still within the error bars. In practice, we did not discard the $C^{18}O$ 5–4 observations but increased their uncertainty to give them less weight in the calculations. The effect of multiple velocity components in discussed in Sect. 4.4.

The ^{13}CO and $C^{18}O$ column densities are converted to ^{12}CO column densities by using $^{12}C/^{13}C = 65$ (based on Langer & Penzias 1990; Vladilo et al. 1993) and $^{16}O/^{18}O = 550$ (Wilson & Rood 1994) and then using $CO/H_2 = 10^{-4}$ to obtain the H_2 column density (tabulated in Table 5). The median H_2 column densities for Class 0 sources are 4.6×10^{21} cm^{-2} and 5.2×10^{21} cm^{-2} for ^{13}CO and $C^{18}O$ data, respectively. For Class I sources the value is 4.6×10^{21} cm^{-2} for ^{13}CO, with the caveat that only few Class I sources have been measured in $C^{18}O$. The agreement between the two isotopologs indicates that the lines are not strongly affected by optical depths. Since this conversion uses a CO/H_2 abundance ratio close to the maximum, the inferred

H_2 column densities should be regarded as minimum values. In particular, for Class 0 sources freeze-out and other chemical processes will lower the CO/H_2 abundance (see Sect. 6) (Jørgensen et al. 2002). Thus, the actual difference in column densities between the Class 0 and Class I stages is larger than is shown in Table 5.

4.2. CO ladders

Spectral Line Energy Distribution (SLED) plots are another way of representing the CO ladder where the integrated flux is plotted against upper level rotational quantum number, J_{up}. In Fig. 10, ^{12}CO line fluxes for the observed transitions are plotted. Since the CO 3–2 lines are available for all sources, the fluxes are all normalized to their own CO 3–2 flux. The thick blue and red lines are the median values of all sources for each transition for each class. It is readily seen that the Class 0 and Class I sources in our sample have similar excitation conditions, but that the Class I sources show a wider spread at high-J and have higher error bars due to the weaker absolute intensities. Similarly, as can be inferred from Fig. 9, the ^{13}CO SLEDs do not show any significant difference between the two classes. Thus, although the continuum SEDs show a significant evolution from Class 0 to Class I with T_{bol} increasing from <30 K to more than 500 K, this change is not reflected in the line SLEDs of the ^{12}CO or the optically thinner ^{13}CO excitation. This limits the usage of CO SLEDs as an evolutionary probe. One of the explanations for this lack of evolution is that T_{bol} depends on thermal emission from both the dust in the envelope and the extincted stellar flux, whereas the SLED only traces the temperature of the gas in the envelope and/or outflow, but has no stellar component. Moreover, the infrared dust emission comes from warm (few hundred K) optically thick dust very close to the protostar, whereas, the CO originates further out the envelope.

4.3. Two temperature components?

Unresolved line observations of higher-J CO transitions ($J = 13$ up to 50) by *Herschel*-PACS (Herczeg et al. 2012; Karska et al. 2013; Manoj et al. 2013) typically show two temperature components with ~300 K and ~900 K. Goicoechea et al. (2012) found three temperature components from combined SPIRE and PACS data, with the lower temperature of ~100 K fitting lines up to $J_u = 14$, similar to that found in our data. The question addressed here is if the higher 300 K component only appears for lines with $J_u > 10$ or whether it becomes visible in our data. One third of our sample shows a positive curvature in the ^{12}CO rotation diagrams (Fig. 6), specifically IRAS 4A, IRAS 4B, BHR71, IRAS 15398, L483mm, Ser-SMM1, L723mm, B335, and L1489 (see Fig. 11).

The curvature in ^{12}CO rotation diagrams is treated by dividing the ladder into two components, where the first fit is from 2–1 to 7–6 for the colder component and the second fit from 7–6 to 10–9 for the warmer component. The fit from 2–1 to 10–9 is named as global. The median T_{rot} is 43 K for the colder component and 138 K for the warmer component for these nine sources.

Close inspection of the SPIRE data by Goicoechea et al. (2012) shows a slight curvature for low-J in their cold component as well. The "two-component" decomposition is perhaps a generic feature for Class 0 low-mass protostars, which implies that the CO 10–9 transition is at the border of the transitions for the cold ($T_{rot} < 100$ K) and warm ($T_{rot} \sim 300$ K) component associated with the currently shocked gas (Karska et al. 2013). T_{rot} clearly increases when higher rotational levels are
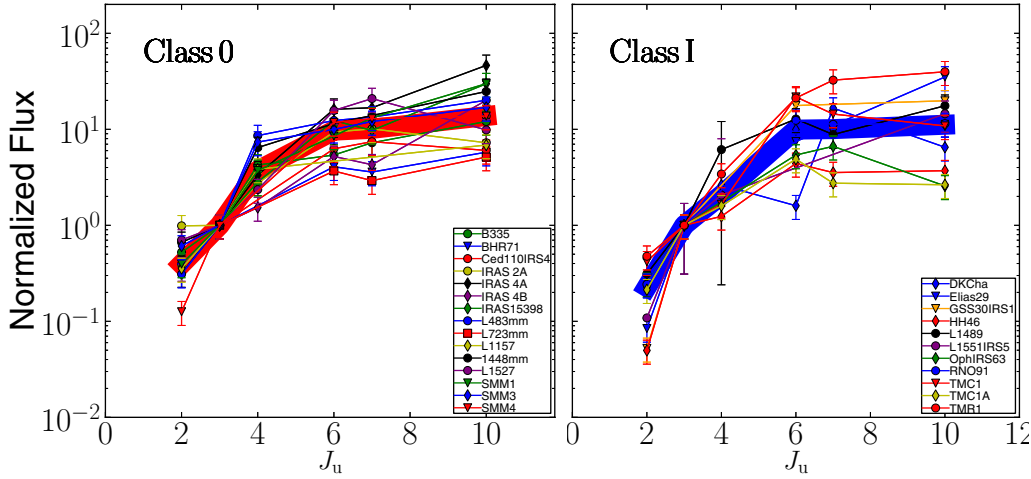
Fig. 10. ^{12}CO spectral line energy distribution (SLED) for the observed transitions. All of the fluxes are normalized to their own CO 3–2 flux for Class 0 (*left*) and Class I (*right*) sources separately. The beams are ~20″ beam. The thick lines are the median values of each transitions.
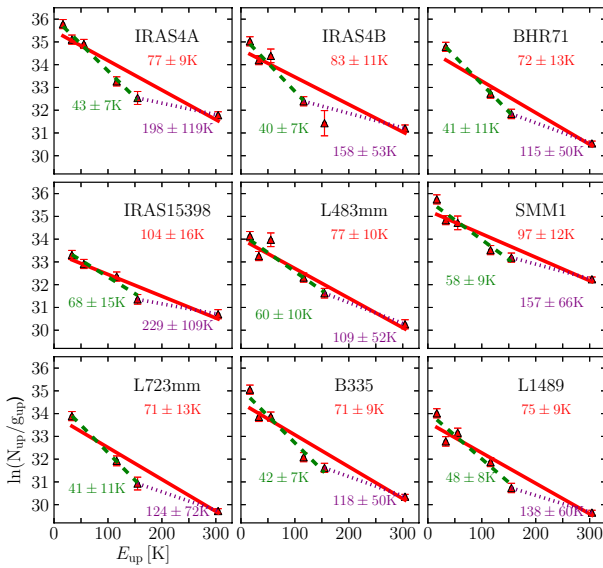

Fig. 11. Two temperature components fitted for selected sources to the ^{12}CO lines, from 2–1 to 7–6 (cold), from 7–6 to 10–9 (warm), and 2–1 to 10–9 (global).

Fig. 12. Rotational temperatures calculated channel by channel for ^{12}CO. Each spectrum is shifted to $V_{\mathrm{lsr}} = 0$ km s^{-1} and rebinned to 3 km s^{-1} velocity resolution.

added (Fig. 11), and for the brightest sources in NGC 1333 and Serpens, $T_{\mathrm{rot}} > 150$ K. See Sect. 4.4 for further discussion.

4.4. Velocity resolved diagrams

To investigate whether the ^{12}CO narrow and broad components have different temperatures, Fig. 12 presents excitation temperatures calculated channel by channel for a few sources with high *S/N*. Each spectrum is shifted to $V_{\mathrm{lsr}} = 0$ km s^{-1} and rebinned to 3 km s^{-1} velocity resolution. It is obvious from Fig. 1 that the line wings are more prominent in the CO 10–9 transitions, specifically for Class 0 sources, as is reflected also in the increasing line widths with the increasing rotation level (see Figs. C.1–C.26; San José-García et al. 2013). Figure 12 shows that in the optically thin line wings, the excitation temperatures are a factor of 2 higher than in the line centers implying that the wings of the higher-J CO lines are associated with the warmer material described in Sect. 4.3. Since the presence of self-absorption at line centers of the lower-J lines reduces their emission, the excitation temperatures at low velocities are further decreased if this absorption is properly corrected for.
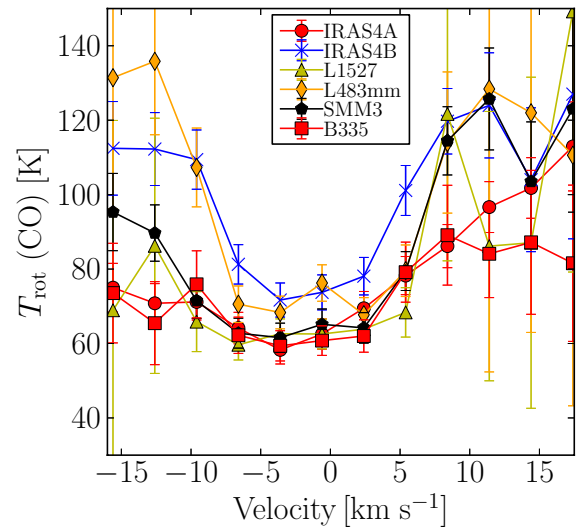
Another way to illustrate the change with velocity is to look at the CO 10–9 and CO 3–2 spectra for each source as shown in Fig. A.1. Figure 13 shows the blue and red line-wing ratios for the 14 sources with the highest *S/N*. For all sources, the line ratios increase with increasing velocity, consistent with Fig. 12.

In summary, while a single rotational temperature provides a decent fit to the bulk of the CO and isotopolog data, both the ^{12}CO integrated intensity rotational diagrams and the velocity resolved diagrams indicate the presence of a second, highly excited component for Class 0 sources. This warmer and/or denser component is most likely associated with the broad line wings, as illustrated by the 10–9/3–2 line ratios, whereas the colder component traces the narrow quiescent envelope gas. On average, the integrated intensities have roughly equal contributions from the narrow and broad components (Fig. 3) so the single rotational temperatures are a weighted mean of the cold and warmer values.

4.5. Kinetic temperature

Having lines from low-to-high-J CO provides information about the physical conditions in the different parts of the envelope.
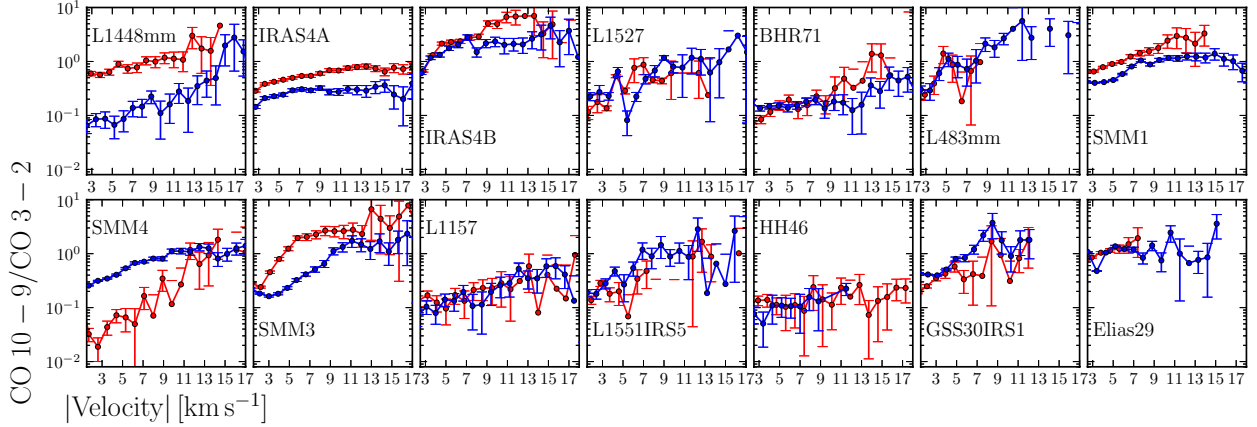
Fig. 13. Ratios of the CO 10–9/3–2 line wings for 14 protostars as function of velocity offset from the central emission. Spectra are shifted to $V_{lsr} = 0$ km s^{-1}. The wings start at ± 2.5 km s^{-1} from V_{lsr} in order to prevent adding the central self-absorption feature in the CO 3–2 lines.

The critical densities for the different transitions are $n_{cr} = 4.2 \times 10^5$ cm^{-3}, 1.2×10^5 cm^{-3}, and 2×10^4 cm^{-3} for CO 10–9, 6–5 and 3–2 transitions at ~ 50–100 K, using the CO collisional rate coefficients by Yang et al. (2010). For densities higher than n_{cr}, the emission is thermalized and therefore a clean temperature diagnostic, however, for lower densities the precise value of the density plays a role in the analysis. In the high density case ($n > n_{cr}$), the kinetic temperature is equal to the rotation temperature. By using two different ^{12}CO lines, kinetic temperatures can be calculated if the density is known independently using the RADEX non-LTE excitation and radiative transfer program (van der Tak et al. 2007). The analysis below for CO 10–9/3–2 assumes that the emission originates from the same gas.

The resulting model line ratios are presented in Fig. 14 for a grid of temperatures and densities. Densities for each source are calculated from the envelope parameters determined by modeling of the submillimeter continuum emission and spectral energy distribution (Kristensen et al. 2012). A spherically symmetric envelope model with a power-law density structure is assumed (Jørgensen et al. 2002). The 20″ diameter beam covers a range of radii from ~ 1250 AU (e.g., Ced110IRS4, Oph sources) up to 4500 AU (HH46) and the densities range from 5.8×10^4 cm^{-3} (Elias 29) up to 2.3×10^6 cm^{-3} (Ser-SMM4). The densities for all sources at the 10″ radius are given at the last column in Table 4. Note that these are lower limits since the densities increase inward of 10″. The envelope densities are used here as a proxy for the densities at the outflow walls where the entrainment occurs.

The majority of the Class 0 sources have densities that are similar or higher than the critical densities of the high-J CO lines, with the possible exceptions of Ced110-IRS4, L483 mm, L723 mm, and L1157. However, in Class I sources, the majority of the densities are lower than the critical densities with the exception of L1551 IRS5. The inferred kinetic temperatures from the CO 10–9/3–2 blue and red line-wings, which generally increase with velocity, are presented in Table 5 and range mostly from 70 K to 250 K. The ratios for individual sources are included in Fig. 14 at the 10″ radius density of the sources.

The thick magenta and black bars indicate the average values for the composite Class 0 and Class I sources (Sect. 5.3). For average densities at a 10″ radius of $\sim 10^6$ cm^{-3} and $\sim 10^5$ cm^{-3} for Class 0 and Class I sources, respectively, the CO 10–9/CO 3–2 line ratios would imply kinetic temperatures of around 80–130 K for Class 0 and 140–180 K for Class I sources (Fig. 14), assuming the two lines probe the same physical component. If part of
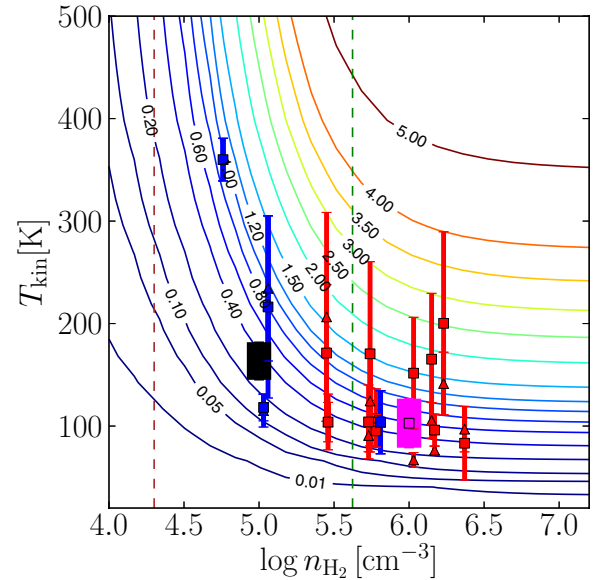
Fig. 14. Model CO 10–9/3–2 line intensity ratios as function of temperature and density, obtained for a CO column density of 10^{16} cm^{-2} with line-widths of 10 km s^{-1}, representative of the observed CO intensity and line width. Note that the bars are the ranges of lower and upper limits as seen from the observations in Fig. 13. Red markers are for Class 0 and blue markers are for Class I sources. Blue wing ratios are indicated with triangles and red wing ratios have square symbols. Thick magenta and black lines indicate the ratios from the composite spectra for Class 0 and Class I sources, respectively. Vertical dashed lines indicate the limits for n_{cr} for CO 3–2 (brown) and CO 10–9 (green). In the relevant density range, higher ratios are indicative of higher kinetic temperatures.

the CO 10–9 emission comes from a different physical component, these values should be regarded as upper limits.

5. Correlations with physical properties

5.1. Integrated intensities

Figure 15 shows the integrated intensities W of the CO 10−9 lines plotted against L_{bol}, M_{env}, and T_{bol}. The intensities are scaled to a common distance of 200 pc. The bolometric luminosity, L_{bol} and bolometric temperature T_{bol} of the sources have been measured using data from infrared to millimeter wavelengths including new *Herschel* far-infrared
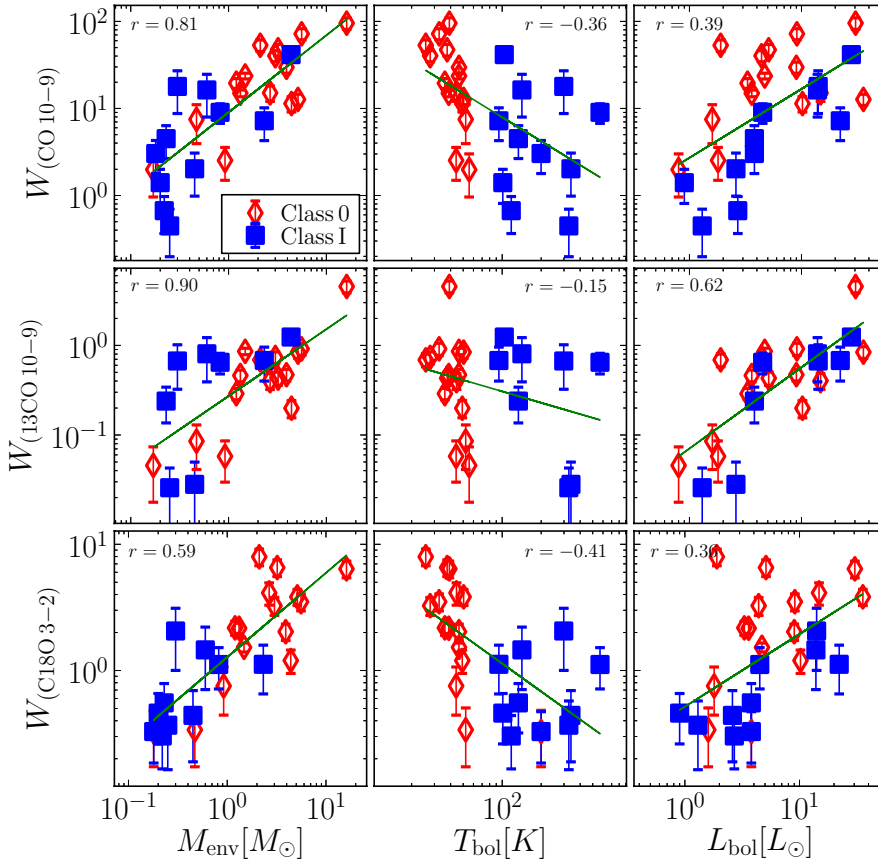
Fig. 15. From top to bottom, ^{12}CO 10–9, ^{13}CO 10–9, and C^{18}O 3–2 integrated intensity W normalized at 200 pc are plotted against various physical properties: envelope mass at 10 K radius, M_{env}; bolometric temperature, T_{bol}; and bolometric luminosity, L_{bol}. Green lines are the best fit to the data points and r values in each of the plots are Pearson correlation coefficient.

fluxes, and are presented in Kristensen et al. (2012). These are commonly used evolutionary tracers in order to distinguish young stellar objects. The envelope mass, M_{env} is calculated from the DUSTY modeling by Kristensen et al. (2012).

In Fig. 15, the green lines are the best power-law fits to the entire data set. Clearly, the CO 10–9 lines are stronger for the Class 0 sources which have higher M_{env} and L_{bol} and lower T_{bol}, for all isotopologs. The same correlation is seen for other (lower-J) CO and isotopolog lines, such as CO 2–1, 3–2, 4–3, 6–5 and 7–6; examples for ^{13}CO 10–9 and C^{18}O 3–2 are included in Fig. 15. The Pearson correlation coefficients for ^{12}CO 10–9 are $r = 0.39$ (1.87σ), 0.81 (4.05σ), and −0.36 (−1.68σ) for L_{bol}, M_{env}, and T_{bol}, respectively. The coefficients, r, for M_{env} in ^{13}CO 10–9 and C^{18}O 3–2 are 0.90 (4.49σ) and 0.59 (2.97σ). Those correlations indicate that there is a strong correlation between the intensities and envelope mass, M_{env}, consistent with the lines becoming weaker as the envelope is dissipated. Together with the high-J CO lines, the C^{18}O low-J lines are also good evolutionary tracers in terms of M_{env} and T_{bol}. Adding intermediate and high-mass WISH sources to extend the correlation to higher values of L_{bol} and M_{env} shows that these sources follow the same trend with similar slopes with a strong correlation (San José-García et al. 2013). The scatter in the correlation partly reflects the fact that the CO abundance is not constant throughout the envelope and changes with evolutionary stage (see Sect. 6).

5.2. Excitation temperature and comparison with evolutionary models

Figure 16 presents the derived rotational temperatures for ^{12}CO, ^{13}CO and C^{18}O versus M_{env}, T_{bol}, and L_{bol}. In contrast with the integrated intensities, no systematic trend is seen for any parameter. As noted in Sect. 4.2, this lack of change in excitation temperature with evolution is in stark contrast with the evolution of the continuum SED as reflected in the range of T_{bol}.

To investigate whether the lack of evolution in excitation temperature is consistent with our understanding of models of embedded protostars, a series of collapsing envelope and disk formation models with time has been developed by Harsono et al. (2013), based on the formulation of Visser et al. (2009) and Visser & Dullemond (2010). Three different initial conditions are studied. The total mass of the envelope is taken as 1 $M_\odot$ initially in all cases, but different assumptions about the sound speed c_S and initial core angular momentum Ω result in different density structures as a function of time. The three models have $\Omega = 10^{-14}$, 10^{-14}, 10^{-13} s^{-1} and $c_S = 0.26$, 0.19, 0.26 km s^{-1}, respectively, covering the range of parameters expected for low-mass YSOs. The luminosity of the source changes with time from <1 to ~5–10 $L_\odot$. The dust temperature is computed at each time step using a full 2D radiative transfer model and the gas temperature is taken equal to the dust temperature.

Given the model physical structures, the CO excitation is then computed as a function of time (evolution) through full 2D non-LTE excitation plus radiative transfer calculations. The line fluxes are computed for $i = 45°$ inclination but do not depend strongly on the value of i. The resulting line intensities are convolved to a 20″ beam and CO rotational temperatures are computed using the 2–1 up to 10–9 lines. Details are provided in Harsono et al. (2013). The resulting model excitation temperatures are plotted against model L_{bol}, T_{bol}, and M_{env} values as a function of time, with envelope mass decreasing with time. Note
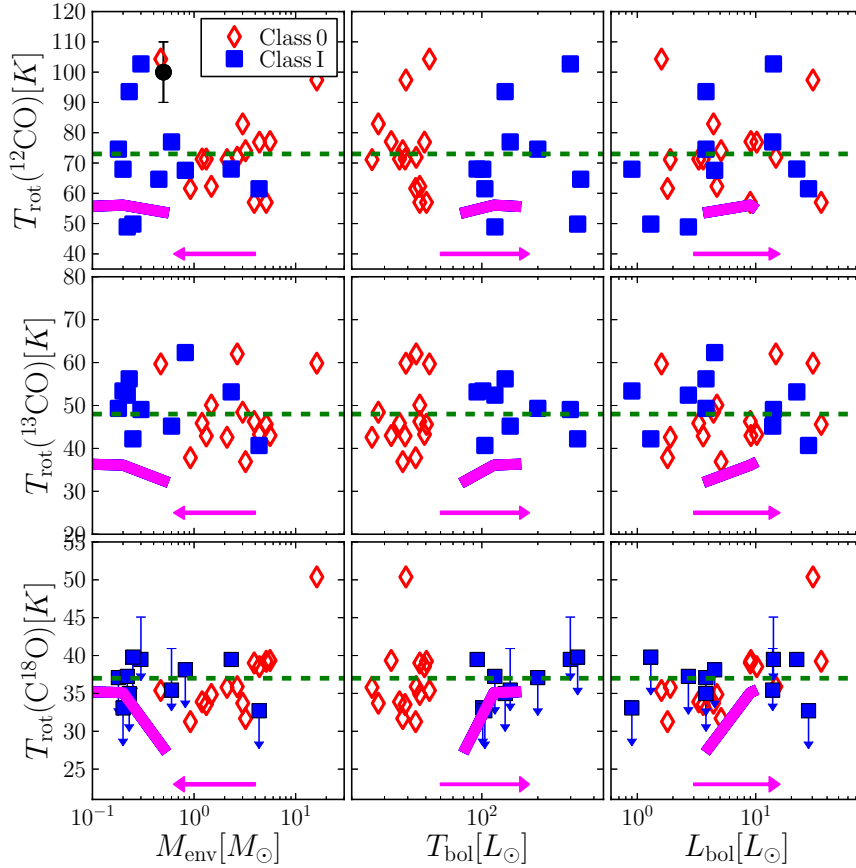
Fig. 16. Calculated rotational temperatures, $T_{\rm rot}$, plotted $M_{\rm env}$, $T_{\rm bol}$, and $L_{\rm bol}$, for ^{12}CO (*top*), ^{13}CO (*middle*), $C^{18}O$ lines (*bottom*). The median excitation temperatures of ~70 K, 48 K and 37 K for ^{12}CO, ^{13}CO and $C^{18}O$, respectively, are indicated with the green dashed lines. Typical error bar for each of the $T_{\rm rot}$ values is shown in the upper left plot, represented in black circle data point. In the $C^{18}O$ plots, blue arrows indicate the upper limits for a number of sources. These figures are compared with disk evolution models of Harsono et al. (2013, magenta solid lines), which represents all three models discussed in the text. Magenta arrows also show the direction of time. The figures show that the excitation temperature does not change with the increasing luminosity, envelope mass or density, confirming that Class 0 and I sources have similar excitation conditions.

that because these models were run for a single $M_{\rm env} = 1\,M_\odot$, they do not cover the full range of observed $M_{\rm env}$.

The first conclusion from this comparison is that the model rotational temperatures hardly show any evolution with time consistent with the observations, in spite of the envelope mass changing by two orders of magnitude. Although the density decreases to values below the critical densities, the temperature increases throughout the envelope so the rotational temperatures stay constant.

The second conclusion is that the model rotational temperatures are generally below the observed temperatures, especially for ^{12}CO (~55 K) and ^{13}CO (~36 K). For ^{12}CO this could be due to the fact that outflow emission is not included in the models, which accounts typically for more than half of the line intensity and has a higher rotational temperature (see Sect. 4.4). Indeed, the rotational temperature of the narrow component is around 60–70 K, closer to the model values. For ^{13}CO, the model $T_{\rm rot}$ values could be lower than the observed values because UV photon heating contributes along the outflow walls (see Visser et al. 2012; Yıldız et al. 2012, for quantitative discussion), although this effect may be small within ~1000 AU radius of the source position itself (Yıldız et al. 2012). The model $C^{18}O$ rotational temperatures are close to the observed values (typically 28–35 K), illustrating that the envelope models are an accurate representation of the observations.

5.3. High-J CO vs. water

Do the average spectra of the Class 0 and Class I sources show any evolution and how does this compare with water? In Fig. 4, stacked and averaged ^{12}CO 3–2, 10–9, and H_2O $1_{10}-1_{01}$ spectra for the Class 0 and I sources have been presented. Consistent

with the discussion in Sect. 3.2 and San José-García et al. (2013), Class 0 sources have broader line widths than Class I sources, showing the importance of protostellar outflows in Class 0 sources. In general, Class I sources show weaker overall emission except for the bright sources GSS30 IRS1 and Elias 29, consistent with the trend in Fig. 15. Figure 17 shows the H_2O $1_{10}-1_{01}$/CO 10–9, H_2O $1_{10}-1_{01}$/CO 3–2, and CO 10–9/CO 3–2 line ratios of the averaged spectra. The CO 10–9/CO 3–2 line wings show increasing ratios from ~0.2 to ~1.0–3.0 for the averaged Class 0 spectrum, but this trend is weaker for the Class I sources which have a near constant ratio of 0.3. The implied kinetic temperature has been discussed in Sect. 4.5.

Franklin et al. (2008) examined the H_2O abundance as a function of velocity by using CO 1–0 as a reference frame. Here it is investigated how H_2O/CO line ratios change with increasing J by using CO 3–2 and 10–9 as reference frames (Fig. 17). In this figure, the CO 3–2 line has been convolved to a 40″ beam using the JCMT data (also done by Kristensen et al. 2012). For the 10–9 line, no map is available so the emission is taken to scale linearly with the beam size, as appropriate for outflow line wings assuming a 1D structure (Tafalla et al. 2010). Thus, the 10–9 intensities are a factor of two lower than those shown in, for example, Fig. 4 where data in a 20″ beam were used. The line wing ratios are computed up to the velocity where the CO emission reaches down to ~2σ noise limit, even though the H_2O line wings extend further.

Consistent with Kristensen et al. (2012), an increasing trend of H_2O/CO 3–2 line ratios with velocity is found for both Class 0 and Class I sources. However, the H_2O/CO 10–9 ratios show little variation with velocity for Class 0 sources, and the ratio is constant within the error bars. For the Class I sources an increasing trend in H_2O/CO 10–9 line ratios is still seen.
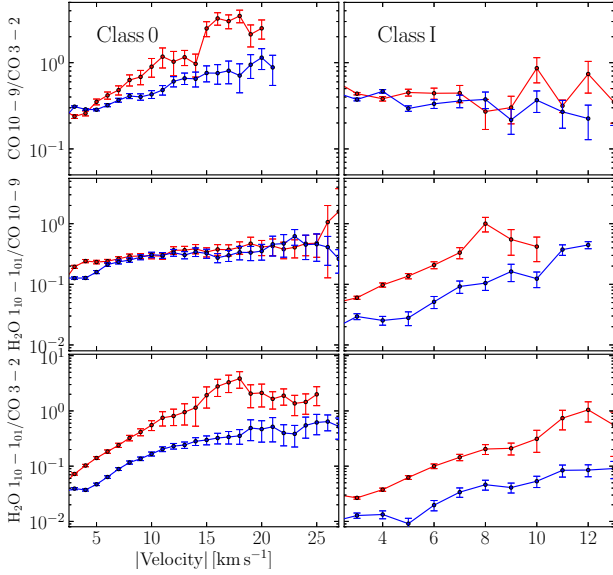
Fig. 17. Blue and red line wing ratios of CO 10–9/3–2 (*top panel*), $H_2O\ 1_{10}–1_{01}$/CO 10–9 (*middle panel*), and $H_2O\ 1_{10}–1_{01}$/CO 3–2 (*bottom panel*) for the composite Class 0 and Class I source spectra. The H_2O/CO 10–9 and H_2O/CO 3–2 ratios are a factor of two lower than shown in Fig. 4 due to the beam size difference of 20″ (CO 10–9 lines) to 40″ ($H_2O\ 1_{10}–1_{01}$ lines).
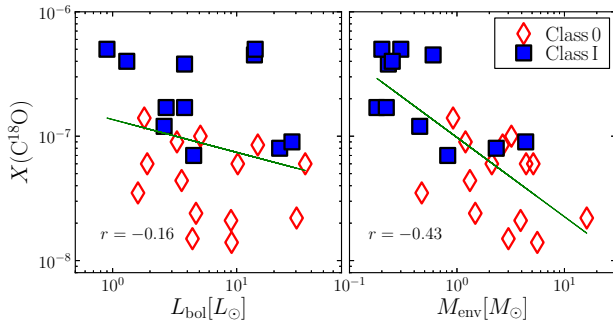

Fig. 18. Constant abundance profiles are fitted to the lower-J $C^{18}O$ 3–2 are shown as function of L_{bol} and M_{env}. Green lines are the best fit to the data points and r values in each of the plots are Pearson correlation coefficient.

Because of the similarity of the CO 10–9 line wings with those of water, it is likely that they are tracing the same warm gas. This is in contrast with the 3–2 line, which probes the colder entrained gas. The conclusion that H_2O and high-J CO emission go together (but not low-J CO) is consistent with recent analyses (Santangelo et al. 2012; Vasta et al. 2012; Tafalla et al. 2013) of WISH data at outflow positions offset from the source. The CO 10–9 line seems to be the lowest J transition whose line wings probe the warm shocked gas rather than the colder entrained outflow gas (see also Sect. 4.3); HIFI observations of higher-J lines up to $J = 16$–15 should show an even closer correspondence between H_2O and CO (Kristensen et al., in prep.). That paper will also present H_2O/CO abundance ratios since deriving those from the data requires further modeling because the H_2O lines are subthermally excited and optically thick.

Table 7. Summary of $C^{18}O$ abundance profiles.

Source	Profile	X_{in}	T_{ev} [K]	X_D	n_{de} [cm^{-3}]	X_0
IRAS 2A[a]	Drop	1.5×10^{-7}	25	$\sim 4 \times 10^{-8}$	7×10^4	5×10^{-7}
IRAS 4A[b]	Drop	$\sim 1 \times 10^{-7}$	25	5.5×10^{-9}	7.5×10^4	5×10^{-7}
IRAS 4B[b]	Jump	3×10^{-7}	25	1×10^{-8}	...	...
Ser-SMM1	Drop	1.5×10^{-7}	25	1.0×10^{-8}	1.4×10^5	5×10^{-7}
Elias29	Constant	5×10^{-7}	...	5×10^{-7}	...	5×10^{-7}
GSS30IRS1	Jump	4×10^{-7}	25	2×10^{-8}	...	...

Notes. X_{in} is the abundance of inner envelope, T_{ev} is the evaporation temperature, X_D drop zone abundance, n_{de} is the desorption density, and X_0 is the abundance of the outermost part of the envelope. See Fig. B.1 in Yıldız et al. (2010) for definition. Results from; [a] Yıldız et al. (2010); [b] Yıldız et al. (2012).

6. CO abundance and warm inner envelope

6.1. CO abundance profiles

The wealth of high quality $C^{18}O$ lines probing a wide range of temperatures allows the CO abundance structure throughout the quiescent envelope to be constrained. The procedure has been described in detail in Yıldız et al. (2010, 2012). Using the density and temperature structure of each envelope as derived by Kristensen et al. (2012, their Table C.1; see Sect. 4.5), the CO abundance profile can be inferred by comparison with the $C^{18}O$ data. The Ratran (Hogerheijde & van der Tak 2000) radiative-transfer modeling code is used to compute line intensities for a given trial abundance structure.

Six sources with clear detections of $C^{18}O$ 9–8 and 10–9 have been modeled. The outer radius of the models is important for the lower-J lines and for Class 0 sources. It is taken to be the radius where either the density n drops to $\sim 1.0 \times 10^4$ cm^{-3}, or the temperature drops below 8–10 K, whichever is reached first. In some Class 0 sources (e.g., IRAS 4A, IRAS 4B), however, the density is still high even at temperatures of ~ 8 K; here the temperature was taken to be constant at 8 K and the density was allowed to drop until $\sim 10^4$ cm^{-3}. The turbulent velocity (Doppler-b parameter) is set to 0.8 km s^{-1}, which is representative of the observed $C^{18}O$ line widths for most sources (Jørgensen et al. 2002) except for Elias 29 where 1.5 km s^{-1} is adopted. The model emission is convolved with the beam in which the line has been observed.

First, constant abundance profiles are fitted to the lower-J $C^{18}O$ 3–2, together with the 2–1 transitions, if available and they are tabulated in Table 5. In Fig. 18, these abundances are plotted as function of bolometric luminosities and envelope masses. Consistent with Jørgensen et al. (2002), Class 0 sources with higher envelope mass have lower average abundances in their envelopes than Class I sources, by more than an order of magnitude. This result is firm for lower-J transitions; however, in order to fit higher-J lines simultaneously, it is necessary to introduce a more complex "drop" abundance profile with a freeze-out zone (Jørgensen et al. 2004). The inner radius is determined by where the dust temperature falls below the CO evaporation temperature of 25 K. The outer radius is determined by where the density becomes too low for freeze-out to occur within the lifetime of the core.

Following Yıldız et al. (2010, 2012) for the NGC 1333 IRAS 2A, IRAS 4A and IRAS 4B protostars, such a drop-abundance profile provides a better fit to the $C^{18}O$ data than a constant or "anti-jump" abundance. In these profiles, X_{in} is

defined as the abundance of the inner envelope down to the evaporation temperature of CO, T_{ev}. The outer abundance X_0 is set to 5×10^{-7} below at a certain desorption density, n_{de}, corresponding to the maximum expected CO abundance of 2.7×10^{-4}. The drop abundance zone is defined as the freeze-out region in the envelope between the limit of T_{ev} and n_{de} (see Fig. B.1 in Yıldız et al. 2010.) Best fit abundances for different sources are summarized in Table 7. As in our previous work and in Fuente et al. (2012) and Alonso-Albi et al. (2010), the CO abundance in the inner envelope is below the canonical value of 2.7×10^{-4} (Lacy et al. 1994) by a factor of a few for the Class 0 sources, probably due to processing of CO to other species on the grains during the cold phase.

Only two of the Class I sources (GSS30 IRS1 and Elias 29) have been observed in deep integrations of $C^{18}O$ 10–9 and therefore they are the only Class I sources modeled in detail. These sources are located in the Ophiuchus molecular cloud, where two low-density foreground sheets contribute to the lowest J 1–0 and 2–1 lines (e.g., Loren 1989; van Kempen et al. 2009d). To take this into account, a single slab foreground cloud is added in front of the protostars with 15 K temperature, 1.5×10^4 cm^{-3} H$_2$ density, and 10^{16} cm^{-2} CO column density. Best-fit models for the $C^{18}O$ 3–2, 5–4, 9–8 and 10–9 lines toward GSS30 IRS1 and Elias 29 can then be well fit with a constant CO abundance close to the canonical value and require at most only a small freeze-out zone (for the case of GSS30 IRS1). Jørgensen et al. (2005b) argue that the size of the freeze-out zone evolves during protostellar evolution, i.e., for Class 0 sources the drop-zone should be much larger than for Class I sources. This is indeed consistent with the results found here. Interestingly, however, the constant or inner abundances X_{in} are high, consistent with the maximum CO gas phase abundance. If these Class I sources went through a previous Class 0 phase with a more massive and colder envelope, apparently less CO ice has been converted to other species during this phase than found for the NGC 1333 sources. One possible explanation is that the dust in this part of Ophiuchus is on average warmer due to the UV radiation from the nearby massive stars. Higher dust temperatures decrease the efficiency of CO hydrogenation because the hydrogen atom has only a short residence time on the grain (Fuchs et al. 2009). Alternatively, the low CO abundance component may have been incorporated to the disk and/or dispersed. Finally, there may be a PDR contribution to the observed intensities (Liseau et al. 2012; Bjerkeli et al. 2012).

6.2. Warm inner envelope

The higher-J $C^{18}O$ transitions such as 9–8 and 10–9 (E_u up to $\sim$300 K) in principle trace directly the warmer gas in the inner envelope. Can we now use these data to put limits on the amount of warm >100 K gas, which could then be used as a reference for determining abundances of complex molecules?

In principle, one could argue that simply summing the observed column density of molecules in each level should provide the total warm column density, as done by Plume et al. (2012) for the case of Orion and in Table 5 based on the rotational diagrams. However, in the low-mass sources considered here freeze-out also plays a role and CO can be converted to other species on the grains. Thus, to convert to $N(H_2)$ in the warm gas, one needs to use the values of X_{in} that have been derived in Table 7. However, these values are derived in the context of a physical model of the source, so in principle one simply recovers the input model.

Besides the complication of the changing CO abundance with radius, there are two other effects that make a direct
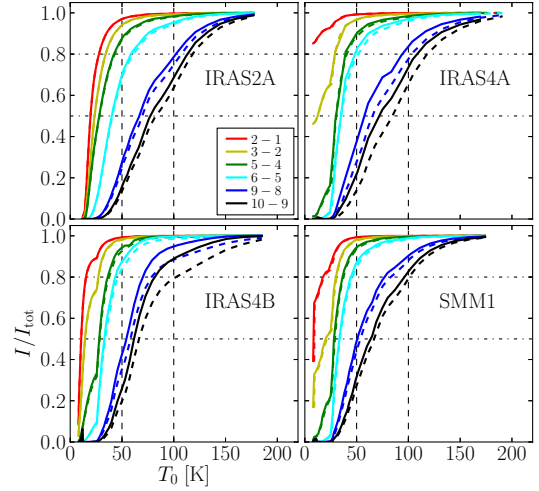
Fig. 19. Cumulative intensity I/I_{tot} for various $C^{18}O$ lines as function of envelope radius (as indicated by the temperature T_o) with the dust opacity included (solid curves), and dust opacity off (dashed curves). The dash-dotted lines indicates the fractions of 50 and 80%, respectively.
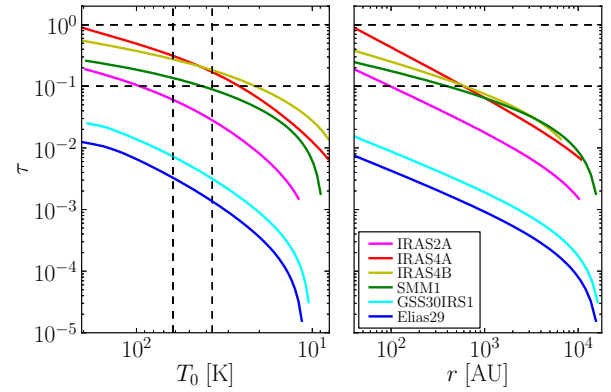
Fig. 20. Dust optical depth at 1 THz as function of envelope radius and temperature. Horizontal dashed lines indicate the $\tau = 1$ and $\tau = 0.1$ values whereas vertical dash-dotted lines are radii, where the temperatures are between 40 K and 60 K.

observational determination of the warm H$_2$ column densities far from simple. The first issue is the fact that not all emission in the 9–8 or 10–9 lines arises from gas at >100 K even though E_u = 237–290 K. Figure 19 shows the cumulative $C^{18}O$ line intensities (solid curves) as functions of radius (or, equivalently, temperature) for four source models. I_{tot} are the intensities measured from the best-fit abundance models as tabulated in Table 7. Thus, the curves represent the fraction of line intensities which have their origins in gas at temperatures below T_0 for the different transitions. As expected, about 90–95% of the $C^{18}O$ emission in the lower-J transitions up to $J_u \leq 3$ comes from gas at <40 K. However, even for the 9–8 transition, 30–50% comes from gas at less than 50 K whereas only $\sim$10–20% originates at temperatures above 100 K. For the 10–9 transition, $\sim$20–40% of the emission comes from >100 K. Thus, these are additional correction factors that would have to be applied to obtain the columns of gas >100 K.

A second potential issue is that the dust continuum at 1 THz may become optically thick so that warm $C^{18}O$ emission cannot escape. Figure 20 shows the dust opacity as function of radius throughout the envelope, obtained by multiplying the column densities with the κ_{dust}(1 THz) (Ossenkopf & Henning 1994, their Table 1, Col. 5) and integrating from the outer edge to each

radius to find the optical depth (τ). It is seen that the dust is optically thin ($\tau < 1$ at 1 THz) throughout the envelopes of our sources except for IRAS 4A, where it reaches unity in the innermost part of the envelope. To what extent is the fraction of high-J emission coming from >100 K affected by the dust? In Fig. 19 (dashed curves), the dust emission has been turned off in the Ratran models. For the lower-J, lower-frequency transitions, almost no difference is found; however, for the higher-J transitions the cumulative intensities are somewhat higher (up to a factor of 2) when no dust is present.

In summary, there are various arguments why warm H_2 column densities cannot be inferred directly from the high-J $C^{18}O$ data. Moreover, all of these arguments use a simple spherically symmetric physical model of the source to quantify the effects. It is known that such models fail on the smaller scales (less than a few hundred AU) due to the presence of a (pseudo)disk and outflow cavities (e.g., Jørgensen et al. 2005a). Spatially resolved data are needed to pin down the structure of the inner envelopes and properly interpret the origin of the high-J $C^{18}O$ emission.

7. Conclusions

We have presented the first large-scale survey of spectrally resolved low- to high-J CO and isotopolog lines ($2 \leq J_{up} \leq 10$) in 26 low-mass young stellar objects by using data from *Herschel*-HIFI, APEX, and JCMT telescopes. Velocity resolved data are the key to obtaining the complete picture of the protostellar envelope and the interaction of the protostar with the environment and follow the evolution from the Class 0 to Class I phase.

- The ^{12}CO line profiles can be decomposed into narrow and broad components, with the relative fractions varying from zero to nearly 100%, with a median of 42% of the $J = 10$–9 emission in the narrow component. The average Class 0 rofile shows a broader, more prominent wing than the average Class I profile.
- The 10–9 together with 3–2 intensities correlate strongly with total luminosity M_{env} and are inversely proportional with bolometric temperature T_{bol}, illustrating the dissipation of the envelope with evolution.
- Rotation diagrams are constructed for each source in order to derive rotational temperatures and column densities. Median temperatures of T_{rot} are 70 K, 48 K, and 37 K, for the ^{12}CO, ^{13}CO and $C^{18}O$ transitions, respectively, for integrated intensities over the entire line ptofiles. The excitation temperatures and SLEDs are very similar for Class 0 and Class I sources in all three isotopologs and do not show any trend with M_{env}, L_{bol} or T_{bol}, in contrast with the continuum SEDs.
- The ^{12}CO 10–9/CO 3–2 intensity ratio as well as the overall rotational temperature generally increase with velocity. The central narrow component due to the quiescent envelope has a lower temperature than the broad outflow component.
- Models of the CO emission from collapsing envelopes reproduce the lack of evolution found in the observed excitation temperatures. They agree quantitatively for $C^{18}O$ but underproduce the ^{12}CO and ^{13}CO excitation temperatures, pointing to the combined effects of outflows and photonheating in boosting these temperatures.
- Comparison of the ^{12}CO profiles with those of H_2O shows that the H_2O 1_{10}–1_{01}/CO 10–9 intensity ratio is nearly constant with velocity for Class 0 sources, contrary to the case

for low-J CO lines. Combined with other findings, this suggests that the CO 10–9 line has contributions from the warmer (~300 K) shocked gas seen in PACS data containing also water, rather than the colder (~100 K) entrained outflow gas traced by low-J CO lines.
- The $C^{18}O$ line intensities give average CO abundances that increase by more than an order of magnitude with decreasing envelope mass from the Class 0 to the Class I phase, consistent with earlier findings. Modeling of the full set of higher-J $C^{18}O$ lines within a given physical model shows further evidence for a freeze-out zone ("drop" abundance profile) in the envelopes of Class 0 sources with an inner CO abundance that is a factor of a few lower than the canonical CO abundance probably due to processing of CO on grains into other molecules. For two Class I sources in Ophiuchus, no freeze-out zone is needed and the data are consistent with a constant high abundance value at a level that is close to the maximum gas-phase CO abundance. The lack of processing for these sources may de due to the higher dust temperatures in Ophiuchus, evolutionary effects, or a PDR contribution.
- The warm (>100 K) H_2 column densities cannot be derived directly from $C^{18}O$ 9–8 or 10–9 lines because of contributions to the emission from colder gas in the envelope, dust extinction at high frequency, and more generally a lack of knowledge of the source structure on a few hundred AU scales.

Overall, our data show that the evolution from the Class 0 to the Class I phase is traced in the decrease of the line intensities reflecting envelope dissipation, a less prominent broad wing indicating a decrease in the outflow power, and an increase in the average CO abundance, reflecting a smaller freeze-out zone. The CO excitation temperature from $J_u = 2$ to 10 shows little evolution between these two classes, however.

The next step in the study of CO in low mass protostars is clearly to obtain higher spectral and spatial resolution data with instruments like ALMA that recover the full range of spatial scales from <100 AU to >1000 AU in both low- and high-J CO and isotopolog lines.
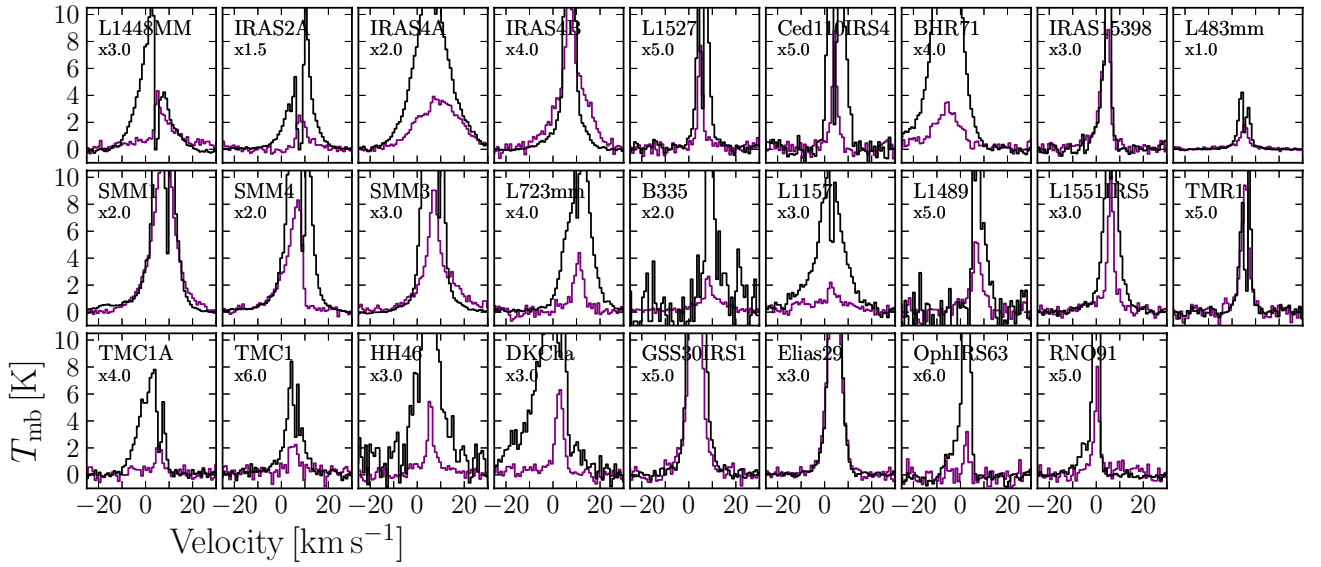
Appendix A: CO 10–9/3–2 spectra

Fig. A.1. Zoom-in spectra of the line wings of ^{12}CO 3–2 (black) and ^{12}CO 10–9 (magenta) overplotted for each source. The spectra are multiplied by a constant factor indicated in the figure in order to show the line wings in more detail. They have been rebinned to 0.6–1 km s^{-1}, to enhance signal-to-noise.

Appendix B: Observations matrix

Table B.1. Observed sources and lines.

Source	12CO 2–1	3–2	4–3	6–5	7–6	10–9	13CO 2–1	3–2	4–3	6–5	8–7	10–9	C18O 2–1	3–2	5–4	6–5	9–8	10–9
L1448-MM	JCMT	JCMT	JCMT	. . . ^{a}	. . . ^{a}	HIFI	JCMT	JCMT	. . .	APEX	. . .	HIFI	JCMT	JCMT	HIFI	. . .	HIFI	HIFI
NGC 1333-IRAS 2A	JCMT	JCMT	JCMT	APEX	APEX	HIFI	. . .	JCMT	JCMT	APEX	. . .	HIFI	JCMT	JCMT	HIFI	APEX	HIFI	HIFI
NGC 1333-IRAS 4A	JCMT	JCMT	JCMT	APEX	APEX	HIFI	JCMT	JCMT	JCMT	APEX	HIFI	HIFI	JCMT	JCMT	HIFI	APEX	HIFI	HIFI
NGC 1333-IRAS 4B	JCMT	JCMT	JCMT	APEX	APEX	HIFI	. . .	JCMT	. . .	APEX	HIFI	HIFI	JCMT	JCMT	HIFI	APEX	HIFI	HIFI
L1527	JCMT	JCMT	JCMT	APEX	APEX	HIFI	. . .	JCMT	JCMT	APEX	HIFI	HIFI	JCMT	JCMT	HIFI	. . .	HIFI	. . .
Ced110-IRS4	. . .	APEX	APEX	APEX	APEX	HIFI	. . .	. . .	. . .	APEX	. . .	HIFI	. . .	. . .	. . .	. . .	HIFI	. . .
BHR71	. . .	APEX	. . .	APEX	APEX	HIFI	. . .	. . .	. . .	APEX	. . .	HIFI	. . .	APEX	HIFI	. . .	HIFI	. . .
IRAS 15398	. . .	JCMT	JCMT	APEX	APEX	HIFI	. . .	JCMT	. . .	APEX	. . .	HIFI	JCMT	JCMT	HIFI	. . .	HIFI	. . .
L483 mm	JCMT	JCMT	JCMT	APEX	APEX	HIFI	JCMT	JCMT	JCMT	APEX	. . .	HIFI	JCMT	JCMT	HIFI	. . .	HIFI	HIFI
Ser-SMM1	JCMT	JCMT	JCMT	APEX	APEX	HIFI	JCMT	JCMT	. . .	APEX	HIFI	HIFI	JCMT	JCMT	HIFI	APEX	HIFI	HIFI
Ser-SMM4	JCMT	JCMT	JCMT	APEX	APEX	HIFI	. . .	JCMT	. . .	APEX	HIFI	HIFI	. . .	JCMT	HIFI	. . .	HIFI	HIFI
Ser-SMM3	JCMT	JCMT	JCMT	APEX	APEX	HIFI	JCMT	JCMT	. . .	APEX	APEX	HIFI	JCMT	JCMT	HIFI	. . .	HIFI	HIFI
L723	. . .	JCMT	. . .	APEX	APEX	HIFI	JCMT	JCMT	JCMT	APEX	APEX	HIFI	JCMT	JCMT	HIFI	. . .	HIFI	. . .
B335	JCMT	JCMT	JCMT	APEX	APEX	HIFI	JCMT	JCMT	. . .	APEX	. . .	HIFI	JCMT	JCMT	HIFI	. . .	HIFI	. . .
L1157	JCMT	JCMT	JCMT	JCMT	. . .	HIFI	JCMT	JCMT	. . .	JCMT	. . .	HIFI	JCMT	JCMT	HIFI	. . .	HIFI	. . .
L1489	JCMT	JCMT	JCMT	APEX	APEX	HIFI	. . .	JCMT	. . .	APEX	. . .	HIFI	JCMT	JCMT	. . .	. . .	HIFI	. . .
L1551-IRS5	JCMT	JCMT	JCMT	APEX	. . .	HIFI	JCMT	JCMT	. . .	APEX	. . .	HIFI	JCMT	JCMT	. . .	. . .	HIFI	. . .
TMR1	JCMT	JCMT	JCMT	APEX	APEX	HIFI	. . .	JCMT	. . .	APEX	. . .	HIFI	JCMT	JCMT	. . .	. . .	HIFI	. . .
TMC1A	JCMT	JCMT	JCMT	APEX	APEX	HIFI	. . .	JCMT	. . .	APEX	. . .	HIFI	JCMT	JCMT	. . .	. . .	HIFI	. . .
TMC1	JCMT	JCMT	JCMT	APEX	APEX	HIFI	. . .	JCMT	. . .	APEX	. . .	HIFI	JCMT	JCMT	. . .	. . .	HIFI	. . .
HH46-IRS	APEX	APEX	APEX	APEX	APEX	HIFI	. . .	APEX	APEX	APEX	APEX	HIFI	JCMT	APEX	. . .	APEX	HIFI	. . .
DK Cha	. . .	APEX	APEX	APEX	APEX	HIFI	. . .	. . .	APEX	APEX	APEX	HIFI	APEX	APEX	. . .	APEX	HIFI	. . .
GSS30-IRS1	JCMT	JCMT	. . .	APEX	. . .	HIFI	JCMT	JCMT	. . .	APEX	. . .	HIFI	JCMT	JCMT	. . .	. . .	HIFI	. . .
Elias 29	JCMT	JCMT	. . .	APEX	. . .	HIFI	JCMT	JCMT	. . .	APEX	. . .	HIFI	JCMT	JCMT	HIFI	. . .	HIFI	. . .
Oph-IRS63	JCMT	JCMT	. . .	APEX	APEX	HIFI	. . .	JCMT	. . .	APEX	APEX	HIFI	JCMT	JCMT	. . .	. . .	HIFI	. . .
RNO91	JCMT	JCMT	. . .	APEX	APEX	HIFI	JCMT	JCMT	. . .	APEX	APEX	HIFI	JCMT	JCMT	. . .	. . .	HIFI	. . .

Notes. Sources above the horizontal line are Class 0, sources below are Class I. HIFI indicates *Herschel*-HIFI observations. $^{(a)}$ Gomez-Ruiz et al. (in prep).

References

Alonso-Albi, T., Fuente, A., Crimier, N., et al. 2010, A&A, 518, A52

André, P., Ward-Thompson, D., & Barsony, M. 2000, Protostars & Planets IV, 59

Arce, H. G., Shepherd, D., Gueth, F., et al. 2007, Protostars and Planets V, 245

Bachiller, R., & Perez Gutierrez, M. 1997, ApJ, 487, L93

Bachiller, R., Martin-Pintado, J., Tafalla, M., Cernicharo, J., & Lazareff, B. 1990, A&A, 231, 174

Bjerkeli, P., Liseau, R., Larsson, B., et al. 2012, A&A, 546, A29

Blake, G. A., Sandell, G., van Dishoeck, E. F., et al. 1995, ApJ, 441, 689

Bontemps, S., André, P., Terebey, S., & Cabrit, S. 1996, A&A, 311, 858

Bourke, T. L., Garay, G., Lehtinen, K. K., et al. 1997, ApJ, 476, 781

Buckle, J. V., Hills, R. E., Smith, H., et al. 2009, MNRAS, 399, 1026

Ceccarelli, C., Caselli, P., Herbst, E., Tielens, A. G. G. M., & Caux, E. 2007, Protostars and Planets V, 47

Chen, H., Myers, P. C., Ladd, E. F., & Wood, D. O. S. 1995, ApJ, 445, 377

de Graauw, T., Helmich, F. P., Phillips, T. G., et al. 2010, A&A, 518, L6

Franklin, J., Snell, R. L., Kaufman, M. J., et al. 2008, ApJ, 674, 1015

Fuchs, G. W., Cuppen, H. M., Ioppolo, S., et al. 2009, A&A, 505, 629

Fuente, A., Caselli, P., McCoey, C., et al. 2012, A&A, 540, A75

Fuller, G. A., & Ladd, E. F. 2002, ApJ, 573, 699

Goicoechea, J. R., Cernicharo, J., Karska, A., et al. 2012, A&A, 548, A77
Goldsmith, P. F., & Langer, W. D. 1999, ApJ, 517, 209
Green, J. D., Evans, II, N. J., Jørgensen, J. K., et al. 2013, ApJ, 770, 123
Gregersen, E. M., Evans, II, N. J., Zhou, S., & Choi, M. 1997, ApJ, 484, 256
Griffin, M. J., Abergel, A., Abreu, A., et al. 2010, A&A, 518, L3
Güsten, R., Baryshev, A., Bell, A., et al. 2008, in SPIE Conf. Ser., 7020
Harsono, D., Visser, R., Bruderer, S., et al. 2013, A&A, 555, A45
Hatchell, J., Richer, J. S., Fuller, G. A., et al. 2005, A&A, 440, 151
Hayashi, M., Hasegawa, T., Ohashi, N., & Sunada, K. 1994, ApJ, 426, 234
Herczeg, G. J., Karska, A., Bruderer, S., et al. 2012, A&A, 540, A84
Hogerheijde, M. R., & van der Tak, F. F. S. 2000, A&A, 362, 697
Jørgensen, J. K., Schöier, F. L., & van Dishoeck, E. F. 2002, A&A, 389, 908
Jørgensen, J. K., Schöier, F. L., & van Dishoeck, E. F. 2004, A&A, 416, 603
Jørgensen, J. K., Schöier, F. L., & van Dishoeck, E. F. 2005a, A&A, 437, 501
Jørgensen, J. K., Schöier, F. L., & van Dishoeck, E. F. 2005b, A&A, 435, 177
Karska, A., Herczeg, G. J., van Dishoeck, E. F., et al. 2013, A&A, 552, A141
Kasemann, C., Güsten, R., Heyminck, S., et al. 2006, in SPIE Conf. Ser., 6275
Kristensen, L. E., van Dishoeck, E. F., Tafalla, M., et al. 2011, A&A, 531, L1
Kristensen, L. E., van Dishoeck, E. F., Bergin, E. A., et al. 2012, A&A, 542, A8
Kutner, M. L., & Ulich, B. L. 1981, ApJ, 250, 341
Lacy, J. H., Knacke, R., Geballe, T. R., & Tokunaga, A. T. 1994, ApJ, 428, L69
Lada, C. J. 1999, in NATO ASIC Proc. 540: The Origin of Stars and Planetary
    Systems, eds. C. J. Lada, & N. D. Kylafis, 143
Langer, W. D., & Penzias, A. A. 1990, ApJ, 357, 477
Liseau, R., Goldsmith, P. F., Larsson, B., et al. 2012, A&A, 541, A73
Loren, R. B. 1989, ApJ, 338, 902
Manoj, P., Watson, D. M., Neufeld, D. A., et al. 2013, ApJ, 763, 83
Müller, H. S. P., Schlöder, F., Stutzki, J., & Winnewisser, G. 2005, J. Mol. Struct.,
    742, 215
Myers, P. C., & Ladd, E. F. 1993, ApJ, 413, L47
Myers, P. C., Evans, II, N. J., & Ohashi, N. 2000, Protostars and Planets IV, 217
Ossenkopf, V., & Henning, T. 1994, A&A, 291, 943
Ott, S. 2010, in Astronomical Data Analysis Software and Systems XIX, eds.
    Y. Mizumoto, K.-I. Morita, & M. Ohishi, ASP Conf. Ser., 434, 139
Pickett, H. M., Poynter, R. L., Cohen, E. A., et al. 2010, J. Quant. Spect. Radiat.
    Trans., 111, 1617
Pilbratt, G. L., Riedinger, J. R., Passvogel, T., et al. 2010, A&A, 518, L1
Plume, R., Bergin, E. A., Phillips, T. G., et al. 2012, ApJ, 744, 28
Poglitsch, A., Waelkens, C., Geis, N., et al. 2010, A&A, 518, L2
Robitaille, T. P., Whitney, B. A., Indebetouw, R., Wood, K., & Denzmore, P.
    2006, ApJS, 167, 256

Roelfsema, P. R., Helmich, F. P., Teyssier, D., et al. 2012, A&A, 537, A17
San José-García, I., Mottram, J. C., Kristensen, L. E., et al. 2013, A&A, 553,
    A125
Santangelo, G., Nisini, B., Giannini, T., et al. 2012, A&A, 538, A45
Schöier, F. L., van der Tak, F. F. S., van Dishoeck, E. F., & Black, J. H. 2005,
    A&A, 432, 369
Shirley, Y. L., Evans, II, N. J., Rawlings, J. M. C., & Gregersen, E. M. 2000,
    ApJS, 131, 249
Spaans, M., Hogerheijde, M. R., Mundy, L. G., & van Dishoeck, E. F. 1995,
    ApJ, 455, L167
Tachihara, K., Onishi, T., Mizuno, A., & Fukui, Y. 2002, A&A, 385, 909
Tafalla, M., Santiago-García, J., Hacar, A., & Bachiller, R. 2010, A&A, 522,
    A91
Tafalla, M., Liseau, R., Nisini, B., et al. 2013, A&A, 551, A116
van der Tak, F. F. S., Black, J. H., Schöier, F. L., Jansen, D. J., & van Dishoeck,
    E. F. 2007, A&A, 468, 627
van Dishoeck, E. F., & Blake, G. A. 1998, ARA&A, 36, 317
van Dishoeck, E. F., Kristensen, L. E., Benz, A. O., et al. 2011, PASP, 123, 138
van Kempen, T. A., Hogerheijde, M. R., van Dishoeck, E. F., et al. 2006, A&A,
    454, L75
van Kempen, T. A., van Dishoeck, E. F., Güsten, R., et al. 2009a, A&A, 507,
    1425
van Kempen, T. A., van Dishoeck, E. F., Güsten, R., et al. 2009b, A&A, 501, 633
van Kempen, T. A., van Dishoeck, E. F., Hogerheijde, M. R., & Güsten, R. 2009c,
    A&A, 508, 259
van Kempen, T. A., van Dishoeck, E. F., Salter, D. M., et al. 2009d, A&A, 498,
    167
van Kempen, T. A., Kristensen, L. E., Herczeg, G. J., et al. 2010, A&A, 518,
    L121
Vasta, M., Codella, C., Lorenzani, A., et al. 2012, A&A, 537, A98
Visser, R., & Dullemond, C. P. 2010, A&A, 519, A28
Visser, R., van Dishoeck, E. F., Doty, S. D., & Dullemond, C. P. 2009, A&A,
    495, 881
Visser, R., Kristensen, L. E., Bruderer, S., et al. 2012, A&A, 537, A55
Vladilo, G., Centurion, M., & Cassola, C. 1993, A&A, 273, 239
Wilson, T. L., & Rood, R. 1994, ARA&A, 32, 191
Yang, B., Stancil, P. C., Balakrishnan, N., & Forrey, R. C. 2010, ApJ, 718,
    1062
Yıldız, U. A., van Dishoeck, E. F., Kristensen, L. E., et al. 2010, A&A, 521, L40
Yıldız, U. A., Kristensen, L. E., van Dishoeck, E. F., et al. 2012, A&A, 542, A86
Young, C. H., & Evans, II, N. J. 2005, ApJ, 627, 293

Appendix C: CO spectra of sample

C.1. L1448MM
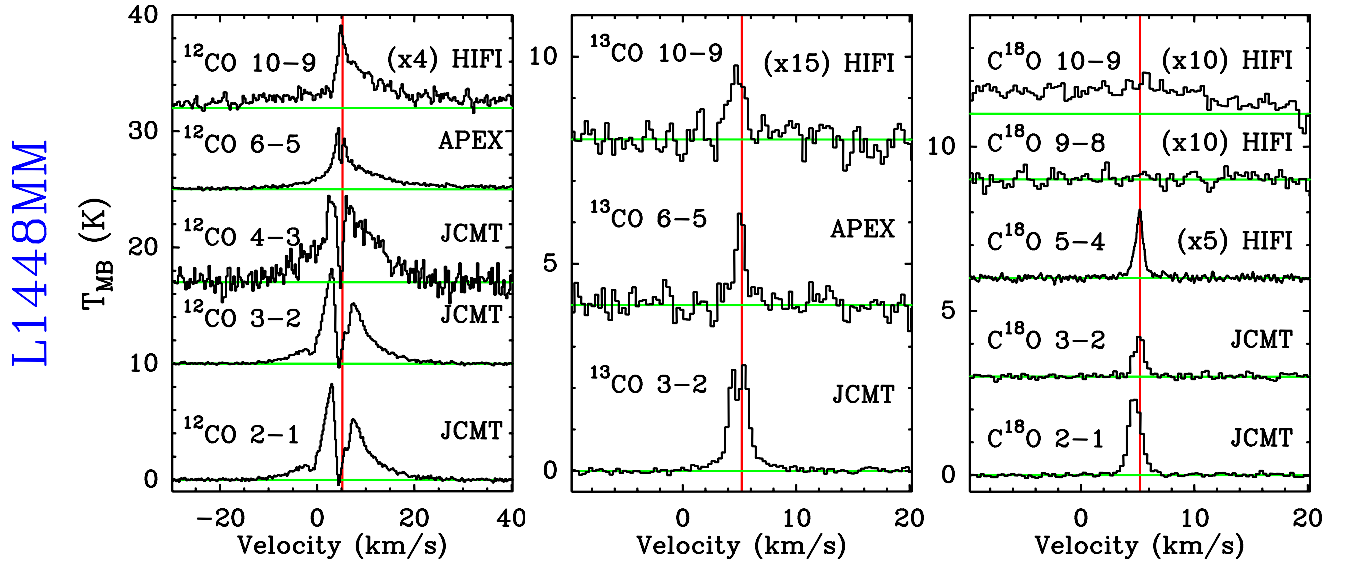
Fig. C.1. Observed ^{12}CO, ^{13}CO, and $C^{18}O$ transitions for L1448MM.

Table C.1. Observed line intensities for L1448MM in all observed transitions.

Mol.	Transition	Telescope	Efficiency η	$\int T_{MB}dV$ [K km s^{-1}]	T_{peak} [K]	rms [K]
CO	2–1	JCMT-RxA	0.69	59.71	8.26	0.10
	3–2	JCMT-HARPB	0.63	32.15	4.20	0.085
	4–3	JCMT	0.38	87.49	7.45	0.77
	6–5[a]	APEX-CHAMP$^+$	0.46	46.15	5.67	0.12
	10–9	*Herschel*-HIFI[b]	0.64	21.53	. . .	0.15
^{13}CO	2–1	JCMT-RxA	0.74	9.84	6.50	0.066
	3–2	JCMT-HARPB	0.63	5.74	2.70	0.065
	6–5	APEX-CHAMP$^+$	0.48	2.88	2.69	0.34
	10–9	*Herschel*-HIFI[b]	0.74	0.34	0.13	0.019
$C^{18}O$	2–1	JCMT-RxA	0.69	3.53	2.35	0.061
	3–2	JCMT-HARPB	0.63	1.47	1.48	0.10
	5–4	*Herschel*-HIFI[b]	0.76	0.42	0.45	0.018
	9–8	*Herschel*-HIFI[c]	0.74	<0.052	. . .	0.023
	10–9	*Herschel*-HIFI[c]	0.74	<0.055	. . .	0.024

Notes. [a] Gomez-Ruiz et al. (in prep.) [b] Only H-polarization observation is used. [c] H- and V-polarization observations averaged.

C.2. IRAS2A

Fig. C.2. Observed ^{12}CO, ^{13}CO, and C^{18}O transitions for IRAS 2A.

Table C.2. Observed line intensities for IRAS 2A in all observed transitions.

Mol.	Transition	Telescope	Efficiency η	$\int T_{MB}dV$ [K km s^{-1}]	T_{peak} [K]	rms [K]
CO	2–1	JCMT-RxA	0.69	129.70	20.54	0.083
	3–2	JCMT-HARPB	0.63	46.93	9.38	0.061
	4–3	JCMT[a]	0.38	180.00	23.67	0.55
	6–5	APEX-CHAMP$^+$	0.52	55.02	8.89	0.60
	7–6	APEX-CHAMP$^+$	0.49	37.39	6.35	1.29
	10–9	*Herschel*-HIFI[b]	0.64	9.20	1.80	0.14
^{13}CO	2–1	JCMT-RxA	0.69	19.25	3.95	0.10
	3–2	JCMT-HARPB	0.63	8.48	2.66	0.078
	6–5	APEX-CHAMP$^+$	0.52	7.08	3.95	0.15
	8–7	*Herschel*-HIFI[c]	0.75	1.37	0.66	0.005
	10–9	*Herschel*-HIFI[b]	0.74	0.61	0.30	0.030
C^{18}O	2–1	JCMT-RxA	0.69	6.00	2.81	0.15
	3–2	JCMT-HARPB	0.63	2.78	2.10	0.10
	5–4	*Herschel*-HIFI[b]	0.76	0.78	0.67	0.013
	6–5	APEX-CHAMP$^+$	0.56	3.58	2.09	0.27
	9–8	*Herschel*-HIFI[c]	0.74	0.19	0.090	0.020
	10–9	*Herschel*-HIFI[b]	0.74	0.15	0.046	0.009

Notes. [a] Taken in 11″ beam. [b] Only H-polarization observation is used. [c] H- and V-polarization observations averaged.

C.3. IRAS4A

Fig. C.3. Observed ^{12}CO, ^{13}CO, and C^{18}O transitions for IRAS 4A.

Table C.3. Observed line intensities for IRAS4A in all observed transitions.

Mol.	Transition	Telescope	Efficiency η	$\int T_{MB}dV$ [K km s^{-1}]	T_{peak} [K]	rms [K]
CO	2–1	JCMT-RxA	0.69	116.49	18.43	0.11
	3–2	JCMT-HARPB	0.63	132.56	18.85	0.070
	4–3	JCMT[a]	0.38	194.25	23.78	0.92
	6–5	APEX-CHAMP$^+$	0.48	84.23	10.03	0.27
	7–6	APEX-CHAMP$^+$	0.45	55.00	17.04	4.39
	10–9	*Herschel*-HIFI[b]	0.64	52.16	2.31	0.18
^{13}CO	2–1	JCMT-RxA	0.74	39.30	7.57	0.15
	3–2	JCMT-HARPB	0.63	11.43	4.49	0.078
	4–3	JCMT[a]	0.38	15.19	7.35	0.78
	6–5	APEX-CHAMP$^+$	0.52	7.03	2.61	0.20
	8–7	*Herschel*-HIFI[c]	0.75	2.14	0.38	0.009
	10–9	*Herschel*-HIFI[c]	0.74	0.66	0.16	0.022
C^{18}O	2–1	JCMT-RxA	0.69	4.90	2.70	0.23
	3–2	JCMT-HARPB	0.63	2.54	2.30	0.22
	5–4	*Herschel*-HIFI[d]	0.76	0.61	0.37	0.010
	6–5	APEX-CHAMP$^+$	0.48	3.00	2.00	0.26
	9–8	*Herschel*-HIFI[c]	0.74	0.17	0.050	0.023
	10–9	*Herschel*-HIFI[e]	0.74	0.045	0.023	0.008

Notes. The values given here are calculated for 20″ beam, therefore values are slightly different than Yıldız et al. (2012). [a] Taken in 11″ beam. [b] *Herschel* observation corrected for the chopped emission and only H polarization observation is used. [c] H- and V-polarization observations averaged. [d] Only H-polarization observation is used. [e] Observed by open time program OT2_rvisser_2. H- and V-polarization observations averaged.
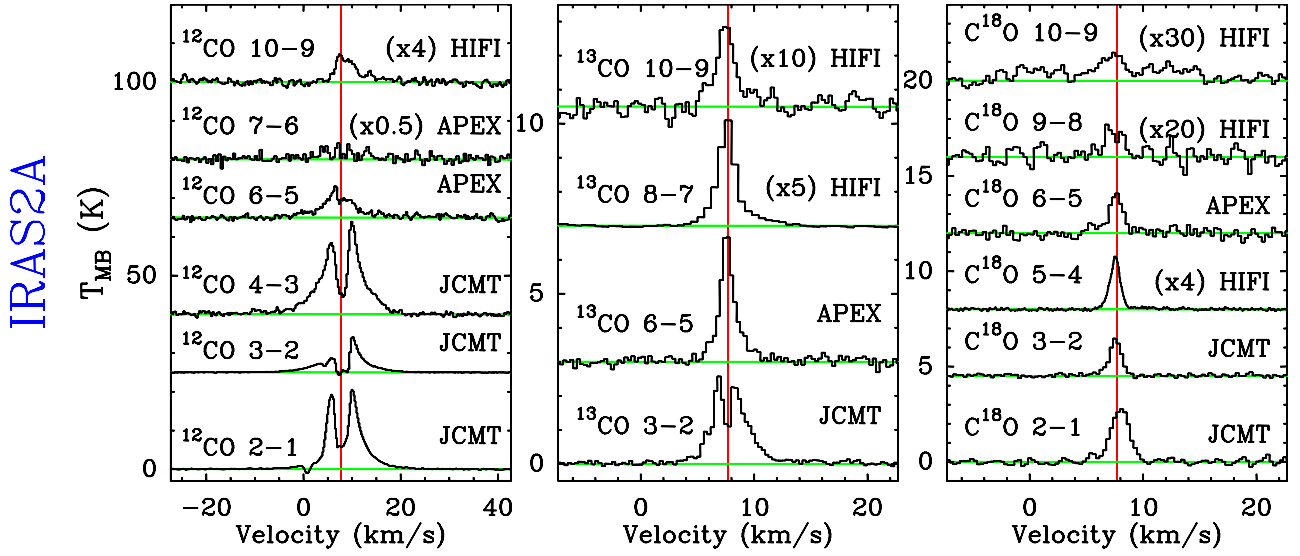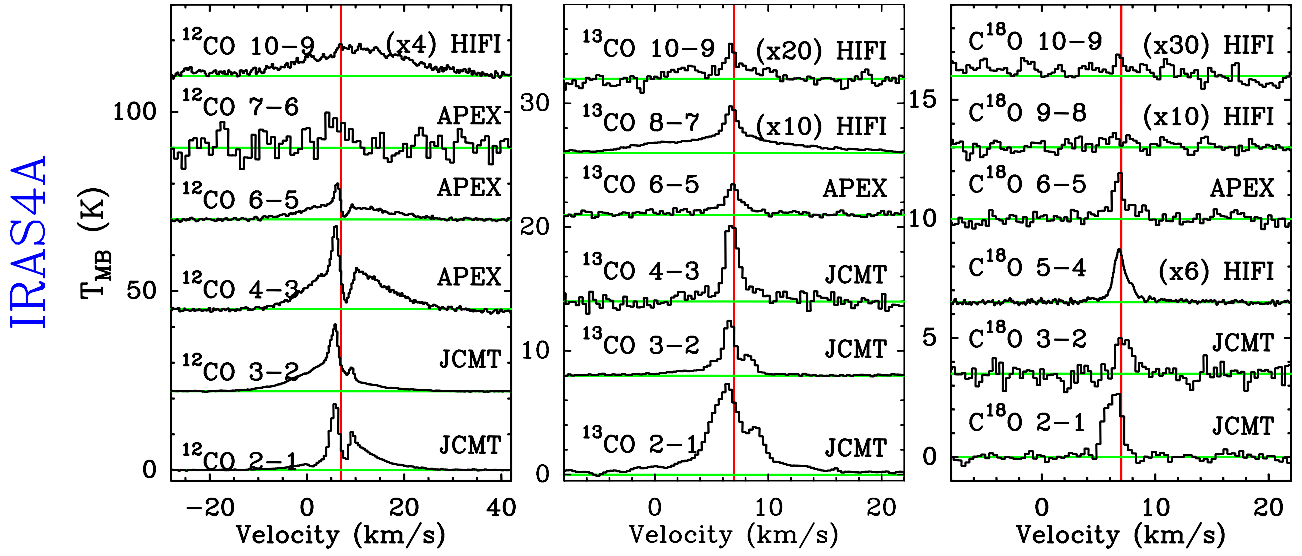
C.4. IRAS4B

Fig. C.4. Observed ^{12}CO, ^{13}CO, and C^{18}O transitions for IRAS 4B.

Table C.4. Observed line intensities for IRAS4B in all observed transitions.

Mol.	Transition	Telescope	Efficiency η	$\int T_{MB}dV$ [K km s^{-1}]	T_{peak} [K]	rms [K]
CO	2–1	JCMT-RxA	0.69	54.70	13.94	0.070
	3–2	JCMT-HARPB	0.63	53.89	10.39	0.034
	4–3	JCMT[a]	0.38	115.19	14.38	0.26
	6–5	APEX-CHAMP$^+$	0.48	35.17	6.29	0.29
	7–6	APEX-CHAMP$^+$	0.45	<35.00	...	4.51
	10–9	*Herschel*-HIFI[b]	0.64	29.17	2.96	0.10
^{13}CO	3–2	JCMT-HARPB	0.63	5.90	2.32	0.023
	6–5	APEX-CHAMP$^+$	0.52	2.20	1.03	0.10
	8–7	*Herschel*-HIFI[c]	0.75	0.73	0.25	0.009
	10–9	*Herschel*-HIFI[c]	0.74	0.53	0.15	0.021
C^{18}O	2–1	JCMT-RxA	0.69	5.30	2.50	0.16
	3–2	JCMT-HARPB	0.63	2.36	1.70	0.30
	5–4	*Herschel*-HIFI[d]	0.76	0.33	0.21	0.014
	6–5	APEX-CHAMP$^+$	0.48	1.35	0.82	0.22
	9–8	*Herschel*-HIFI[c]	0.74	<0.024	...	0.022
	10–9	*Herschel*-HIFI[e]	0.74	0.059	0.04	0.009

Notes. The values given here are calculated for 20″ beam, therefore values are slightly different than Yıldız et al. (2012). [a] Taken in 11″ beam. [b] *Herschel* observation corrected for the chopped emission and only H polarization observation is used. [c] H- and V-polarization observations averaged. [d] Only H-polarization observation is used. [e] Observed by open time program OT2_rvisser_2. H- and V-polarization observations averaged.
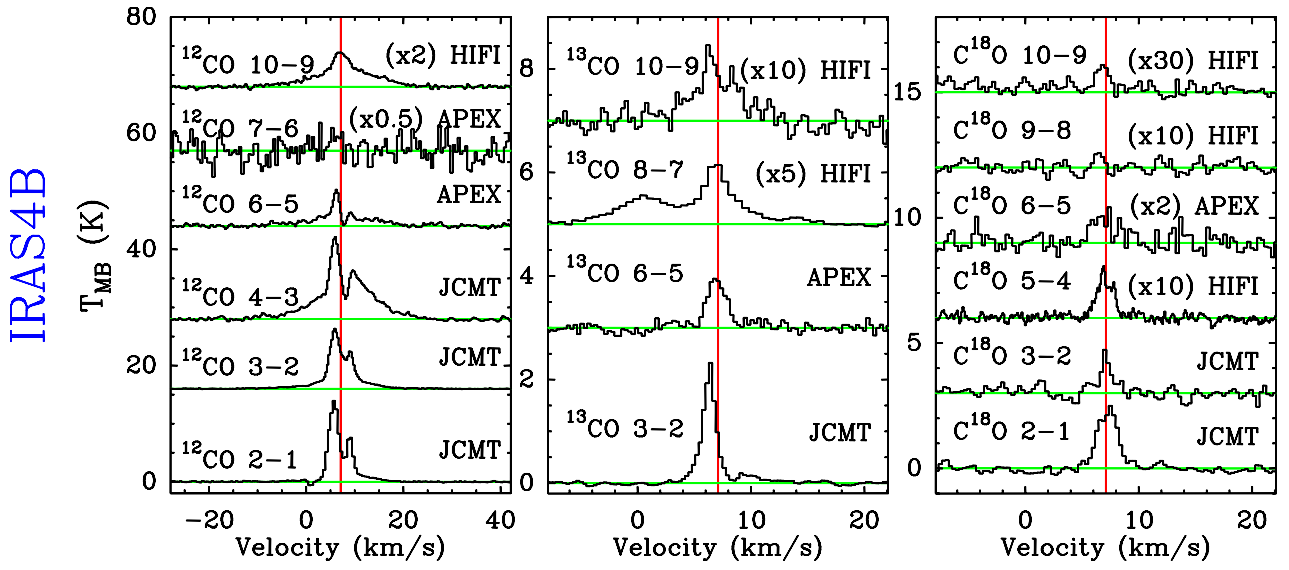
C.5. L1527

Fig. C.5. Observed ^{12}CO, ^{13}CO, and C^{18}O transitions for L1527.

Table C.5. Observed line intensities for L1527 in all observed transitions.

Mol.	Transition	Telescope	Efficiency η	$\int T_{MB}dV$ [K km s^{-1}]	T_{peak} [K]	rms [K]
CO	2–1	JCMT-RxA	0.69	38.14	14.04	0.086
	3–2	JCMT-HARPB	0.63	19.38	6.90	0.12
	4–3	JCMT[a]	0.38	63.64	16.39	0.46
	6–5	APEX-CHAMP$^+$	0.52	38.02	14.88	0.33
	7–6	APEX-CHAMP$^+$	0.49	31.90	11.82	0.85
	10–9	*Herschel*-HIFI[b]	0.64	5.17	2.00	0.12
^{13}CO	2–1	JCMT-RxA	0.69	12.12	4.92	0.085
	3–2	JCMT-HARPB	0.63	4.72	2.71	0.073
	4–3	JCMT[a]	0.38	12.12	6.40	0.089
	6–5	APEX-CHAMP$^+$	0.48	4.72	2.35	0.51
	10–9	*Herschel*-HIFI[b]	0.76	0.12	0.06	0.019
C^{18}O	2–1	JCMT-RxA	0.69	4.55	3.89	0.11
	3–2	JCMT-HARPB	0.63	1.54	1.90	0.10
	5–4	*Herschel*-HIFI[b]	0.76	0.49	0.35	0.009
	9–8	*Herschel*-HIFI[c]	0.74	<0.050	...	0.022

Notes. [a] Taken in 11″ beam. [b] Only H-polarization observation is used. [c] H- and V-polarization observations averaged.

C.6. Ced110IRS4
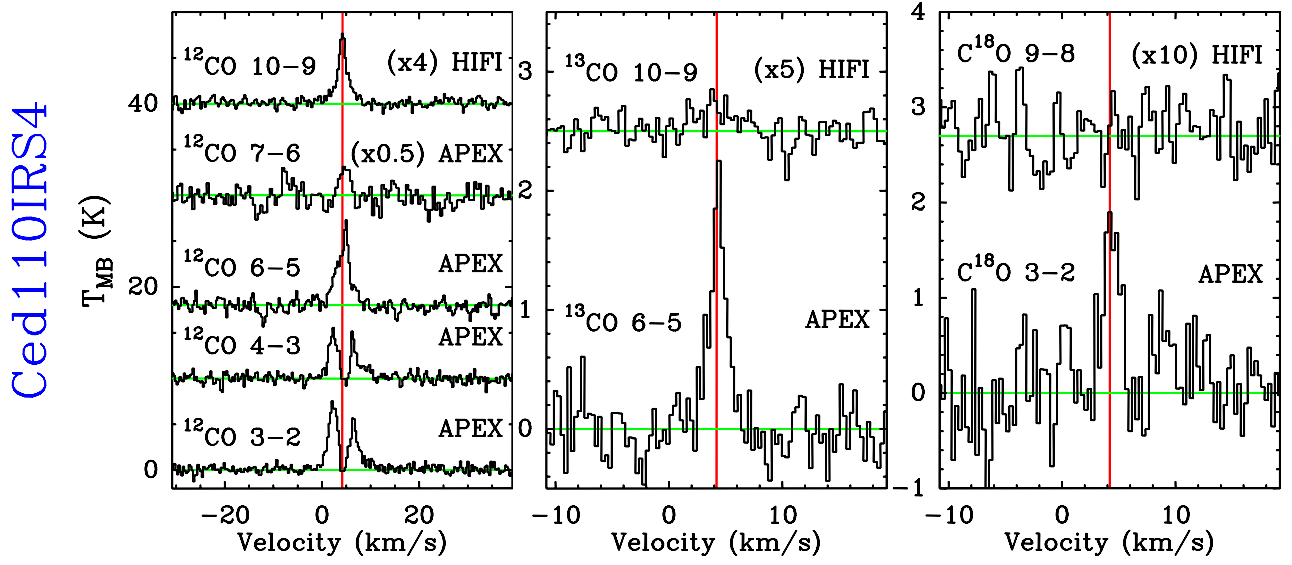
Fig. C.6. Observed ^{12}CO, ^{13}CO, and C^{18}O transitions for Ced110-IRS4.

Table C.6. Observed line intensities for Ced110-IRS4 in all observed transitions.

Mol.	Transition	Telescope	Efficiency η	$\int T_{MB}dV$ [K km s^{-1}]	T_{peak} [K]	rms [K]
CO	3–2	APEX	0.73	31.14	7.70	0.35
	4–3	APEX	0.60	20.00	5.70	0.62
	6–5	APEX-CHAMP$^+$	0.45	24.42	10.36	0.71
	7–6	APEX-CHAMP$^+$	0.42	18.23	6.82	1.49
	10–9	*Herschel*-HIFI[a]	0.66	5.08	1.92	0.12
^{13}CO	6–5	APEX-CHAMP$^+$	0.45	2.98	2.70	0.30
	10–9	*Herschel*-HIFI[a]	0.74	0.12	0.08	0.027
C^{18}O	3–2	APEX–2a	0.73	3.10	1.90	0.47
	9–8	*Herschel*-HIFI[a]	0.74	<0.059	. . .	0.026

Notes. [a] H- and V-polarization observations averaged.
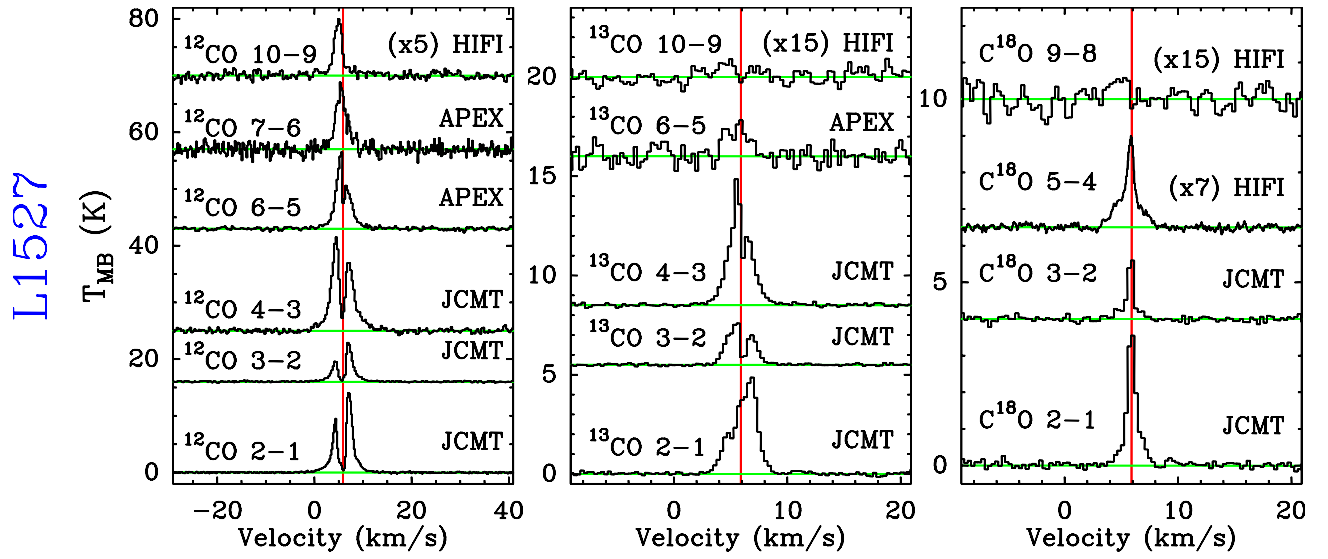
C.7. BHR71
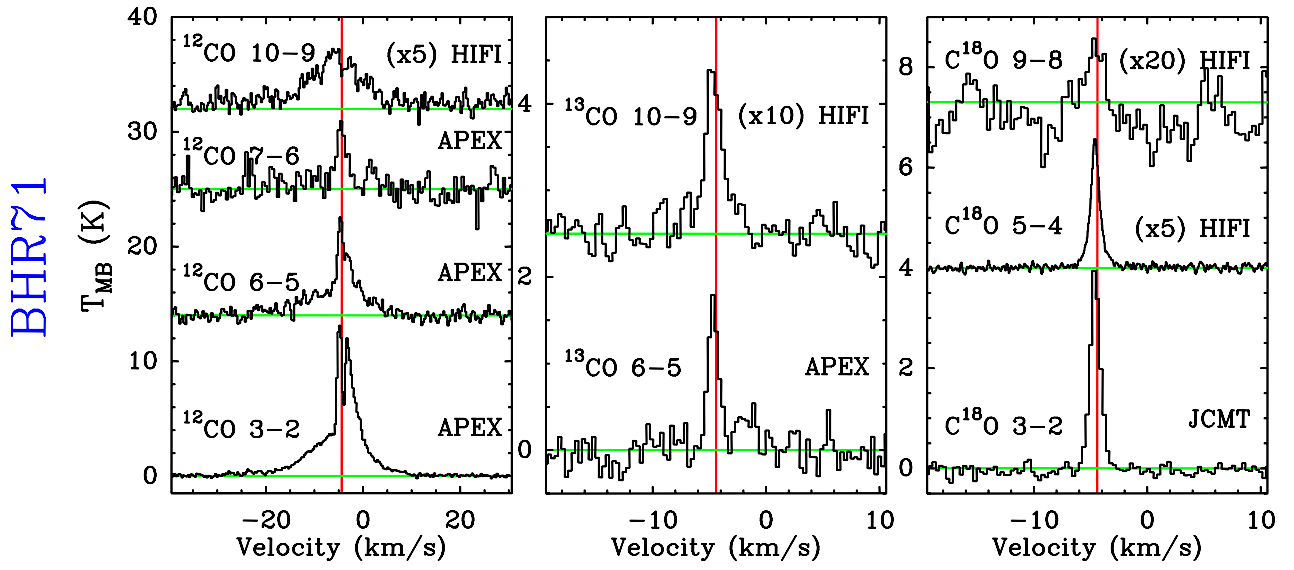
Fig. C.7. Observed ^{12}CO, ^{13}CO, and C^{18}O transitions for BHR71.

Table C.7. Observed line intensities for BHR71 in all observed transitions.

Mol.	Transition	Telescope	Efficiency η	$\int T_{MB}dV$ [K km s^{-1}]	T_{peak} [K]	rms [K]
CO	3–2	APEX	0.73	96.49	14.46	0.20
	6–5	APEX-CHAMP^{+}	0.46	49.14	8.72	0.52
	7–6	APEX-CHAMP^{+}	0.49	27.26	6.83	1.31
	10–9	*Herschel*-HIFI[a]	0.64	15.08	1.00	0.15
^{13}CO	6–5	APEX-CHAMP^{+}	0.45	2.67	1.92	0.23
	10–9	*Herschel*-HIFI[b]	0.74	0.40	0.20	0.017
C^{18}O	3–2	APEX-2a	0.73	4.12	4.05	0.11
	5–4	*Herschel*-HIFI[a]	0.76	0.56	0.51	0.010
	9–8	*Herschel*-HIFI[b]	0.74	0.08	0.07	0.022

Notes. [a] Only H-polarization observation is used. [b] H- and V-polarization observations averaged.

C.8. IRAS153981

Fig. C.8. Observed ^{12}CO, ^{13}CO, and C^{18}O transitions for IRAS15398.

Table C.8. Observed line intensities for IRAS15398 in all observed transitions.

Mol.	Transition	Telescope	Efficiency η	$\int T_{\rm MB}dV$ [K km s^{-1}]	$T_{\rm peak}$ [K]	rms [K]
CO	3–2	APEX	0.73	22.00	8.54	0.15
	4–3	APEX	0.60	26.26	6.76	0.32
	6–5	APEX-CHAMP$^+$	0.48	33.91	5.33	0.25
	7–6	APEX-CHAMP$^+$	0.49	16.88	3.90	0.64
	10–9	*Herschel*-HIFI[a]	0.64	17.74	3.01	0.10
^{13}CO	3–2	JCMT-HARPB	0.63	1.15	1.27	0.12
	6–5	APEX-CHAMP$^+$	0.48	0.51	0.51	0.12
	10–9	*Herschel*-HIFI[a]	0.74	0.20	0.18	0.027
C^{18}O	2–1	JCMT-RxA	0.69	2.03	2.52	0.093
	3–2	JCMT-HARPB	0.63	0.80	0.72	0.075
	5–4	*Herschel*-HIFI[a]	0.76	0.085	0.065	0.085
	9–8	*Herschel*-HIFI[a]	0.74	<0.055	. . .	0.024

Notes. [a] H- and V-polarization observations averaged.

C.9. L483 mm

Fig. C.9. Observed ^{12}CO, ^{13}CO, and C^{18}O transitions for L483 mm.

Table C.9. Observed line intensities for L483 mm in all observed transitions.

Mol.	Transition	Telescope	Efficiency η	$\int T_{MB}dV$ [K km s^{-1}]	T_{peak} [K]	rms [K]
CO	2–1	JCMT-RxA	0.69	22.40	6.53	0.13
	3–2	JCMT-HARPB	0.63	20.98	4.77	0.060
	4–3	JCMT	0.38	76.09	18.61	0.94
	6–5	APEX-CHAMP$^+$	0.45	32.40	8.92	0.49
	7–6	APEX-CHAMP$^+$	0.49	22.12	6.29	1.11
	10–9	*Herschel*-HIFI[a]	0.64	11.39	2.00	0.10
^{13}CO	2–1	JCMT-RxA	0.74	6.98	3.23	0.17
	3–2	JCMT-HARPB	0.63	4.28	2.94	0.071
	4–3	JCMT[b]	0.38	10.87	6.64	0.93
	6–5	APEX-CHAMP$^+$	0.46	4.17	2.16	0.13
	10–9	*Herschel*-HIFI[a]	0.74	0.20	0.10	0.017
C^{18}O	2–1	JCMT-RxA	0.69	3.52	3.10	0.042
	3–2	JCMT-HARPB	0.63	1.20	1.39	0.15
	5–4	*Herschel*-HIFI[c]	0.76	0.34	0.20	0.012
	9–8	*Herschel*-HIFI[a]	0.74	<0.050	. . .	0.022
	10–9	*Herschel*-HIFI[a]	0.74	<0.046	. . .	0.020

Notes. [a] H- and V-polarization observations averaged. [b] Taken in 11″ beam. [c] Only H-polarization observation is used.
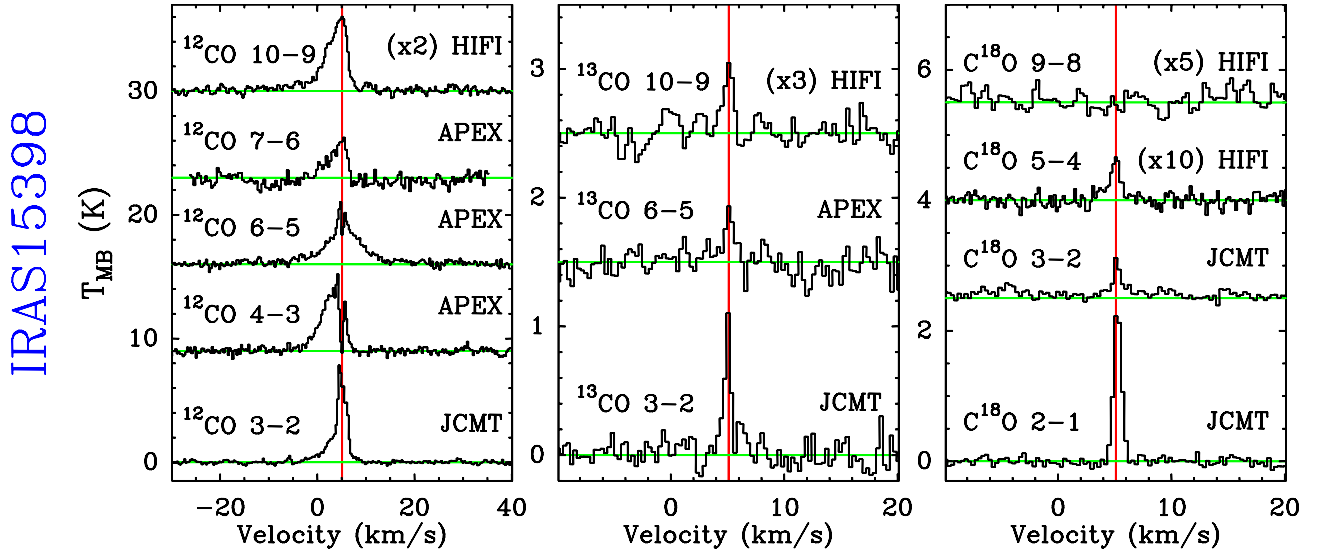
C.10. SMM1

Fig. C.10. Observed ^{12}CO, ^{13}CO, and C^{18}O transitions for SerSMM1.

Table C.10. Observed line intensities for SerSMM1 in all observed transitions.

Mol.	Transition	Telescope	Efficiency η	$\int T_{MB}dV$ [K km s^{-1}]	T_{peak} [K]	rms [K]
CO	2–1	JCMT-RxA	0.69	112.49	15.09	0.19
	3–2	JCMT-HARPB	0.63	101.82	13.45	0.023
	4–3	JCMT	0.38	159.90	29.03	0.39
	6–5	APEX-CHAMP$^+$	0.52	108.36	15.49	0.17
	7–6	APEX-CHAMP$^+$	0.40	105.61	16.41	0.59
	10–9	*Herschel*-HIFI[a]	0.64	82.28	7.74	0.09
^{13}CO	2–1	JCMT-RxA	0.74	31.78	8.87	0.17
	3–2	JCMT-HARPB	0.63	11.18	3.44	0.074
	6–5	APEX-CHAMP$^+$	0.46	17.53	5.58	0.18
	8–7	*Herschel*-HIFI[b]	0.75	5.93	1.49	0.007
	10–9	*Herschel*-HIFI[b]	0.74	3.44	0.66	0.027
C^{18}O	2–1	JCMT-RxA	0.69	10.31	5.49	0.06
	3–2	JCMT-HARPB	0.63	4.83	2.20	0.049
	5–4	*Herschel*-HIFI[b]	0.76	1.80	0.97	0.010
	6–5	APEX-CHAMP$^+$	0.56	4.75	2.10	0.26
	9–8	*Herschel*-HIFI[a]	0.74	0.44	0.18	0.019
	10–9	*Herschel*-HIFI[a]	0.74	0.59	0.12	0.017

Notes. [a] H- and V-polarization observations averaged. [b] Only H-polarization observation is used.
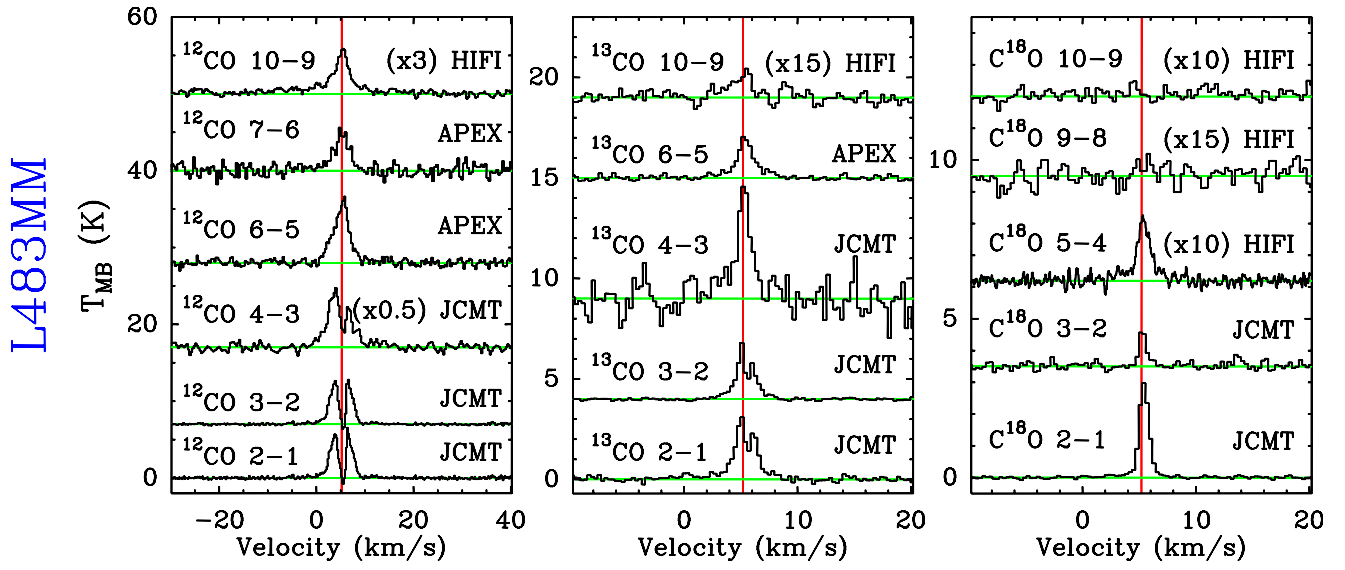
C.11. SMM4

Fig. C.11. Observed ^{12}CO, ^{13}CO, and C^{18}O transitions for SerSMM4.

Table C.11. Observed line intensities for SerSMM4 in all observed transitions.

Mol.	Transition	Telescope	Efficiency η	$\int T_{MB} dV$ [K km s^{-1}]	T_{peak} [K]	rms [K]
CO	2–1	JCMT-RxA	0.69	168.38	24.80	0.10
	3–2	JCMT-HARPB	0.63	108.35	15.48	0.022
	6–5	APEX-CHAMP$^+$	0.52	159.61	27.56	0.23
	7–6	APEX-CHAMP$^+$	0.40	110.08	19.39	0.63
	10–9	*Herschel*-HIFI[a]	0.64	40.24	4.98	0.13
^{13}CO	3–2	JCMT-HARPB	0.63	26.08	8.10	0.048
	6–5	APEX-CHAMP$^+$	0.52	10.65	2.61	0.15
	8–7	*Herschel*-HIFI[b]	0.75	1.62	0.31	0.009
	10–9	*Herschel*-HIFI[b]	0.74	0.52	0.10	0.020
C^{18}O	3–2	JCMT-HARPB	0.63	6.02	2.52	0.061
	5–4	*Herschel*-HIFI[b]	0.76	1.41	0.53	0.010
	9–8	*Herschel*-HIFI[b]	0.74	<0.055	. . .	0.024
	10–9	*Herschel*-HIFI[b]	0.74	<0.048	. . .	0.021

Notes. [a] Only H-polarization observation is used. [b] H- and V-polarization observations averaged.
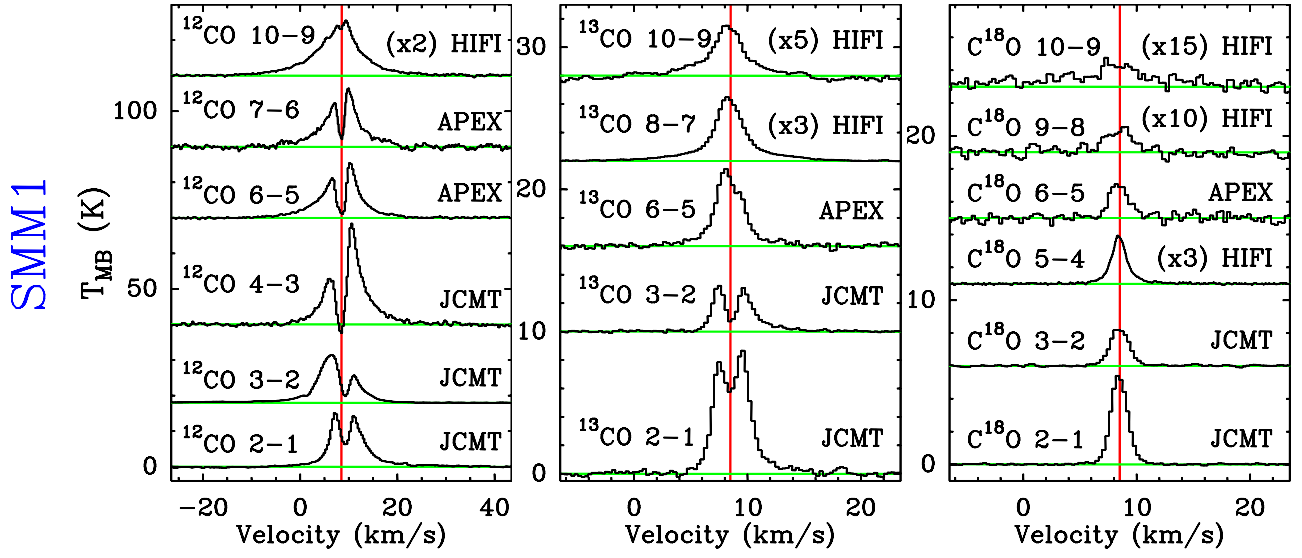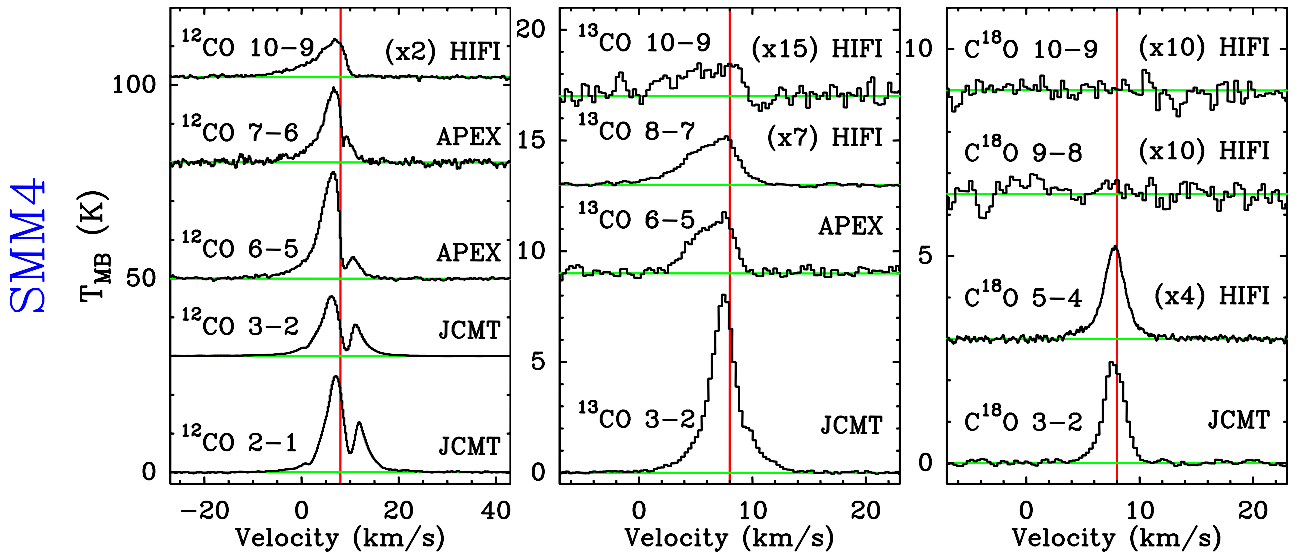
C.12. SMM3

Fig. C.12. Observed ^{12}CO, ^{13}CO, and C^{18}O transitions for SerSMM3.

Table C.12. Observed line intensities for SerSMM3 in all observed transitions.

Mol.	Transition	Telescope	Efficiency η	$\int T_{MB}dV$ [K km s^{-1}]	T_{peak} [K]	rms [K]
CO	2–1	JCMT-RxA	0.69	132.99	19.15	0.11
	3–2	JCMT-HARPB	0.63	78.14	10.83	0.034
	4–3	JCMT	0.38	242.95	32.85	0.79
	6–5	APEX-CHAMP$^+$	0.52	97.56	12.73	0.22
	7–6	APEX-CHAMP$^+$	0.40	74.26	11.54	0.55
	10–9	*Herschel*-HIFI[a]	0.64	35.71	3.49	0.095
^{13}CO	2–1	JCMT-RxA	0.74	44.50	13.65	0.18
	3–2	JCMT-HARPB	0.63	18.30	7.06	0.072
	6–5	APEX-CHAMP$^+$	0.52	9.59	4.12	0.26
	8–7	APEX-CHAMP$^+$	0.49	5.59	2.28	0.61
	10–9	*Herschel*-HIFI[a]	0.74	0.33	0.092	0.02
C^{18}O	2–1	JCMT-RxA	0.69	8.01	3.44	0.32
	3–2	JCMT-HARPB	0.63	4.95	2.63	0.060
	5–4	*Herschel*-HIFI[b]	0.76	1.29	0.70	0.012
	9–8	*Herschel*-HIFI[a]	0.74	<0.043	. . .	0.019
	10–9	*Herschel*-HIFI[a]	0.74	<0.032	. . .	0.014

Notes. [a] H- and V-polarization observations averaged. [b] Only H-polarization observation is used.

C.13. L723 mm

Fig. C.13. Observed ^{12}CO, ^{13}CO, and C^{18}O transitions for L723 mm.

Table C.13. Observed line intensities for L723 mm in all observed transitions.

Mol.	Transition	Telescope	Efficiency η	$\int T_{MB} dV$ [K km s^{-1}]	T_{peak} [K]	rms [K]
CO	3–2	JCMT-HARPB	0.63	39.54	6.39	0.052
	6–5	APEX-CHAMP$^+$	0.52	22.02	5.44	1.11
	7–6	APEX-CHAMP$^+$	0.49	11.00	6.00	3.81
	10–9	*Herschel*-HIFI[a]	0.64	6.65	1.17	0.085
^{13}CO	2–1	JCMT-RxA	0.74	7.09	2.23	0.10
	3–2	JCMT-HARPB	0.63	4.79	2.18	0.08
	4–3	JCMT[b]	0.38	10.81	5.92	0.76
	6–5	APEX-CHAMP$^+$	0.45	3.33	1.25	0.18
	8–7	APEX-CHAMP$^+$	0.49	1.94	4.67	1.55
	10–9	*Herschel*-HIFI[a]	0.74	0.21	0.13	0.025
C^{18}O	2–1	JCMT-RxA	0.69	2.16	1.75	0.077
	3–2	JCMT-HARPB	0.63	0.96	0.70	0.094
	5–4	*Herschel*-HIFI[c]	0.76	0.20	0.14	0.019
	9–8	*Herschel*-HIFI[a]	0.74	<0.043	. . .	0.019

Notes. [a] H- and V-polarization observations averaged. [b] Taken in 11″ beam. [c] Only H-polarization observation is used.
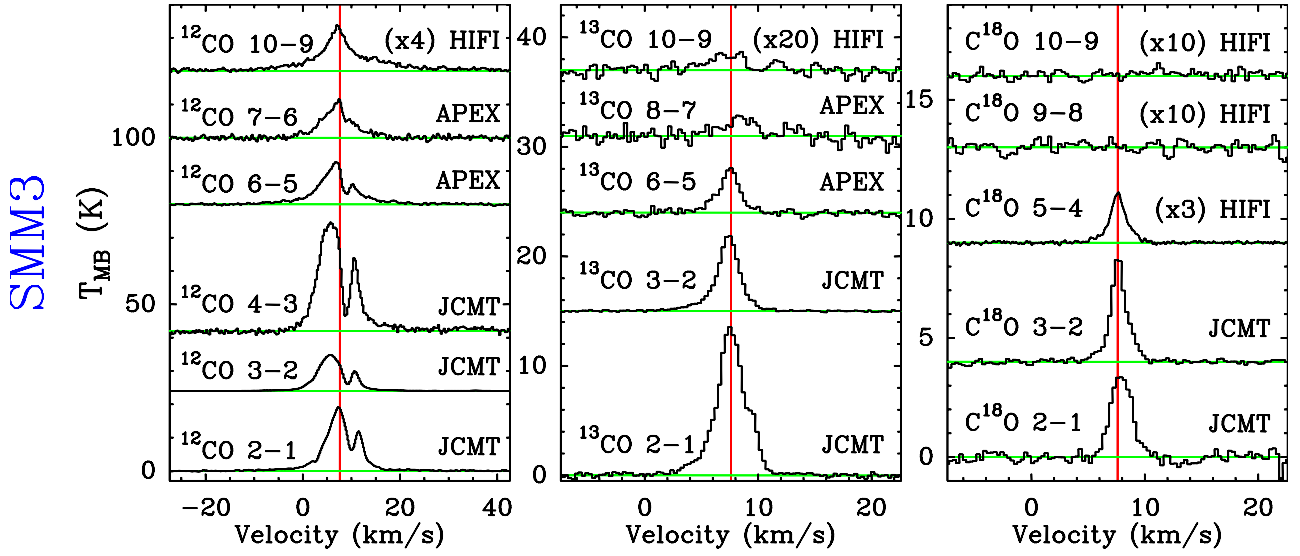
C.14. B335

Fig. C.14. Observed ^{12}CO, ^{13}CO, and C^{18}O transitions for B335.

Table C.14. Observed line intensities for B335 in all observed transitions.

Mol.	Transition	Telescope	Efficiency η	$\int T_{MB}dV$ [K km s^{-1}]	T_{peak} [K]	rms [K]
CO	2–1	JCMT-RxA	0.69	56.15	13.63	0.51
	3–2	JCMT-HARPB	0.63	38.33	8.69	1.49
	4–3	JCMT	0.38	68.67	13.41	0.15
	6–5	APEX-CHAMP$^+$	0.52	25.89	4.41	0.23
	7–6	APEX-CHAMP$^+$	0.49	21.88	3.61	0.58
	10–9	*Herschel*-HIFI[a]	0.64	12.49	1.50	0.13
^{13}CO	2–1	JCMT-RxA	0.74	4.27	3.23	0.051
	3–2	JCMT-HARPB	0.63	3.40	2.95	0.070
	6–5	APEX-CHAMP$^+$	0.48	2.56	2.13	0.21
	10–9	*Herschel*-HIFI[b]	0.74	0.19	0.08	0.019
C^{18}O	2–1	JCMT-RxA	0.69	2.40	2.54	0.10
	3–2	JCMT-HARPB	0.63	1.39	1.90	0.062
	5–4	*Herschel*-HIFI[a]	0.76	0.29	0.32	0.012
	9–8	*Herschel*-HIFI[b]	0.74	<0.057	...	0.025

Notes. [a] Only H-polarization observation is used. [b] H- and V-polarization observations averaged.
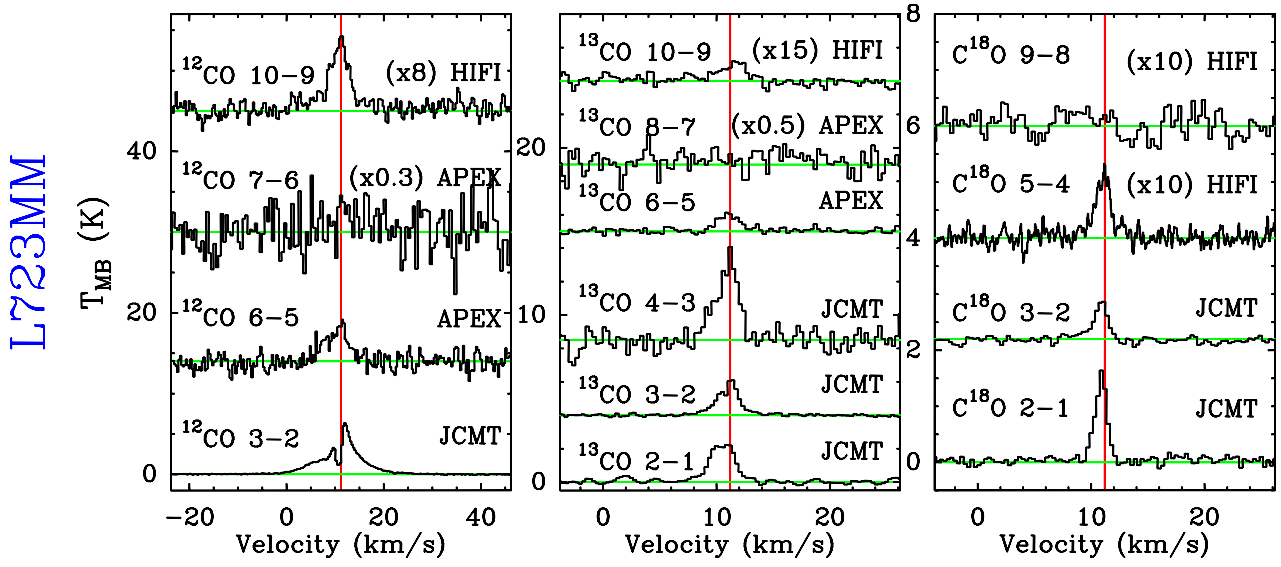
C.15. L1157

Fig. C.15. Observed ^{12}CO, ^{13}CO, and C^{18}O transitions for L1157.

Table C.15. Observed line intensities for L1157 in all observed transitions.

Mol.	Transition	Telescope	Efficiency η	$\int T_{MB} dV$ [K km s^{-1}]	T_{peak} [K]	rms [K]
CO	2–1	JCMT-RxA	0.69	47.92	8.77	0.28
	3–2	JCMT-HARPB	0.63	48.22	7.41	0.10
	4–3	JCMT	0.38	78.15	10.67	0.88
	10–9	*Herschel*-HIFI[a]	0.64	8.94	0.85	0.15
^{13}CO	2–1	JCMT-RxA	0.74	5.10	4.34	0.10
	3–2	JCMT-HARPB	0.63	3.11	2.57	0.11
	10–9	*Herschel*-HIFI[b]	0.74	0.33	0.10	0.027
C^{18}O	2–1	JCMT-RxA	0.69	1.46	1.50	0.094
	3–2	JCMT-HARPB	0.63	0.58	0.83	0.090
	5–4	*Herschel*-HIFI[b]	0.76	0.11	0.14	0.014
	9–8	*Herschel*-HIFI[a]	0.74	<0.05	. . .	0.022

Notes. [a] H- and V-polarization observations averaged. [b] Only H-polarization observation is used.
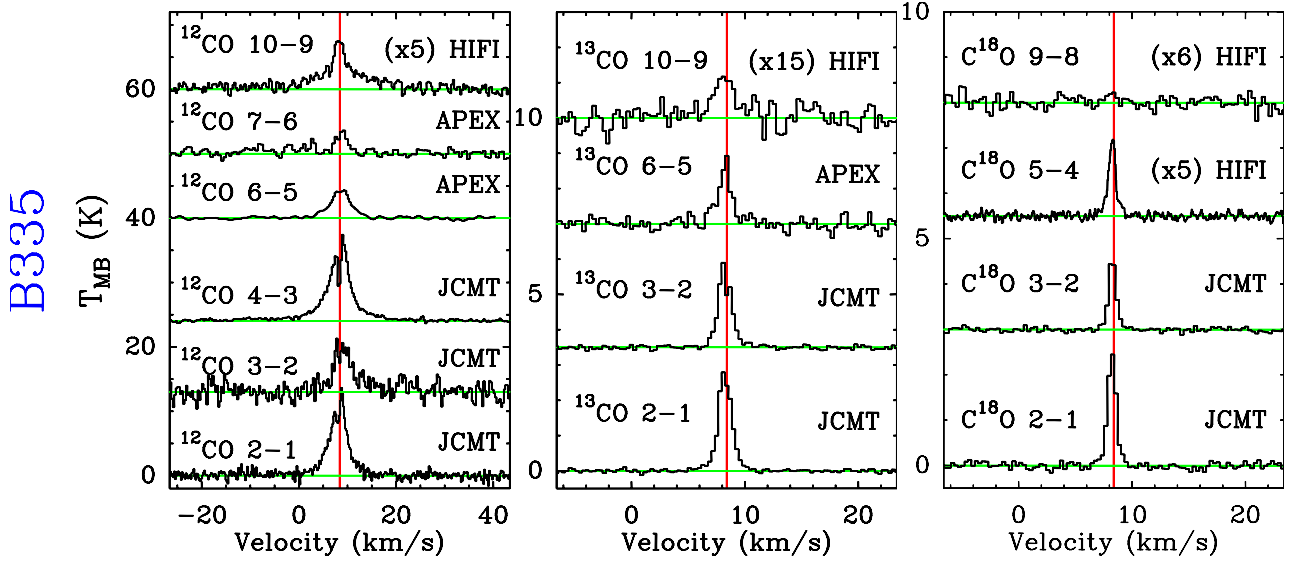
C.16. L1489

Fig. C.16. Observed ^{12}CO, ^{13}CO, and C^{18}O transitions for L1489.

Table C.16. Observed line intensities for L1489 in all observed transitions.

Mol.	Transition	Telescope	Efficiency η	$\int T_{MB} dV$ [K km s^{-1}]	T_{peak} [K]	rms [K]
CO	2–1	JCMT-RxA	0.69	19.87	4.49	0.15
	3–2	JCMT-HARPB	0.63	13.04	4.00	0.49
	4–3	JCMT	0.38	33.80	7.14	0.15
	6–5	APEX-CHAMP$^+$	0.45	20.87	6.48	0.16
	7–6	APEX-CHAMP$^+$	0.49	9.06	3.65	0.37
	10–9	*Herschel*-HIFI[a]	0.64	6.20	1.16	0.11
^{13}CO	3–2	JCMT-HARPB	0.63	4.45	2.70	0.082
	6–5	APEX-CHAMP$^+$	0.45	8.22	3.77	1.29
	10–9	*Herschel*-HIFI[a]	0.74	0.28	0.11	0.029
C^{18}O	2–1	JCMT-RxA	0.69	1.72	1.62	0.071
	3–2	JCMT-HARPB	0.63	0.67	0.44	0.10
	9–8	*Herschel*-HIFI[a]	0.74	<0.055	...	0.024

Notes. [a] H- and V-polarization observations averaged.

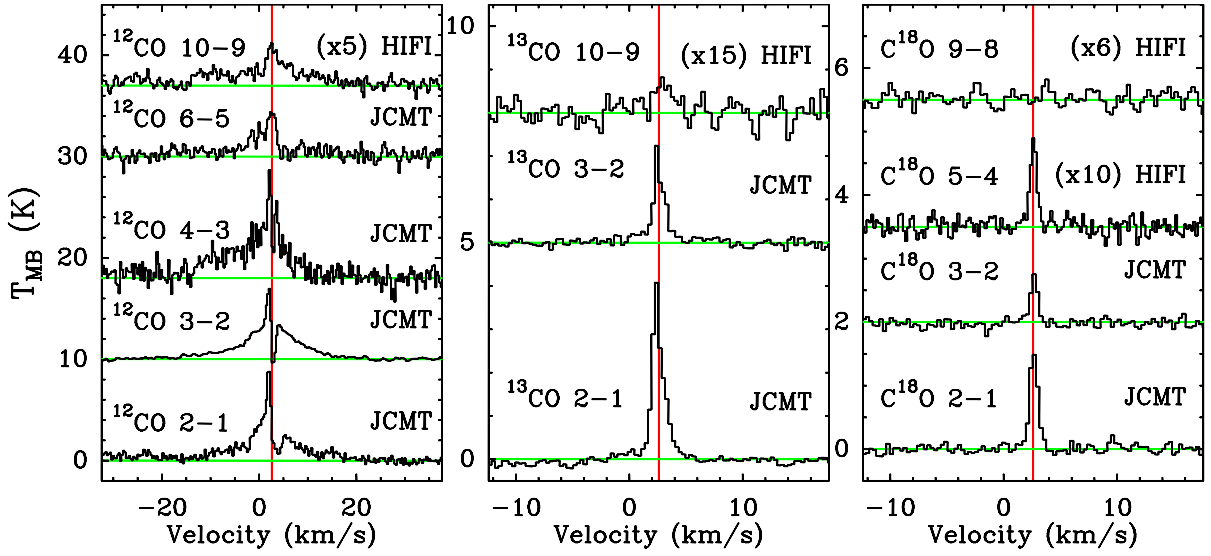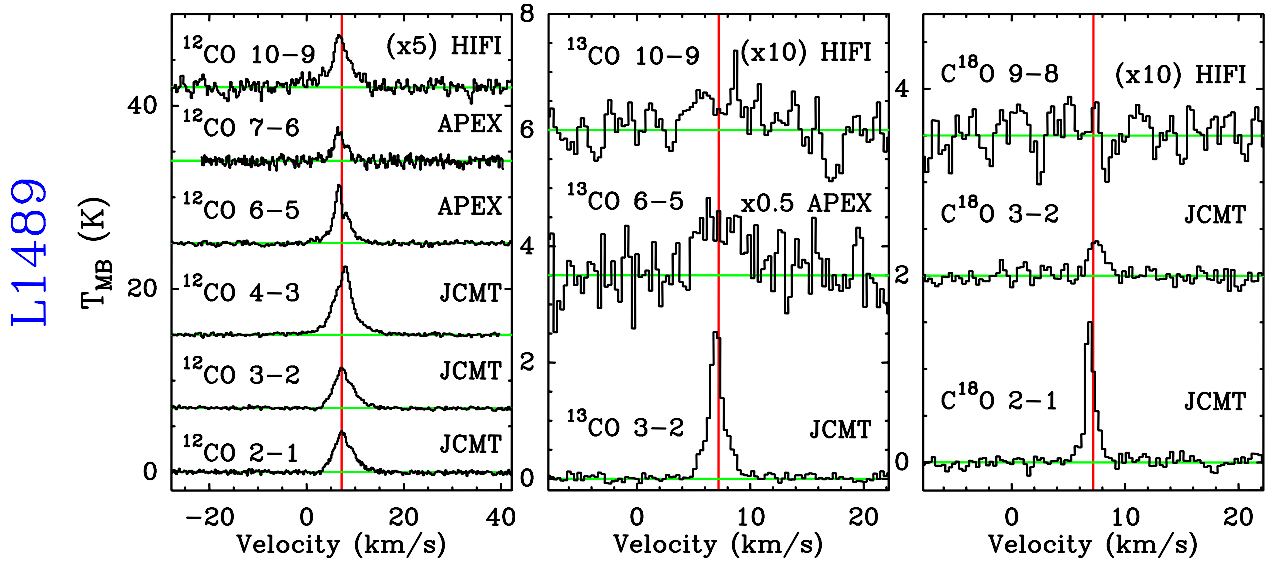## C.17. L1551IRS5

Fig. C.17. Observed ^{12}CO, ^{13}CO, and $C^{18}O$ transitions for L1551IRS5.

Table C.17. Observed line intensities for L1551IRS5 in all observed transitions.

Mol.	Transition	Telescope	Efficiency η	$\int T_{MB}dV$ [K km s^{-1}]	T_{peak} [K]	rms [K]
CO	2–1	JCMT-RxA	0.69	71.52	9.82	0.27
	3–2	JCMT-HARPB	0.63	37.52	6.68	0.11
	4–3	JCMT[a]	0.38	108.13	16.69	0.45
	10–9	*Herschel*-HIFI[b]	0.64	14.73	3.59	0.13
^{13}CO	2–1	JCMT-RxA	0.74	17.86	7.04	0.25
	3–2	JCMT-HARPB	0.63	10.23	4.82	0.18
	6–5	APEX-CHAMP$^+$	0.48	10.50	7.47	0.24
	10–9	*Herschel*-HIFI[b]	0.74	1.38	0.49	0.028
$C^{18}O$	2–1	JCMT-RxA	0.69	5.26	4.62	0.076
	3–2	JCMT-HARPB	0.63	2.29	2.58	0.18
	9–8	*Herschel*-HIFI	0.74	0.22	0.12	0.025

Notes. [a] Taken in 11″ beam. [b] H- and V-polarization observations averaged.
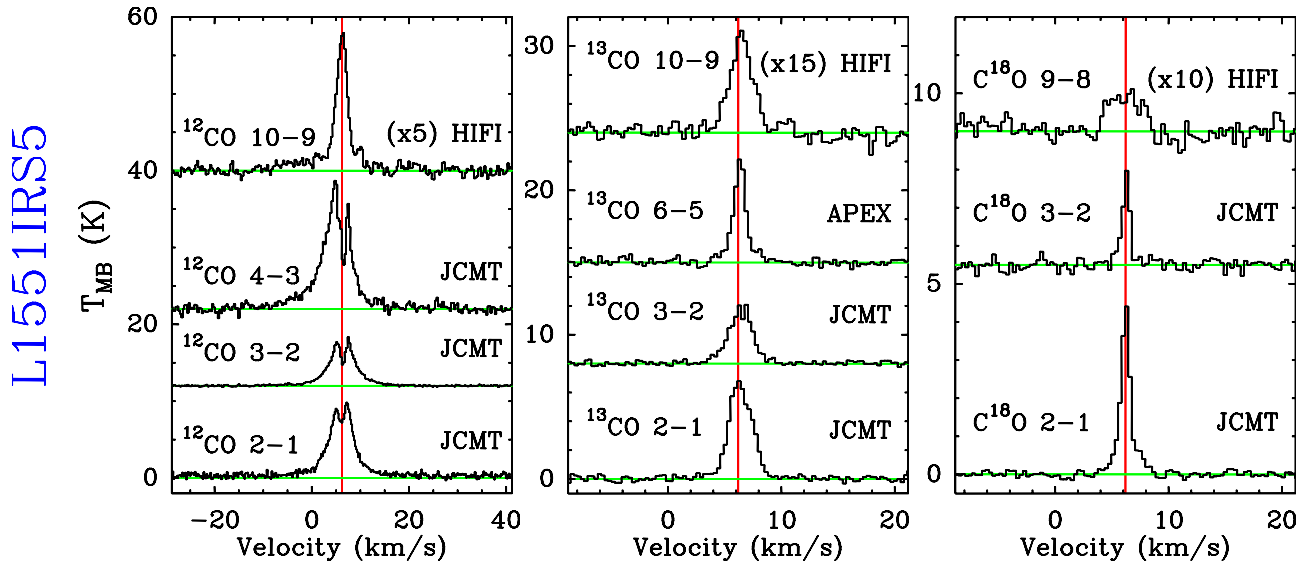
C.18. TMR1

Fig. C.18. Observed ^{12}CO, ^{13}CO, and C^{18}O transitions for TMR1.

Table C.18. Observed line intensities for TMR1 in all observed transitions.

Mol.	Transition	Telescope	Efficiency η	$\int T_{MB}dV$ [K km s^{-1}]	T_{peak} [K]	rms [K]
CO	2–1	JCMT-RxA	0.69	11.94	5.95	0.41
	3–2	JCMT-HARPB	0.63	8.55	4.61	0.088
	4–3	JCMT[a]	0.38	40.78	15.23	3.26
	6–5	APEX-CHAMP$^+$	0.45	22.65	9.15	0.32
	7–6	APEX-CHAMP$^+$	0.42	21.89	8.92	0.81
	10–9	*Herschel*-HIFI[b]	0.64	9.18	2.19	0.13
^{13}CO	3–2	JCMT-HARPB	0.63	4.27	4.62	0.057
	6–5	APEX-CHAMP$^+$	0.45	4.79	2.00	0.032
	10–9	*Herschel*-HIFI[b]	0.74	0.49	0.11	0.027
C^{18}O	2–1	JCMTRxA	0.69	2.20	1.61	0.11
	3–2	JCMT-HARPB	0.63	1.13	1.22	0.091
	9–8	*Herschel*-HIFI[b]	0.74	<0.052	. . .	0.023

Notes. [a] Taken in 11″ beam. [b] H- and V-polarization observations averaged.
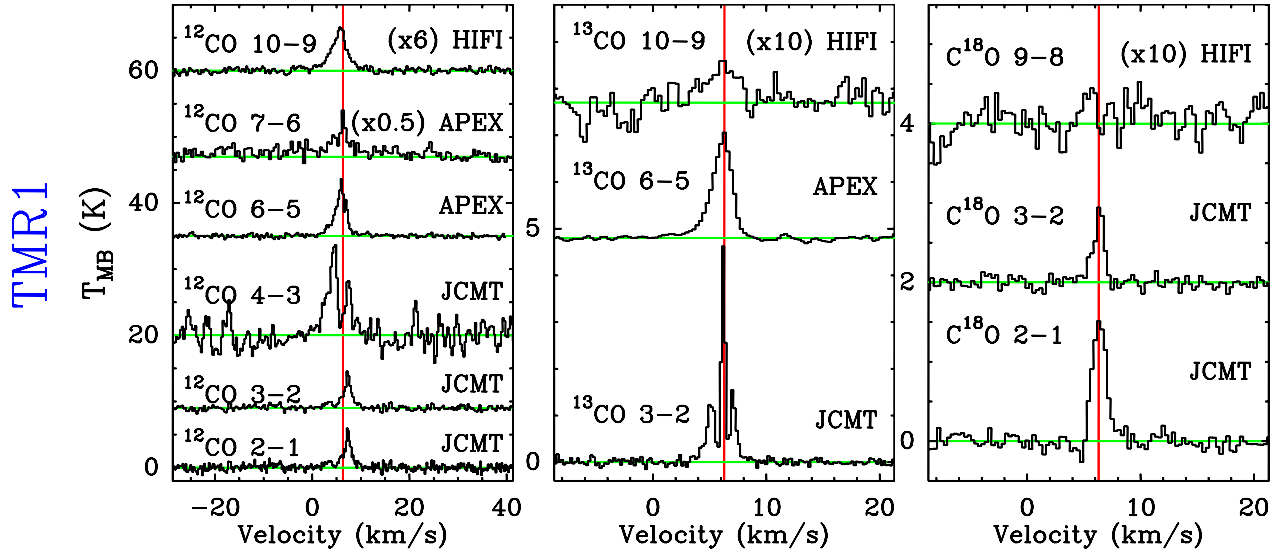
C.19. TMC1A

Fig. C.19. Observed ^{12}CO, ^{13}CO, and $C^{18}O$ transitions for TMC1A.

Table C.19. Observed line intensities for TMC1A in all observed transitions.

Mol.	Transition	Telescope	Efficiency η	$\int T_{MB}dV$ [K km s^{-1}]	T_{peak} [K]	rms [K]
CO	2–1	JCMT-RxA	0.69	30.32	5.55	0.19
	3–2	JCMT-HARPB	0.63	19.10	2.10	0.089
	4–3	JCMT[a]	0.38	42.46	4.82	0.46
	6–5	APEX-CHAMP$^+$	0.52	11.68	3.21	0.24
	7–6	APEX-CHAMP$^+$	0.49	4.13	2.07	0.81
	10–9	*Herschel*-HIFI[b]	0.64	1.37	0.52	0.13
^{13}CO	3–2	JCMT-HARPB	0.63	2.18	1.43	0.073
	6–5	APEX-CHAMP$^+$	0.48	1.76	1.09	0.25
	10–9	*Herschel*-HIFI[b]	0.74	<0.10	…	0.031
$C^{18}O$	2–1	IRAM 30m	0.59	1.97	2.40	0.33
	3–2	JCMT-HARPB	0.63	0.62	0.61	0.11
	9–8	*Herschel*-HIFI[c]	0.74	<0.052	…	0.023

Notes. [a] Taken in 11″ beam. [b] Only H-polarization observation is used. [c] H- and V-polarization observations averaged.
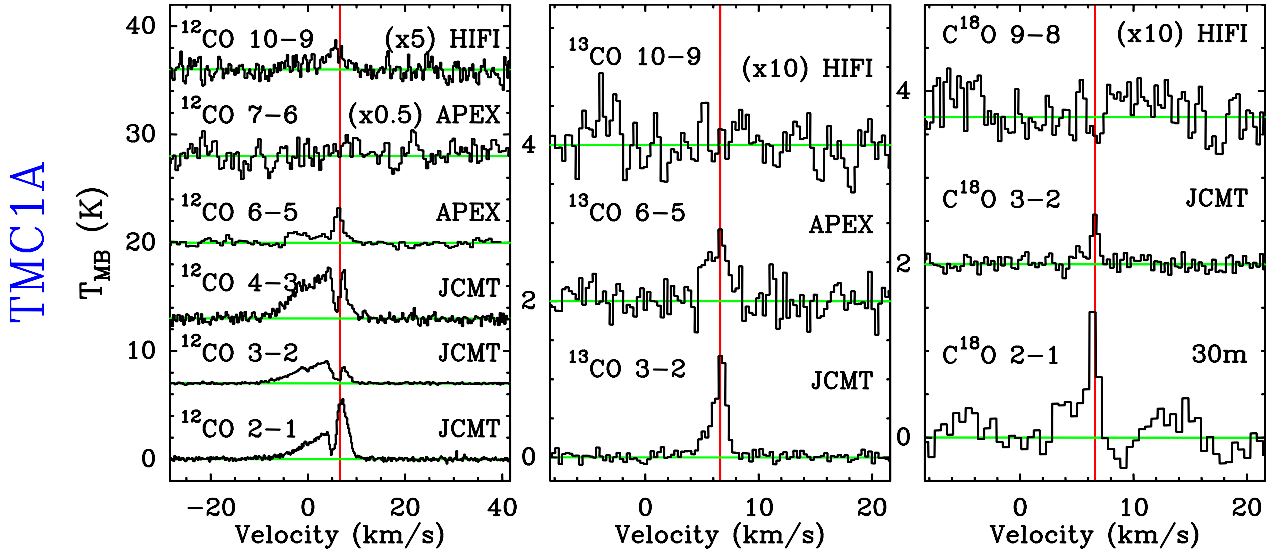
C.20. TMC1

Fig. C.20. Observed ^{12}CO, ^{13}CO, and C^{18}O transitions for TMC1.

Table C.20. Observed line intensities for TMC1 in all observed transitions.

Mol.	Transition	Telescope	Efficiency η	$\int T_{\mathrm{MB}}dV$ [K km s^{-1}]	T_{peak} [K]	rms [K]
CO	2–1	JCMT-RxA	0.69	9.06	1.56	0.21
	3–2	JCMT-HARPB	0.63	9.77	2.05	0.10
	4–3	JCMT[a]	0.38	22.55	4.69	0.44
	6–5	APEX-CHAMP$^+$	0.52	26.58	5.98	0.36
	7–6	APEX-CHAMP$^+$	0.49	11.09	4.53	0.92
	10–9	*Herschel*-HIFI[b]	0.64	2.87	0.49	0.15
^{13}CO	3–2	JCMT-HARPB	0.63	1.16	1.09	0.091
	6–5	APEX-CHAMP$^+$	0.48	2.38	1.81	0.24
	10–9	*Herschel*-HIFI[c]	0.74	<0.10	. . .	0.033
C^{18}O	2–1	IRAM 30m	0.59	4.17	4.10	0.41
	3–2	JCMT-HARPB	0.63	0.94	1.35	0.12
	9–8	*Herschel*-HIFI[c]	0.74	<0.048	. . .	0.021

Notes. [a] Taken in 11″ beam. [b] Only H-polarization observation is used. [c] H- and V-polarization observations averaged.
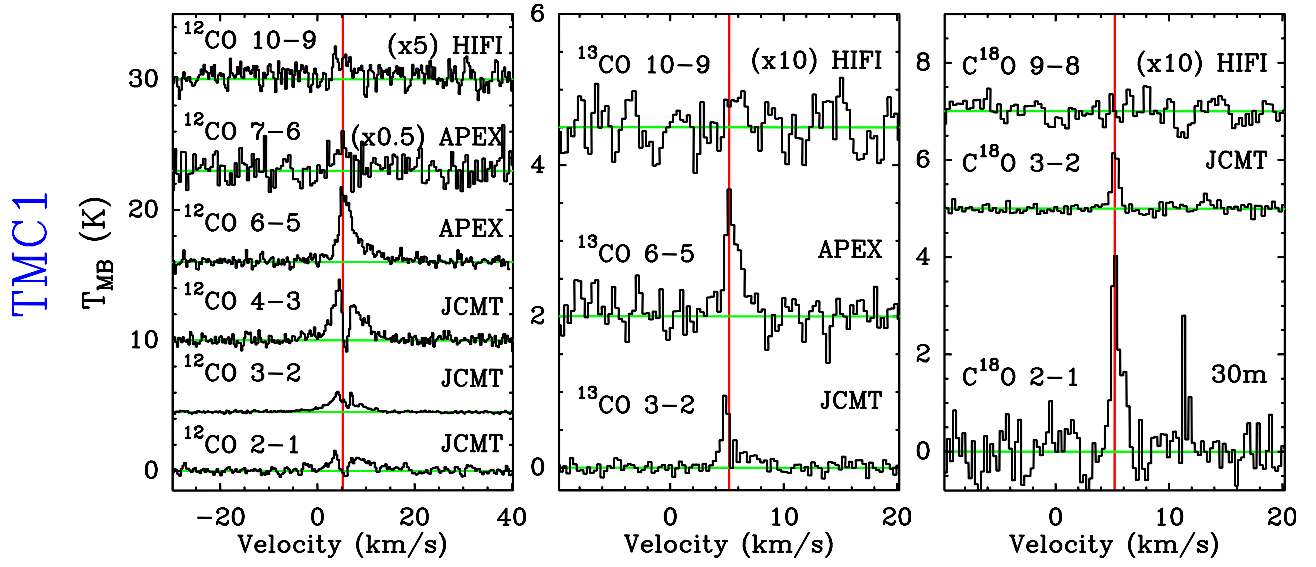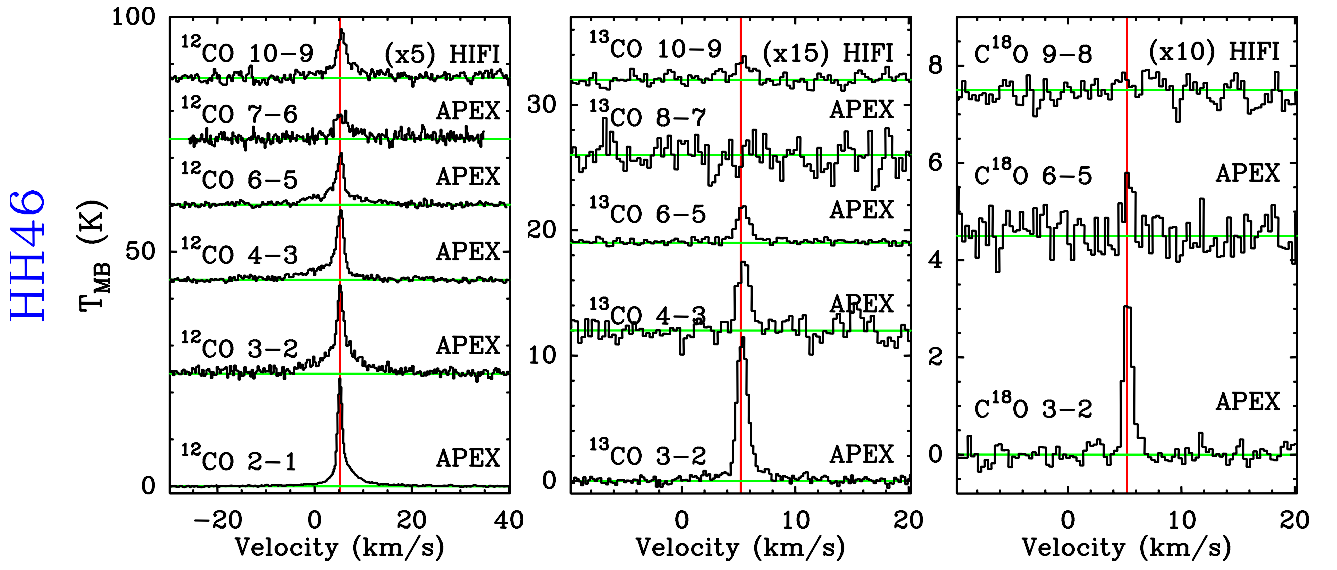
C.21. HH46

Fig. C.21. Observed ^{12}CO, ^{13}CO, and C^{18}O transitions for HH46.

Table C.21. Observed line intensities for HH46 in all observed transitions.

Mol.	Transition	Telescope	Efficiency η	$\int T_{MB}dV$ [K km s^{-1}]	T_{peak} [K]	rms [K]
CO	2–1	APEX	0.73	53.56	22.98	0.08
	3–2	APEX	0.73	81.87	18.78	0.72
	4–3	APEX	0.70	42.81	14.61	0.49
	6–5	APEX-CHAMP$^+$	0.45	45.15	11.84	0.47
	7–6	APEX-CHAMP$^+$	0.49	22.85	6.05	0.89
	10–9	*Herschel*-HIFI[a]	0.64	8.21	2.12	0.14
^{13}CO	3–2	APEX	0.73	17.52	11.89	0.32
	4–3	APEX[b]	0.70	8.04	6.00	1.08
	6–5	APEX-CHAMP$^+$	0.45	5.94	3.12	0.23
	8–7	APEX-CHAMP$^+$	0.42	<1.07	. . .	0.39
	10–9	*Herschel*-HIFI[a]	0.74	0.25	0.18	0.041
C^{18}O	3–2	APEX–2a	0.70	3.20	. . .	0.10
	6–5	APEX-CHAMP$^+$	0.56	1.27	1.50	0.50
	9–8	*Herschel*-HIFI[c]	0.74	<0.057	. . .	0.025

Notes. [a] Only H-polarization observation is used. [b] Taken in 11″ beam. [c] H- and V-polarization observations averaged.
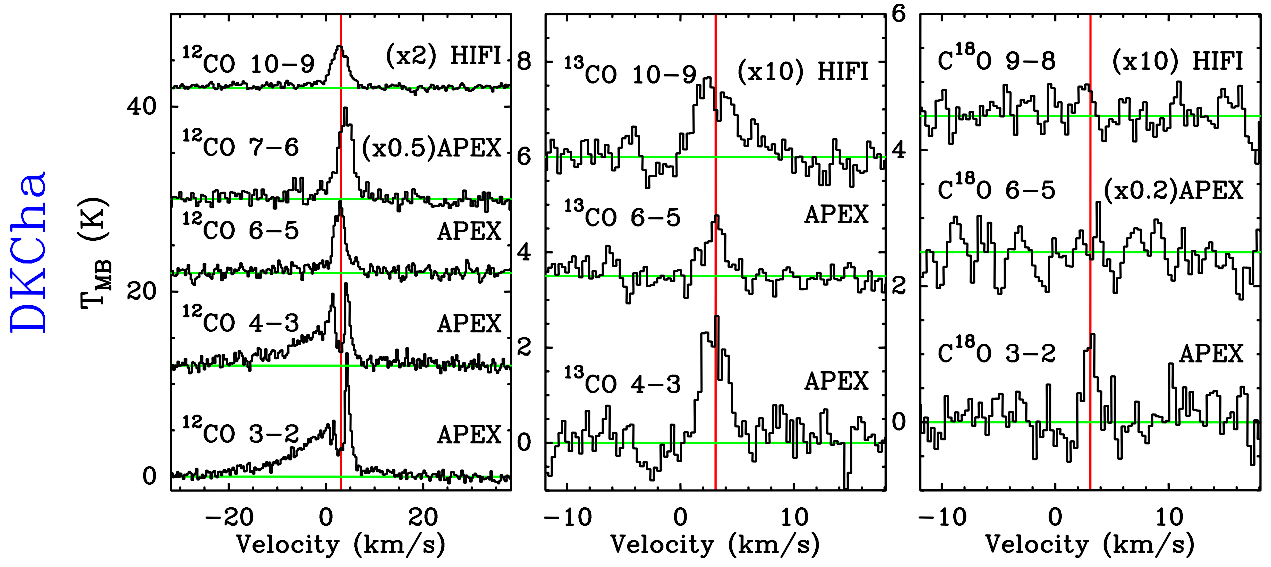
C.22. DK Cha

Fig. C.22. Observed ^{12}CO, ^{13}CO, and C^{18}O transitions for DK Cha.

Table C.22. Observed line intensities for DK Cha in all observed transitions.

Mol.	Transition	Telescope	Efficiency η	$\int T_{MB}dV$ [K km s^{-1}]	T_{peak} [K]	rms [K]
CO	3–2	APEX	0.73	79.98	13.35	0.38
	4–3	APEX	0.65	71.77	10.22	0.49
	6–5	APEX-CHAMP$^+$	0.45	28.02	8.21	0.57
	7–6	APEX-CHAMP$^+$	0.42	84.86	20.21	1.89
	10–9	*Herschel*-HIFI[a]	0.64	11.40	2.31	0.12
^{13}CO	3–2	APEX[b]	. . .	6.70	. . .	. . .
	4–3	APEX	0.65	6.54	3.06	0.44
	6–5	APEX-CHAMP$^+$	0.45	2.19	1.37	0.25
	8–7	APEX-CHAMP$^+$	0.49	0.84	. . .	0.90
	10–9	*Herschel*-HIFI[c]	0.74	0.82	0.19	0.028
C^{18}O	3–2	APEX	0.70	1.41	1.55	0.40
	9–8	*Herschel*-HIFI[a]	0.74	<0.057	. . .	0.025

Notes. [a] H- and V-polarization observations averaged. [b] van Kempen et al. (2006) [c] Only H-polarization observation is used.
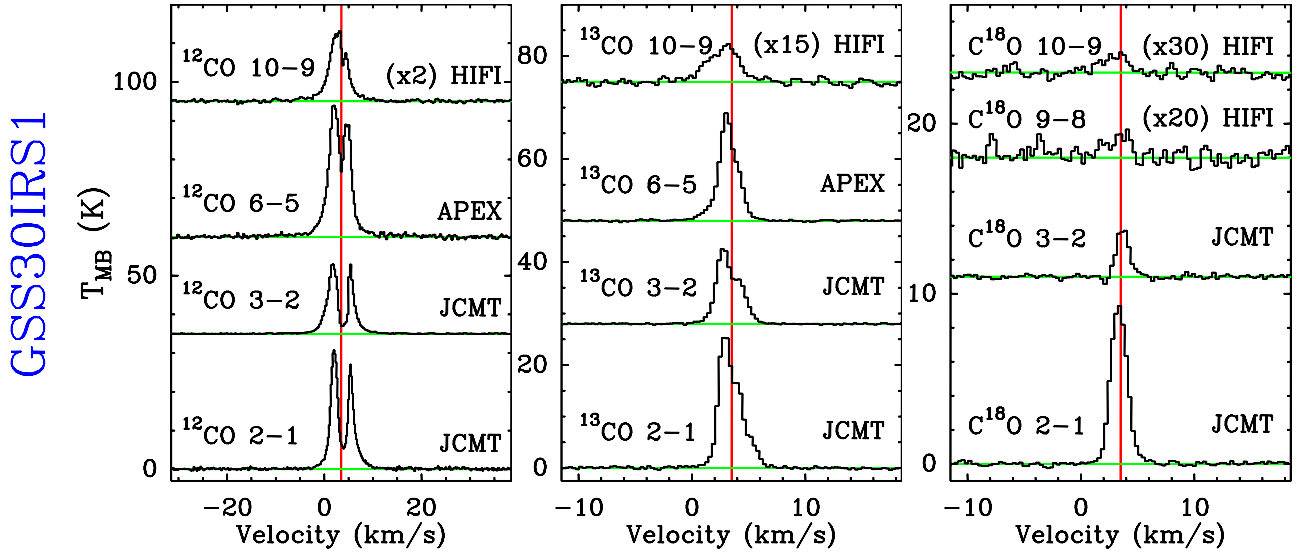
C.23. GSS30IRS1

Fig. C.23. Observed ^{12}CO, ^{13}CO, and C^{18}O transitions for GSS30IRS1.

Table C.23. Observed line intensities for GSS30IRS1 in all observed transitions.

Mol.	Transition	Telescope	Efficiency η	$\int T_{\rm MB}{\rm d}V$ [K km s^{-1}]	$T_{\rm peak}$ [K]	rms [K]
CO	2–1	JCMT-RxA	0.69	114.80	30.76	0.23
	3–2	JCMT-HARPB	0.63	77.95	18.90	0.079
	6–5	APEX-CHAMP$^+$	0.45	172.38	34.48	0.41
	10–9	*Herschel*-HIFI[a]	0.64	41.78	9.28	0.15
^{13}CO	2–1	JCMT-RxA	0.74	58.94	26.30	0.25
	3–2	JCMT-HARPB	0.63	34.33	14.87	0.12
	6–5	APEX-CHAMP$^+$	0.48	41.64	21.37	0.13
	10–9	*Herschel*-HIFI[a]	0.74	2.06	0.50	0.032
C^{18}O	2–1	JCMT-RxA	0.69	17.09	9.45	0.12
	3–2	JCMT-HARPB	0.63	3.73	2.81	0.12
	9–8	*Herschel*-HIFI[b]	0.74	0.21	0.093	0.023
	10–9	*Herschel*-HIFI[b]	0.74	0.089	0.042	0.009

Notes. [a] Only H-polarization observation is used. [b] H- and V-polarization observations averaged.
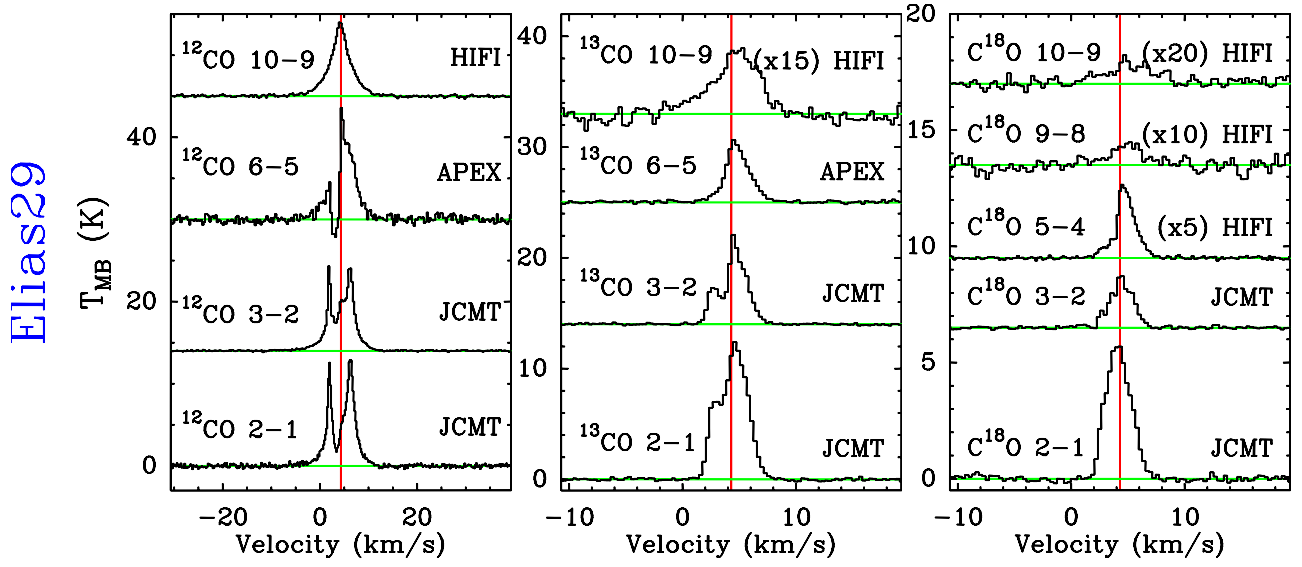
C.24. Elias29

Fig. C.24. Observed ^{12}CO, ^{13}CO, and C^{18}O transitions for Elias29.

Table C.24. Observed line intensities for Elias29 in all observed transitions.

Mol.	Transition	Telescope	Efficiency η	$\int T_{MB} dV$ [K km s^{-1}]	T_{peak} [K]	rms [K]
CO	2–1	JCMT-RxA	0.69	53.74	12.88	0.18
	3–2	JCMT-HARPB	0.63	48.35	11.14	0.069
	6–5	APEX-CHAMP$^+$	0.48	45.08	14.55	0.48
	10–9	*Herschel*-HIFI[a]	0.64	45.86	9.15	0.11
^{13}CO	2–1	JCMT-RxA	0.74	37.38	12.55	0.17
	3–2	JCMT-HARPB	0.63	18.71	8.25	0.10
	6–5	APEX-CHAMP$^+$	0.48	14.62	5.68	0.13
	10–9	*Herschel*-HIFI[a]	0.74	1.72	0.39	0.031
C^{18}O	2–1	JCMT-RxA	0.69	15.69	5.89	0.15
	3–2	JCMT-HARPB	0.63	5.27	2.53	0.066
	5–4	*Herschel*-HIFI[a]	0.76	1.26	0.60	0.010
	9–8	*Herschel*-HIFI[a]	0.74	0.34	0.10	0.027
	10–9	*Herschel*-HIFI[b]	0.74	0.23	0.07	0.010

Notes. [a] H- and V-polarization observations averaged. [b] Only H-polarization observation is used.
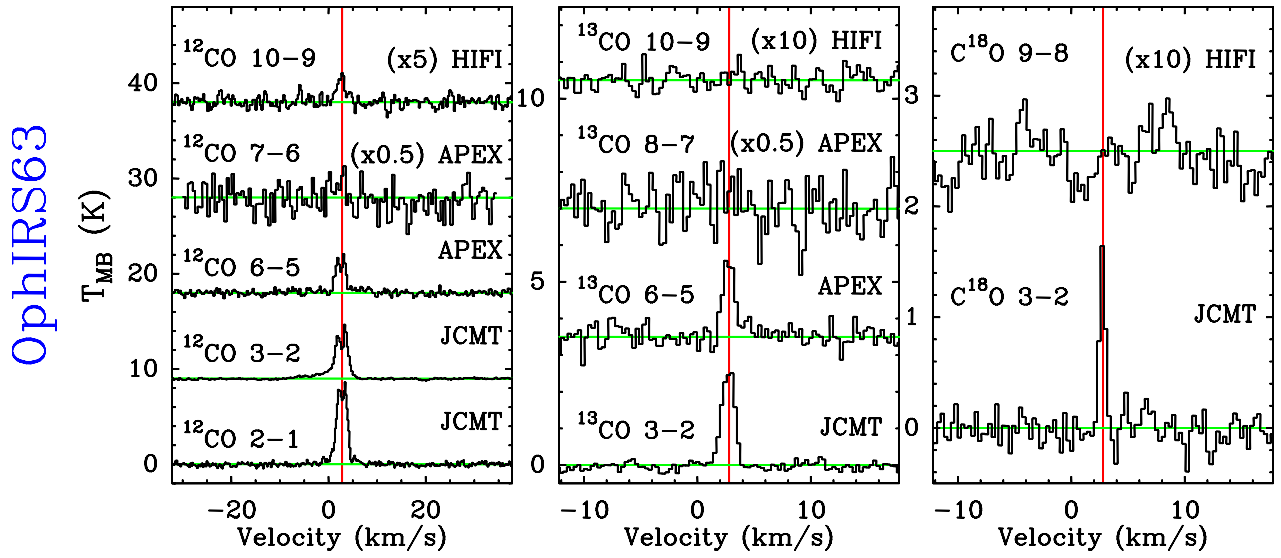
C.25. Oph IRS63

Fig. C.25. Observed ^{12}CO, ^{13}CO, and C^{18}O transitions for Oph IRS63.

Table C.25. Observed line intensities for OphIRS63 in all observed transitions.

Mol.	Transition	Telescope	Efficiency η	$\int T_{MB}dV$ [K km s^{-1}]	T_{peak} [K]	rms [K]
CO	2–1	JCMT-RxA	0.69	23.27	8.64	0.19
	3–2	JCMT-HARPB	0.63	16.47	6.06	0.094
	6–5	APEX-CHAMP$^+$	0.48	11.11	4.36	0.32
	7–6	APEX-CHAMP$^+$	0.48	8.63	4.77	1.09
	10–9	*Herschel*-HIFI[a]	0.64	1.15	0.62	0.13
^{13}CO	3–2	JCMT-HARPB	0.63	3.58	2.67	0.13
	6–5	APEX-CHAMP$^+$	0.45	3.02	2.51	0.35
	8–7	APEX-CHAMP$^+$	0.49	<4.26	...	1.68
	10–9	*Herschel*-HIFI[a]	0.74	<0.066	...	0.026
C^{18}O	3–2	JCMT-HARPB	0.63	0.94	1.73	0.17
	9–8	*Herschel*-HIFI[a]	0.74	<0.048	...	0.021

Notes. [a] H- and V-polarization observations averaged.
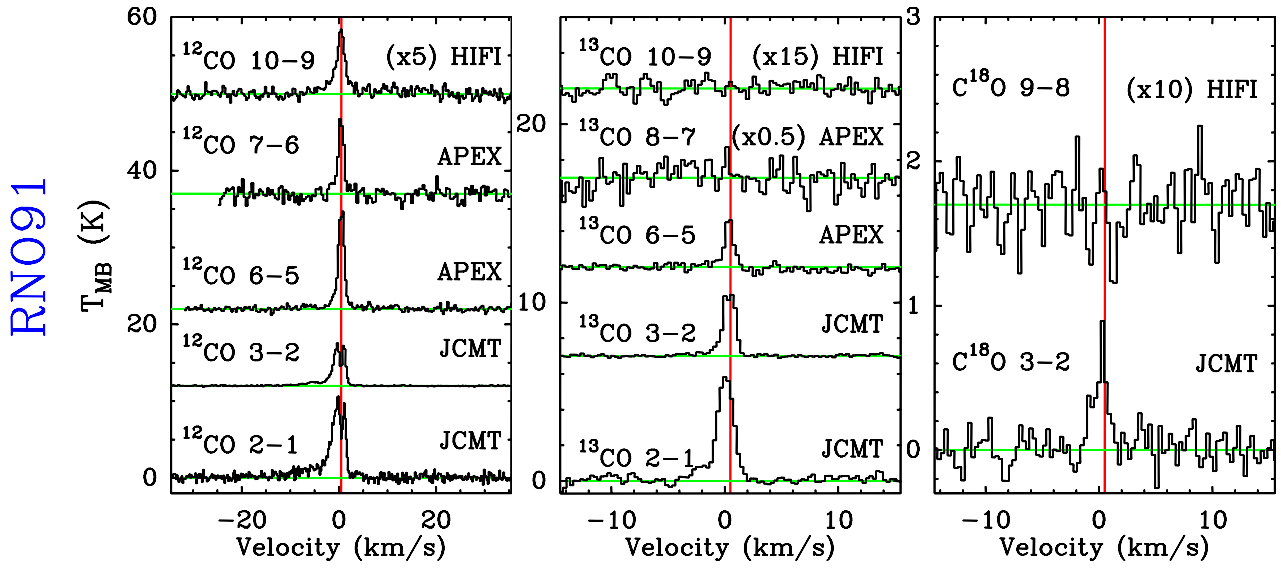
C.26. RNO91

Fig. C.26. Observed ^{12}CO, ^{13}CO, and C^{18}O transitions for RNO91.

Table C.26. Observed line intensities for RNO91 in all observed transitions.

Mol.	Transition	Telescope	Efficiency η	$\int T_{\mathrm{MB}} dV$ [K km s^{-1}]	T_{peak} [K]	rms [K]
CO	2–1	JCMT-RxA	0.69	40.47	10.64	0.42
	3–2	JCMT-HARPB	0.63	16.75	6.19	0.064
	6–5	APEX-CHAMP$^+$	0.48	25.96	13.45	0.33
	7–6	APEX-CHAMP$^+$	0.49	14.87	11.06	1.15
	10–9	*Herschel*-HIFI[a]	0.64	5.19	1.69	0.10
^{13}CO	2–1	JCMT-RxA	0.74	11.77	5.87	0.39
	3–2	JCMT-HARPB	0.63	5.38	3.92	0.08
	6–5	APEX-CHAMP$^+$	0.45	2.43	2.98	0.28
	8–7	APEX-CHAMP$^+$	0.49	1.55	4.58	1.77
	10–9	*Herschel*-HIFI[a]	0.74	<0.072	...	0.028
C^{18}O	3–2	JCMT-HARPB	0.63	1.13	1.06	0.14
	9–8	*Herschel*-HIFI[a]	0.74	<0.052	...	0.023

Notes. [a] H- and V-polarization observations averaged.

Appendix D: *Herschel*-HIFI observation IDs

Table D.1. *Herschel* obsids for related observations.

Source	^{12}CO 10–9	^{13}CO 10–9	^{13}CO 8–7	C^{18}O 5–4	C^{18}O 9–8	C^{18}O 10–9
L1448-MM	1342203253	1342201803	. . .	1342203186	1342203182	1342201802
IRAS 2A	1342191701	1342191657	1342225937	1342192206	1342191606	1342215968
IRAS 4A	1342191721	1342191656	1342225938	1342192207	1342191605	1342249014
IRAS 4B	1342191722	1342191655	1342225940	1342192208	1342191604	1342249851
L1527	1342203256	1342216335	. . .	1342203188	1342203156	. . .
Ced110IRS	1342201734	1342200765	. . .	. . .	1342201756	. . .
BHR71	1342201732	1342200764	. . .	1342200755	1342215915	. . .
IRAS 15398	1342214446	1342214414	. . .	1342266008	1342203165	. . .
L483	1342217730	1342207374	. . .	1342207582	1342218213	1342207375
Ser SMM1	1342207701	1342207379	1342229782	1342194463	1342194994	1342207378
Ser SMM4	1342207700	1342207380	1342229782	1342194464	1342194993	1342207381
Ser SMM3	1342207699	1342207377	. . .	1342207580	1342207658	1342207376
L723-MM	1342210152	1342210168	. . .	1342219172	1342210041	. . .
B335	1342230175	1342219248	. . .	1342219182	1342219217	. . .
L1157	1342198346	1342200763	. . .	1342199077	1342197970	. . .
L1489	1342203254	1342203938	. . .	. . .	1342203158	. . .
L1551-IRS5	1342203258	1342203940	. . .	. . .	1342203153	. . .
TMR1	1342225917	1342203937	. . .	. . .	1342203157	. . .
TMC1A	1342225916	1342215969	. . .	. . .	1342203154	. . .
TMC1	1342203255	1342216336	. . .	. . .	1342203155	. . .
HH46	1342222281	1342194785	. . .	. . .	1342195041	. . .
DKCha	1342201733	1342201590	. . .	. . .	1342201755	. . .
GSS30 IRS1	1342214442	1342214413	. . .	. . .	1342203163	1342250604
Elias29	1342214443	1342214408	. . .	1342266143	1342203162	1342249849
Oph IRS63	1342214441	1342214407	. . .	. . .	1342203164	. . .
RNO91	1342214440	1342214406	. . .	. . .	1342204512	. . .